

✓

**SUGAR CRYSTAL SIZE CHARACTERIZATION  
USING DIGITAL IMAGE PROCESSING**

by  
Getachew Abebe Argaw

submitted in fulfillment of the academic

requirements for the degree of

**Doctor of Philosophy**

School of Physics

University of KwaZulu-Natal

Durban, South Africa

December 2007

As the candidate's supervisors we have/have not approved this thesis for submission.

1. Name: \_\_\_\_\_ Signature: \_\_\_\_\_ Date: \_\_\_\_\_

2. Name: \_\_\_\_\_ Signature: \_\_\_\_\_ Date: \_\_\_\_\_


## Abstract

The measurement of the crystal size distribution is a key prerequisite in optimising the growth of sugar crystals in crystallisation pans or for quality control of the final product. Traditionally, crystal size measurements are carried out by inspection or using mechanical sieves. Apart from being time consuming, these techniques can only provide limited quantitative information. For this reason, a more quantitative automatic system is required. In our project, software routines for the automated measurement of crystal size using classical image analysis techniques were developed. A digital imaging technique involves automatically analyzing a captured image of a representative sample of  $\approx 100$  crystals for the automated measurement of crystal size has been developed. The main problem of crystals size measurements using image processing is the lack of an efficient algorithm to identify and separate overlapping and touching crystals which otherwise compromise the accuracy of size measurement. This problem of overlapping and touching crystals was addressed in two ways. First, 5 algorithms which identify and separate overlapping and touching crystals, using mathematical morphology as a tool, were evaluated. The accuracy of the algorithms depends on the technique used to mark every crystal in the image. Secondly, another algorithm which used convexity measures of the crystals based on area and perimeter, to identify and reject overlapping and touching crystals, have been developed. Finally, the two crystal sizing algorithms, the one applies ultimate erosion followed by a distance transformation and the second uses convexity measures to identify overlapping crystals, were compared with well established mechanical sieving technique. Using samples obtained from a sugar refinery, the parameters of interest, including mean aperture (MA) and coefficient of variance (CV), were calculated and compared with those obtained from the sieving method. The imaging technique is faster, more reliable than sieving and can be used to measure the full crystal size distributions of both massecuite and dry product.

## Declaration

This research work was conducted in two phases. During the first phase, a survey of all sugar industries in Ethiopia was undertaken. The survey helped to identify what technology was being used to control the quality of the exported sugar. The second phase of the work was carried out in the Applied Physics Group (APG) laboratory University of KwaZulu-Natal, Durban, South Africa, from February 2004 to December 2007, under the supervision of Professor M.J. Alport and Dr. S.B. Malinga.

The dissertation represents the original work by the author and have not otherwise been submitted in any form for any degree or diploma to any tertiary institution. Where use has been made of the work of others it is duly acknowledged in the text.

Signature:  Name: Getachew A. Argaw Date: 05/11/2008

## Acknowledgment

First of all I would like to extend my sincere appreciation and gratitude to my supervisor Prof. M.J. Alport who patiently and relentlessly guided me through all those years of my study. Had it not been for his help and guidance, this work could have not been successful. I am also indebted for the support that I got from Dr. S.B. Malinga.

Many thanks to Prof. J. Tapamo School of Geology and Computer Science, University of KwaZulu-Natal, for his valuable guidance. My appreciation and thanks to my best friends Dr. Mohamed Gar-elanabi and Dr. Justice Msomi. I would like to acknowledge the contributions of SMRI staffs particularly Dr. M.J. Kort, Mr. Greg Mitchell Hullet Refineries Durban for supplying sugar samples, Mr. Jonathan Lamb Alport and all in Applied Physics Group, University of KwaZulu-Natal South Africa.

The role my wife, W/r Azeb Alemayehu, played to ease painful moments due to academic rigorous was pivotal for successful completion of my study. In her absence, no word can tell how tough the situation was at the beginning of my study. We are now blessed by a baby girl Edda Getachew who already brought joy to the family. Many thanks Azu. My thank also goes to my family and friends.

## Dedication

This work is dedicated to my father Ato Abebe Argaw who was not lucky to see this day.

# Contents

Abstract	i
Declaration	ii
Acknowledgment	iii
Dedication	iv
Table of Contents	iv
List of Tables	viii
List of Figures	x
List of Abbreviations	xvii
<b>1 Introduction</b>	<b>1</b>
1.1 Justification . . . . .	2
1.2 Description of the Processes Involved in Sugar Production . . . . .	3
1.2.1 Sugar Cane Juice Extraction and Clarification . . . . .	4
1.2.2 Crystallization Process . . . . .	4
1.2.3 Fugal Stations . . . . .	5
1.3 Review of Crystal Size Measurement Techniques . . . . .	5
1.4 Overview . . . . .	7
<b>2 Literature Review</b>	<b>10</b>
2.1 Introduction . . . . .	10
2.2 Grain Size Analysis . . . . .	10
2.2.1 Powers Method . . . . .	10

2.2.2	Rens method . . . . .	11
2.2.3	The RRSB Method . . . . .	13
2.2.4	Butler Method . . . . .	14
2.2.5	Comparison of Grain Size Methods using Artificial Data . . . . .	14
2.3	Calculating MA and CV from Crystal Images . . . . .	16
2.3.1	Summary of Size Distribution . . . . .	17
2.4	Grain Size Analysis Using Sieve . . . . .	18
2.5	Alternative Crystal Size Control Techniques . . . . .	19
2.5.1	Image Based Techniques . . . . .	19
2.5.2	Non-Image Based Techniques . . . . .	21
2.6	MA and CV as Process Control . . . . .	25
<b>3</b>	<b>Mathematical Morphology</b>	<b>27</b>
3.1	Introduction . . . . .	27
3.2	Neighbouring Pixels . . . . .	28
3.2.1	Connectivity of Connected Components . . . . .	28
3.2.2	Structural Element (SE) . . . . .	29
3.3	Basic Morphological Operators . . . . .	30
3.3.1	Erosion . . . . .	30
3.3.2	Dilation . . . . .	30
3.3.3	Properties of Erosion and Dilation . . . . .	31
3.4	Morphological Opening and Closing . . . . .	32
3.4.1	Opening . . . . .	32
3.4.2	Morphological Closing . . . . .	32
3.4.3	Properties of Opening and Closing . . . . .	33
3.5	Recursive Erosion . . . . .	34
3.6	Ultimate Erosion . . . . .	35
3.7	Distance Transformation . . . . .	35
3.8	Watershed Segmentation . . . . .	36
3.9	Summary . . . . .	38
<b>4</b>	<b>Algorithms for Crystal Size Measurements</b>	<b>39</b>
4.1	Introduction . . . . .	39
4.2	Imaging Hardware and Acquisition . . . . .	40

4.3	Applying Watershed Segmentation . . . . .	40
4.4	Image Processing Algorithms . . . . .	41
4.4.1	Foreground and Background Marker . . . . .	43
4.4.2	Ultimate Erosion as a Marker . . . . .	43
4.4.3	Distance Transform as a Marker . . . . .	44
4.4.4	Combining Markers . . . . .	44
4.5	Manual Clicking . . . . .	47
4.6	Accuracy of the Segmentation Algorithm . . . . .	47
4.7	Discussion and Conclusion . . . . .	55
<b>5</b>	<b>Use of Convexity to Remove Overlapping Crystals</b>	<b>59</b>
5.1	Introduction . . . . .	59
5.2	Contour Tracing . . . . .	60
5.3	Convex Hull . . . . .	62
5.4	Convexity Measure . . . . .	63
5.5	Evaluation of the Two Class Classifiers Using the ROC Curve . . . . .	64
5.5.1	AUC as a Performance Measure . . . . .	64
5.6	Segmentation and Calculating Convexity . . . . .	66
5.6.1	Segmentation of Crystals . . . . .	66
5.6.2	Calculation of Convexity Measures . . . . .	68
5.6.3	Classification and Choice of Thresholds . . . . .	70
5.6.4	Classifier Accuracy using AUC . . . . .	73
5.6.5	Calculation of MA and CV . . . . .	74
5.7	Discussion and Conclusion . . . . .	76
<b>6</b>	<b>Application of ANNs and SVMs to Classify Crystals as Overlapping and Non-overlapping</b>	<b>78</b>
6.1	Introduction . . . . .	78
6.2	Artificial Neural Networks . . . . .	79
6.3	Multilayer Perceptrons (MLPs) . . . . .	79
6.4	Supervised Classification Results using Neural Network . . . . .	81
6.5	Support Vector Machine . . . . .	83
6.6	Supervised Classification Results using Support Vector Machines . . . . .	84
6.7	Conclusions . . . . .	85



<b>7</b>	<b>Comparison of Crystal Sizing Algorithms and Sieving Technique</b>	<b>86</b>
7.1	Introduction . . . . .	86
7.2	Crystal Size Distribution Analysis using Mechanical Sieve . . . . .	87
7.3	Using Digital Image Processing . . . . .	89
7.4	DIP and Mechanical Sieving Methods . . . . .	89
	7.4.1 Comparing with UE+DT Algorithm . . . . .	91
	7.4.2 Comparing with Convexity Based Algorithm . . . . .	95
7.5	Discussion . . . . .	98
7.6	Conclusions . . . . .	100
<b>8</b>	<b>Summary and Conclusions</b>	<b>101</b>
8.1	Summary . . . . .	101
8.2	Limitations and Recommendations . . . . .	103
8.3	Conclusions . . . . .	103
8.4	Future Work . . . . .	104

## List of Tables

2.1	Summary of MA and CV calculated using grain size analysis methods for normal artificial data. . . . .	16
2.2	Summary of MA and CV calculated using grain size analysis methods for skewed artificial data. . . . .	17
4.1	Average percentage error in mean aperture MA, calculated after applying the segmentation algorithms BF, UE and DT and the two combinations BF+UE and UE+DT. . . . .	48
5.1	Confusion Matrix . . . . .	64
5.2	Confusion matrix using convexity threshold values of $C_A = C_P = 0.85$ for all the 2175 crystals in the 25 images. . . . .	71
5.3	Summary of % errors and correlation coefficients for MA and CV after applying convexity based algorithm . . . . .	76
6.1	Confusion matrix calculated using ANN . . . . .	82
6.2	Confusion matrix calculated using SVM . . . . .	85
7.1	Summary of MA and CV and their % error calculated using sieving and UE+DT for two samples labeled $n = 1, 2$ . The % errors for MA and CV are calculated with respect to the values obtained by the direct clicking method. . . . .	93
7.2	Summary of MA and CV and their % error calculated using sieving and convexity method for two samples labeled $n = 1, 2$ . The % errors for MA and CV are calculated with respect to the values obtained by direct clicking method. . . . .	95

7.3 Summary of MA and CV calculated using sieving and automatic algorithms for two samples. A shifting factor  $S = 0.61$  was used for UE+DT while  $S = 0.55$  was used for convexity algorithm. . . . . 98

## List of Figures

1.1	Schematic of the various stages in processing sugar cane through to the production of the final product. . . . .	3
2.1	The frequency of occurrence for artificial data used to test methods of grain size analysis. It is a normal distribution with $\mu = 1000\mu\text{m}$ , $\sigma = 262\mu\text{m}$ and skewness = 0.10 . . . . .	15
2.2	The frequency distribution for artificial data used to test methods of grain size analysis. It is a non-normal distribution with $\mu = 1000\mu\text{m}$ , $\sigma = 262\mu\text{m}$ and skewness = 1.2 . . . . .	16
3.1	A pixel P in the square grid and its 4-neighborhood. . . . .	29
3.2	Typical examples of structural elements centered at 'c'. . . . .	30
3.3	Example of erosion transformation using $3 \times 3$ structural element center at 'c'. . . . .	31
3.4	Effect of dilation transformation using $3 \times 3$ structural element center at 'c'. . . . .	31
3.5	Example of opening transformation using $3 \times 3$ structural element center at 'c'. . . . .	33
3.6	Effect of closing transformation using $3 \times 3$ structural element center at 'c'. . . . .	33
3.7	Recursive erosion transformation . . . . .	34
3.8	Distance transformation using the three distance metrics . . . . .	36
3.9	Watershed transformation . . . . .	37

4.1	Flow diagram showing the steps used to segment the crystal images. The acquired image is binarized using Otsu's thresholding method and then marked using UE, DT, FB or a combination of those techniques. Finally watershed flooding is applied to determine the crest lines which separate the objects from each other and from the background. . . . .	42
4.2	Example of background segmented as a foreground. This is the result of mismarking background as a foreground. . . . .	44
4.3	Example of a crystal image marked by several markers and the resulting image when watershed segmentation was applied . . . . .	45
4.4	These are examples to illustrate how well the algorithms segment a sample crystal (a) from the background. The distance transform gives the best result when combined with ultimate erosion. The individual algorithms FB (b), UE(c) and DT (d) in addition (FB+UE) underestimates the area of the crystal. . . . .	46
4.5	The number of crystals segmented using UE+DT (dot) and manually (star)for each of the crystal images. In most images the number of crystals identified by the algorithm is less than the manual method since the algorithm rejected small fragmented crystals. . . . .	48
4.6	Percentage error in the number of crystals segmented using UE+DT and manually. In most images the number of crystals segmented by UE+DT is lower than manual. . . . .	49
4.7	Crystal contours overplotted on the original image (image #23) after segmented using UE+DT. Crystals touching the edge of the image and small sized crystals were rejected (shown by the arrows). . . . .	49
4.8	Scatter plot for the area of crystals analyzed in an image. The abscissa is area calculated manually and the ordinate represents the area calculated using UE+DT. The line is the least square fitted curve with the coefficient of 0.94 and -19. Generally the segmenting algorithm slightly underestimates the area of the crystals. Few outliers are circled.	50
4.9	Scatter plot of the percentage error in the area computed using UE+DT and manually for each of the crystals in in image # 23. For most crystals UE+DT underestimates their area with an average percentage of error approximately 10. . . . .	51

4.10	Frequency distribution for the crystals (in image #23) whose area calculated manually after excluding the crystals that were not segmented by UE+DT. . . . .	51
4.11	Frequency distribution for the crystals (in image #23) whose area calculated using UE+DT. . . . .	52
4.12	Scatter plot of the mean size defined as the mean of the square root of the area ( $\sqrt{A}$ ) of the crystals calculated for each of the 25 images. . . . .	52
4.13	Scatter plot for the mean area calculated for all the crystals in each of 25 images. On the vertical axis is the mean area predicted using UE+DT and on the horizontal axis is the mean area calculated manually by clicking the individual crystal in each image. . . . .	53
4.14	Scatter plot of MA for each of the 25 crystal images. The values on the vertical axis were calculated using UE+DT and the horizontal values were calculated by manually clicking the individual crystals. The best-fit straight line has coefficients of 0.92 and 61. . . . .	54
4.15	Scatter plot for CV. The vertical axis shows the predicted value and the horizontal axis is calculated manually from the crystal images. . . . .	54
4.16	Frequency of occurrence for crystal size, defined as $\sqrt{A}$ , distribution calculated manually. . . . .	55
4.17	Frequency of occurrence for crystal size, defined as $\sqrt{A}$ , distribution calculated using UE+DT. . . . .	56
4.18	Percentage error in CV calculated using UE+DT and manual. The average absolute error of 12 %. . . . .	56
5.1	Boundary tracing: (a) direction notation for 4-connectivity; (b) direction notation for 8-connectivity; (c) pixel neighborhood search sequence in 4-connectivity; (d),(e) search sequence in 8-connectivity; (f) boundary tracing in 8-connectivity (dashed lines show pixels tested during the border tracing) . . . . .	61

5.2	An example region (shaded grey) together with its convex hull (region bounded by dashed line) which is formed by a rubber band if it were to be placed around the region. Beginning at a point $P_1$ on the boundary, and moving in an anti-clockwise direction the next point on the convex hull, $P_q$ is found when the angle formed by the vector $\overline{P_1P_q}$ is a minimum. This process is then repeated. . . . .	62
5.3	Flow diagram showing the steps used to segment the crystal images using the convexity measures. The acquired image was binarized using Otsu's thresholding method and morphological operators and then the areas and perimeters of the connected component and convex hull were calculated. Finally the convexity measures, based on the areas and perimeters, were calculated and threshold values were applied to identify and reject overlapping crystals. . . . .	67
5.4	An example crystal image showing the individual crystals, together with their individual contours. This example also shows that some crystals could be ignored by the algorithm when they were joined by a few pixels. . . . .	68
5.5	Convex hull of a connected component in blue color over plotted segmented image and traced contour in red. . . . .	69
5.6	Examples of two independent neighboring connected components whose convex hulls overlapped. Red marks the boundaries and blue their convex hulls. . . . .	69
5.7	The graph shows the number of crystals classified as overlapping and non overlapping crystals. The convexity values ( $C_A$ and $C_P$ ) vary from 0.55 to 1 in steps of 0.025. An image contained 80 crystals with 15 overlapping and 65 non overlapping which was counted manually. . .	70
5.8	Scatter plot for convexity measures $C_A$ and $C_P$ . Overlapping crystals are marked as '+' and non overlapping crystals are marked 'o'. . . .	71
5.9	The above images show an example of the result of a classifier of applying a convexity threshold value of $C_A, C_P = 0.85$ to typical crystal image resulting in 15 overlapping crystals in (a) and 65 non overlapping crystals in (b). . . . .	72

5.10	The ROC curve for a classification of the crystals into overlapping and non overlapping classes using different threshold values of the convexity measures $C_A$ and $C_P$ according to their convexity measure. The dotted plot represents the values computed for each confusion matrix with a line joins the points. The solid straight line represents the line of 'uselessness' which would result for no separation into classes.	73
5.11	Scatter plot of mean size $\sqrt{A}$ calculated for the 25 images. On the vertical axis is the mean size predicted after using convexity measure to automatically exclude overlapping crystals and the horizontal axis shows the mean size calculated by manually clicking around the individual crystals.	74
5.12	Scatter plot of MA for the 25 crystal images. The values on the vertical axis were calculated after removing overlapping crystals based on the convexity threshold and the horizontal values were calculated by manually clicking the individual crystals. The best-fit straight line has coefficients of 0.92 and 141.	75
5.13	Scatter plot of CV for the 25 images. The values on the vertical axis were calculated after removing overlapping crystals based on the convexity threshold and the horizontal values were calculated by manually clicking the individual crystals.	75
6.1	Two layers perceptron	80
6.2	Propagation rule and activation function for the MLT network	81
7.1	Example of sieves used for crystal sizing. They are four sieves and a pan at the bottom.	87
7.2	Example of elongated crystal passing a square sieve whose size is smaller than the length of the crystal. In this case crystal size is the measure of the other sides of the crystals.	88
7.3	Example to show a crystal whose length is bigger than a sieve size can pass through the square sieve aperture.	89
7.4	One possible operational definition of the length and width of a crystal can be based on the dimensions of a bounding box.	90



7.5	cumulative percentage by mass curves for SMRI sieving results (black), UE+DT (blue) and clicking (red). . . . .	92
7.6	An example of graph for correlation coefficient between SMRI sieving and UE+DT cumulative curves, calculated by shifting a UE+DT curve, versus the shifting factor. . . . .	94
7.7	cumulative percentage by mass curves obtained by using UE+DT (before and after shifting using $S = 0.61$ ) and sieving. Good agreement between the sieving and shifted UE+DT is observed. . . . .	94
7.8	The graph of cumulative percentage by mass verses crystal size calculated using convexity measure, sieve analysis and manual clicking for two samples (a and b). The red star is for convexity method, blue for the clicking and black star for the sieve. Only few data points can be obtained for the sieving method, which is one of its limitations. . . . .	96
7.9	The graph of cumulative percentage by mass verses crystal size calculated using convexity measure, sieve analysis (a and b). The red star is for shifted convexity method, blue for the original convexity and black star for the sieve. . . . .	97

## List of Abbreviations

2D - 2 Dimensional  
ANN - Artificial Neural Network  
AUC - Area Under the Curve  
CCD - Charge Coupled Device  
CV - Coefficient of Variance  
DIP - Digital Image Processing  
DT - Distance Transformation  
FB - Forward and Backward  
FB+UE - Forward and Backward plus Ultimate Erosion  
FPR - False Positive Ratio  
ICUMSA - International Commission for Uniform Methods of Sugar Analysis  
IPP - Image Pro Plus  
LCD - Liquid Crystal Display  
LSVM - Lagrangian Support Vector Machines  
MA - Mean Aperture  
MATLAB - MATrix LABoratory  
MLP - Multi Layer Perceptron  
NMR - Nuclear Magnetic Resonance  
PC - Personal Computer  
RGB - Red, Green, Blue  
RMS - Root Mean Square  
ROC - Receiver Operating Characteristics  
RRSB - Rosin, Rammler, Sperling and Bennett  
SASTA - South African Sugar Technologist Association  
SE - Structural Element  
SEM - Scanned Electron Microscope

SMRI - Sugar Milling Research Institute  
SVM - Support Vector Machines  
TNR - True Negative Ratio  
TPR - True Positive Ratio  
UE - Ultimate Erosion  
UE+DT - Ultimate Erosion plus Distance Transform  
USA - United States of America

# Chapter 1

## Introduction

Improved industrial process control promotes the quality of the output from a factory, which in turn guarantees the production of a shipment that has the required specification. Process control can be used in a sugar factory to ensure the quality of the final sugar product that meets certain specifications.

Sugar production undergoes a series of steps beginning from the sugar cane that arrives at the factory to the centrifuge where the sugar crystals are separated from the molasses. As described in Section 1.2.2, the pan system is the most crucial part of the sugar milling process as this is where the crystallization takes place.

The crystallization process is usually monitored using varieties of indirect techniques such as conductivity of the massecuite, boiling point elevation, stirrer torque and radio frequency measurements in addition to visual inspection. The results from such indirect measurements are evaluated and the necessary decisions are then made by the operators, who then make adjustment to the pressure, temperature, pH etc. This optimization is often compromised by operator fatigue and error. An automated system would not be subjected to these problems and would also allow for online feedback control.

The control of the growth of the sugar crystals is one area where the automated optimization would be of benefit to the sugar industry. Due to the fact that the quality of the sugar and the crystal growth rate depends on the crystal size distribution, research is required to design and build a system that measures the crystal

parameters such as the mean aperture (MA), coefficient of variance (CV), mean length, width, and aspect ratio (length/width).

In this work a computerized approach for measuring these crystal size parameters was investigated. The study demonstrated the possibility of designing an imaging system that can automatically measure crystal size parameters quantitatively, objectively and repeatedly without operator intervention.

## 1.1 Justification

Agro-processing is vital in developing countries, like Ethiopia, whose economy is highly dependent on agriculture. Processing agricultural products at different levels generate more income than unprocessed ones. With the introduction of improved agro-processing, it is possible to reduce the cost of production, which in turn maximizes the returns. Research on agro-processing technology mainly involves control of the quality of the product and so improves the efficiency of the production process. In the sugar industry, the quality of the yield is highly dependent on the quality of the raw material supplied to the factory. It is also equally dependent on the production processes at the factory.

To enhance their competitiveness in the international market, sugar-exporting countries, including Ethiopia, adhere to a set of standards that ensures a high standard of the exported sugar product. In these countries sugar mill owners can only deliver their product to the corporation (or recognized export promotion agency of the country) if they abide by these standards. Customers worldwide depend on both a reliable quality and supply of raw sugar, which always meets specific requirements.

To maximize income from sugar export and maintain competitiveness in the world market on a sustainable basis it is, therefore, necessary to conduct milling technology research to control the quality and improve the efficiency of the raw sugar production process. One important aspect of sugar crystal production is the need to optimize and monitor the crystal growth rate in the crystallization pans. Monitoring the process at the seeding stage of crystallization is required to establish if there is an adequate

population of sugar grains at the beginning of the process. Secondly it is required to establish whether or not the size distribution is bimodal which indicates the presence of false seeding which will compromise the overall crystal growth rate. Once a problem is detected, the necessary process control conditions (eg. pressure, temperature, or water content etc.) need to be adjusted in order to guarantee the adequate quality of the final product fixed by commercial specifications (i.e. adequate size and homogeneous grains). This study demonstrated that the measurement of sugar crystal size measurement can be efficiently achieved using crystal image-processing techniques.

## 1.2 Description of the Processes Involved in Sugar Production

In order to better understand the processes undertaken in a sugar factory, in January 2005, 3 factories (including Metehara, Wonji and Fincha) were visited in Ethiopia. Figure 1.1 shows an overview of sugar production processes at the sugar industry.

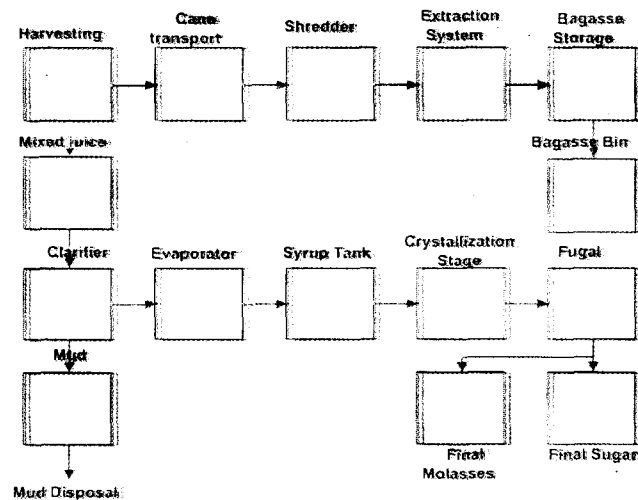


Figure 1.1. Schematic of the various stages in processing sugar cane through to the production of the final product.

### 1.2.1 Sugar Cane Juice Extraction and Clarification

After the sugar cane arrives at the factory, it is weighted at the weightbridge. The cane is then prepared by the shredder for the removal of juice by the extraction station. The extraction process done by series of mills which crash the cane to separate the juice (containing the sugar) from the fibrous part of the cane plant. The fibrous plant material left after the juice is removed is called bagasse. To help in the extraction of juice, water is applied to the bagasse between each crushing mill to wash out the extra sugar. The juice is then clarified. The clarification process removes dirt and other impurities from the juice by settling them in a clarifier. The impurities are then drawn off, washed and dried on a rotary vacuum filter to recover any sugar in the impurities. The clarified juice is then sent to the evaporation stage. Here most of the water is removed from the clear juice in a series of evaporators or effets. The syrup from the evaporator stage then goes to the pan stage.

### 1.2.2 Crystallization Process

The juice entering the evaporator stage has basically the same composition as the raw juice extracted from the sugar cane except for the mud removed by the clarifier. The evaporator (or effets) job is to evaporate most of the water present in the clarified juice and thus concentrate it. The material output of this is called syrup. In the crystallization pan stage, crystal sugar is produced from syrup.

The crystallization is carried out in large tanks or pans under a partial vacuum where the sugar crystals are grown from the syrup. This process involves first loading the pan with sub-saturated syrup, which is then heated under partial vacuum until conditions of oversaturation are reached. The sugar powder is then fed in as seed crystals, which grow during the boiling process. Monitoring the process at the seeding stage of crystallization is required to establish if there is an adequate population of sugar grains at the beginning of the process, secondly it is required to establish whether the size distribution is bimodal indicating presence of false seeding which will compromise the overall crystal growth rate. Once a problem is detected, the necessary process control conditions (e.g. pressure, temperature, or water content etc.) need to be adjusted. This task is needed in order to guarantee the adequate quality of the final product fixed by commercial specifications (i.e. adequate size and homogeneous grains).

### 1.2.3 Fugal Stations

The fugal stations or centrifuges are used to separate sugar crystals from the surrounding molasses by spinning. The massecuite is fed into a basket which is lined with a pierced metal screen backed by gauge. The holes on the screen contain the sugar but allow the molasses to pass through and escape. High grade fugals, grade A or B massecuite, separate shipment sugar from the A or B molasses which are subsequently returned to the appropriate tanks. Low grade fugals separate crystals and molasses in the low grade C massecuite in the crystallization pan.

## 1.3 Review of Crystal Size Measurement Techniques

As described in Chapter 2, in the literature, there are a number of reported direct and indirect techniques that have been used to monitor the growth of sugar crystals in the crystallization pan in addition to visual inspection. Some offline indirect techniques used the pH of the massecuite, conductivity of the liquor, boiling point elevation and etc. These indirect techniques were unable to quantify the size of the crystals in terms of their MA and CV instead they were used to determine solid content (sugar crystals in this case) in the massecuite.

Direct techniques on the other hand referred to those methods which could directly measure crystal size in terms of crystal size parameters (i.e. MA and CV). Direct crystal size measurement techniques include sieving of the dry sugar, laser diffractions of solid suspensions in the solution and crystal imaging methods.

Apart from being used to monitor crystal growth, indirect techniques had some disadvantages. Indirect techniques did not give quantitative information and the analysis was carried out in time intensive manner. Moreover they were subjective and thus prone to errors.

Among direct techniques, sieving method for dry sugar size measurement was well established. Due to the fact that only a few sieve mesh sizes were used sieving method could only provide limited information.



As also described in Chapter 2, previous workers have used a laser diffraction technique with a laser light source and typically 32 - semi-circular silicon detectors to measure the size of crystals. The silicon detectors collected the laser light diffracted by the solid suspensions in the solution. Because a relatively small number of semi-circular detectors were used, this limits the amount of detail information that could be extracted about the crystal size distribution. Moreover laser light sources are expensive.

To overcome some of these limitations, a computerized crystals image processing approach has been evaluated. This study demonstrates that, this method can give a quantitative, objective and reproducible size measurement. The study, furthermore, indicates the possibility of improved control of crystal growth during crystallization stages and online measurement for rapid analysis of samples.

The main problem in the crystal image processing is the lack of an efficient algorithm to separate overlapping and touching crystals which compromises the accuracy of size measurements. To address this problem, algorithms are developed to identify and either separate or reject overlapping and touching crystals. As described in Chapter 4, mathematical morphology has been used as a tool to mark and separate overlapping and touching crystals. However, this tool cannot 100% separate the touching and overlapping crystals, and moreover, it suffers from the problem of over segmentation. To alleviate this problem another algorithm is evaluated to identify and reject touching and overlapping crystals. The study shows that by classifying the crystals using their convexity measures (based on their perimeter and area) it is possible to reject overlapping and touching crystals with a high degree of accuracy.

The ultimate goal of this project is, therefore, to develop and test computerized sugar crystal imaging system that can measure the crystal size parameter MA and CV. The system is compared with the well established sieving method.

## Objectives

1. Implement algorithms to analyze images of dry sugar crystals and obtain parameters which describe their sizes such as MA and CV
2. To evaluate different algorithms developed to optimise the accuracy of the size measurements
3. To compare the algorithms with each other and with a manual method which involved clicking the border of the individual crystals using the computer mouse and with the well established sieving technique

## 1.4 Overview

The 25 sugar samples used in this study were supplied by the Hullet Sugar Refinery based in Durban, South Africa. The MA and CV of the samples were measured using sieving technique at the Hullet Refinery and Sugar Milling Research Institute (SMRI) also based in Durban, South Africa.

Images of the 25 sugar samples were captured using a high resolution CCD camera attached to a microscope. The crystals were deliberately spread on the microscope slide in such a way that they represented all the configurations (such as individual, touching and overlapping) that might be expected to be observed if the images were taken in the production environment. The images were then saved using bmp format and subsequent image analysis was carried out using a PC with a 1.5 GHz Intel Celeron Processor.

A detailed literature review, explaining different sugar crystal sizing techniques, is given in Chapter 2. As described in Chapter 2, these techniques were categorized as being either imaging or non-imaging and their respective advantages and disadvantages were also discussed. This chapter also contains results of the analysis, using artificially generated data, to compare the four (Powers, Rens, RRSB and Butler methods) ICUMSA<sup>1</sup> recommended crystal sizing models.

---

<sup>1</sup>International Commission for Uniform Methods of Sugar Analysis

Mathematical morphology (also called the mathematics of shapes) is defined in terms of non linear operators which characterize the shape of an object. In Chapter 3, definitions, implementations, and examples of morphological operations used in Chapter 4, are presented. Mathematical morphology is used as a tool in this study to mark individual crystals, to fill the curve, detect crystals edges, and to find watershed lines.

The main problem in crystal size measurement using crystals image processing is the lack of an efficient algorithm to separate touching and overlapping crystals. 5 algorithms, based on marker controlled watershed segmentation to identify and separate overlapping and touching crystals have been evaluated. Chapter 4 describes the results of these algorithms and the percentage error is calculated with respect to a manual measurement which involves clicking the border of the crystals using the computer mouse. The algorithm which combines ultimate erosion with distance transformation (UE+DT) as a marker was found to exhibit the lowest percentage error. This UE+DT algorithm was then used to calculate the crystal size parameters (MA and CV).

Marker controlled watershed segmentation was not 100% accurate. The accuracy of the algorithms depended on how well the crystals were marked. If the crystals were marked by multiples of markers, there was the problem of oversegmentation. To alleviate such problems another algorithm that identified and rejected overlapping and touching crystals were evaluated. This algorithm classifies the crystals using their convexity measures based on their area and perimeter. A detail description is presented in Chapter 5. A manual choice of the threshold values of convexity measures based on area and perimeter to classify crystals as overlapping and non-overlapping was used. Although this manual selection gave reasonably acceptable results, subsequent attempts were made to calculate the threshold values objectively.

In Chapter 6 two classification algorithms viz. Artificial Neural Network (ANN) and Support Vector Machines (SVM) were used to classify the crystals as overlapping and non-overlapping crystals.

Chapter 7 focuses on comparing the two image based algorithms which were developed in Chapters 4 and 5 with well established sieving technique. The crystal size parameters calculated using manual clicking borders of the crystals were also compared with mechanical sieving method. The results presented in Chapter 7 demonstrate that it is possible to develop computerized image based system to characterize crystal size parameters and which gives results comparable to the sieving technique.

Finally, a summary of the whole study including conclusions, recommendation and limitations, is given in Chapter 8.

# Chapter 2

## Literature Review

### 2.1 Introduction

The principal objective of sugar manufacturing operations is to ensure a consistent and acceptable product quality is achieved at the lowest cost. High sugar yields in conjunction with good mother liquor exhaustion during crystallization are important requirements to achieve this target. As a consequence, process control is of major importance. The critical components that need to be monitored during the crystallisation process are the supersaturation of mother liquors and the crystal content of the massecuite. The search to optimise production has led to numerous measurement methods to control crystals growth in the sugar industry. This chapter gives a detailed description about ICUMSA<sup>1</sup> recommended methods for grain size analysis and then presents sieving and different non-sieving methods that have been used to monitor sugar boiling.

### 2.2 Grain Size Analysis

#### 2.2.1 Powers Method

One of the first size characterisation methods to be used in the sugar industry was developed by Philip Lyle and first published by Powers (Powers, 1948). This method assumed particle size distribution to follow a normal probability distribution function which is fully represented by the mean of the distribution ( $\mu$ ) and its standard

---

<sup>1</sup>International Commission for Uniform Methods of Sugar Analysis

deviation ( $\sigma$ ). Due to the nature of the normal distribution function, the mean, median and mode of the distribution function all coincide. Furthermore, the standard deviation of a normal distribution may be calculated using the relationship:

$$\sigma = \frac{d_{84} - d_{16}}{2} \times 100\% \quad (2.1)$$

where  $d_{84}$  is the screen size through which 84.13% of the particles would pass ( $\mu + \sigma$ ) and  $d_{16}$  is the screen size through which 15.87% of the particle would pass ( $\mu - \sigma$ ). The Powers method exploits these characteristics for the analysis of grain sizes by characterising the particle size distribution using two parameters, namely the mean aperture (MA) and coefficient of variance (CV). MA is the median-size-by-mass of the distribution. This is the aperture size of a screen which would retain 50% by mass of the particles, while allowing 50% by mass of the particles to pass through. For the normal probability distribution, MA is also equivalent to the mean-size-by-mass of the particles. But this coincidental equivalence does not necessarily hold for non-normal distributions. The CV of the distribution is defined by the equation :

$$CV = \frac{d_{84} - d_{16}}{2MA} \times 100\% \quad (2.2)$$

which, for a normal distribution only, can be described as a standard deviation divided by the mean particle size by mass, expressed as a percentage. Practically, MA is defined as median-size-by-mass. In some article (Dalziel et al., 1999), however, MA is confused with mean-size-by-mass. This confusion arose when mean-size-by-mass was used for non-normal distribution whose mean and median were not the same.

The Powers method can be implemented by first plotting, on arithmetical probability paper, the cumulative mass retained on the probability axis against sieve aperture size on the linear axis and then by drawing the best fit straight line through the plotted points. MA and CV can be calculated by reading, from the graph, the apertures retaining 50% ( $d_{50}$ ), 15.87% ( $d_{16}$ ) and 84.13% ( $d_{84}$ ).

### 2.2.2 Rens method

The Rens method (Rens, 1978) and (ICUMSA, 1994) uses an empirical equation, to describe the crystal size distribution, and to convert the cumulative percentage

by mass retained by different aperture sizes to a linear relationship. For each sieve aperture size,  $d$ , the cumulative percentage by mass retained,  $y$ , is converted to a corresponding linear value,  $z$ , using the following empirical function:

$$z = \begin{cases} -34.5 \left[ 1.14 \sqrt{\ln \frac{50}{y}} - \exp^{-0.18y} \right] & \text{For } 10\% < y < 50\% \\ 0 & \text{For } y = 50\% \\ 34.5 \left[ 1.14 \sqrt{\ln \frac{50}{100-y}} - \exp^{-0.18(100-y)} \right] & \text{For } 50\% < y < 90\% \end{cases} \quad (2.3)$$

The formula is only applied to values of  $y$  greater than 10% and less than 90% and, over this range, there is approximately a linear relationship between  $z$  and  $y$ . The relation between  $d$  and the corresponding  $z$  values calculated is then determined by fitting a straight line which approximate the data points. The aperture size ( $d$ ) is then related to  $z$  as:

$$d = a + kz \quad (2.4)$$

where  $a$  and  $k$  are constants obtained from the regression analysis. The aperture retaining 50% of the sugar,  $d_{50}$ , is obtained when  $y = 50\%$  and therefore  $z = 0$ , i.e.

$$d_{50} = MA = a \quad (2.5)$$

If  $d_{16}$  is the aperture size that retains 16% of the sugar, then

$$d_{16} = MA + kz_{16} \quad (2.6)$$

Since  $d_{16}$  is the sieve size through which 16% of the particle would pass,  $d_{16}$  can then be given as:

$$d_{16} = MA - \sigma \quad (2.7)$$

Using Equation 2.6 and Equation 2.7 and remembering that  $CV = \frac{\sigma}{MA}$ , the following relationship can be achieved:

$$CV = \frac{kz_{16}}{MA} \quad (2.8)$$

### 2.2.3 The RRSB Method

This procedure is named after the authors (Rosin, Rammler, Sperling and Bennett) of a pioneering papers (Rosin et al., 1933) and (Bennet, 1936) and is based on an exponential function to describe the crystal size distribution. The equation for RRSB is based on exponential and is given by:

$$D(d) = 1 - R(d) = 1 - \exp \left[ - \left( \frac{d}{d'} \right)^n \right] \quad (2.9)$$

After taking the natural logarithm of equation 2.9 twice, the equation transforms to:

$$\begin{aligned} \ln \left( \ln \left( \frac{1}{1 - D(d)} \right) \right) &= n \ln(d) - n \ln(d') \\ &= n \ln(d) + C \end{aligned} \quad (2.10)$$

where  $D(d)$  is the cumulative mass fraction passed as function of crystal equivalent diameter in g/g,  $R(d)$  cumulative mass fraction retained as function of crystal equivalent diameter in g/g,  $d$  crystal equivalent diameter in mm,  $d'$  sieve aperture in mm corresponds to  $D = 0.632$ , and  $n$  slope of RRSB function. The RRSB graph is constructed by plotting  $\ln \left( \ln \left( \frac{1}{1 - D(d)} \right) \right)$  against  $n \ln(d)$ . Sugar with a grain size distribution that follows the RRSB function will be a straight line. The distribution is characterised by the gradient,  $n$ , of the line and the aperture  $d'$ . Where  $n$  is a measure of grain uniformity and  $d'$  is the sieve aperture that will pass 63.2% of the sample. In practice, first the cumulative mass fraction transmitted,  $D$ , is calculated for each sieve used in the crystal size analysis and then the values of  $D$  are plotted on the ordinate scale against sieve aperture,  $d$ , on the abscissa of the RRSB graph. The distribution function is then approximated by a straight line from which  $n$  and  $d'$  can be read. Pezzi and Maurandi (1993) established a mathematical relationships between Powers' (MA and CV) and RRSB's ( $d'$  and  $n$ ). MA is related to  $n$  and  $d'$  as:

$$MA = d' \times (\ln 2)^{\frac{1}{n}} \quad (2.11)$$



and the relationship between  $CV$  and  $n$  is given as:

$$CV = \frac{[\ln(100/15.87)]^{\frac{1}{n}} - [\ln(100/84.13)]^{\frac{1}{n}}}{2 \times (\ln 2)^{\frac{1}{n}}} \quad (2.12)$$

### 2.2.4 Butler Method

The Butler method (Butler, 1974) calculates the MA and CV directly from the percentage of fraction retained by each sieve used in the particle size analysis. The method assumes that the mean particle size of each percentage fraction is equal to the average of the sieve aperture retaining the fraction and the preceding aperture. In this way a size is attributed to each fraction and MA is calculated by taking the weighted mean of all fractions. CV is calculated by using the usual statistical relationship. MA and CV are then given by:

$$MA = \frac{\sum_i (R(d_i) \times d_i'')}{\sum_i (R(d_i))} \quad (2.13)$$

$$CV = \frac{SD \times 100}{MA} \quad (2.14)$$

where  $R(d_i)$  is the percentage retained,  $d_i''$  is the mean crystal size defined as the average of the sieve aperture of the retaining fraction and the aperture of the sieve immediately above and  $SD = \sqrt{\frac{\sum_i \{R(d_i) \times (MA - d_i'')^2\}}{\sum_i (R(d_i))}}$ . The value of  $d_i''$  for the uppermost sieve and the base is calculated using the next largest and smallest sieve in the series respectively.

### 2.2.5 Comparison of Grain Size Methods using Artificial Data

ICUMSA (ICUMSA, 1994) suggests that it is possible to calculate MA and CV using one of the following four techniques namely i) Powers ii) Rens iii) RRSB iv) Butler. According to ICUMSA the choice is left to the user. It is, however, a good idea to test the accuracy of crystal sizing methods using artificial data. The comparison was conducted using two artificially generated data sets, one of which had a normal

distribution with a skewness equal to 0.10 and the second one skewed to the right with 1.2 skewness value.

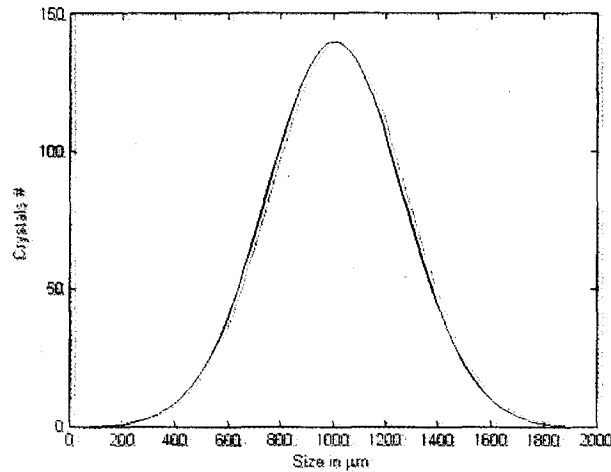


Figure 2.1. The frequency of occurrence for artificial data used to test methods of grain size analysis. It is a normal distribution with  $\mu = 1000\mu\text{m}$ ,  $\sigma = 262\mu\text{m}$  and skewness = 0.10

Figure 2.1 shows the frequency graph for normally distributed artificial data, with an arithmetic mean of  $\mu = 1000\mu\text{m}$  and  $\sigma = 262\mu\text{m}$ , used to evaluate grain size analysis methods. The cumulative percentage by mass for mass distribution (based on crystals volume) was computed assuming that the crystals were cubic in shape. This assumption might be acceptable if there was a need to investigate grain size analysis methods for an ideal situation like this. Parameters of interest including MA and CV were calculated. Table 2.1 shows MA and CV calculated using the grain size methods. MA was calculated within  $1184.7 \pm 2.9\mu\text{m}$  while CV was within  $20.5 \pm 0.3\%$ . The highest spread in CV resulted from powers method which gave the largest value in CV. To test the sensitivity of the grain size analysis methods, MA and CV were calculated for the skewed artificial data whose distribution graph shown in Figure 2.2.

Table 2.2 summarized the MA and CV calculated for the non-normal distribution. MA was estimated within  $1703.9 \pm 39.3\mu\text{m}$  which exhibited higher spread than normal distribution while CV was calculated to be  $32.6 \pm 1.0\%$  also shown higher standard deviation. In both distributions MA was more spread than CV. In general the standard deviation of both MA and CV increased when the distribution was non-normal. The next section focuses on how and why the Rens method can be used to calculate the crystal size parameters from crystals images.

Table 2.1. Summary of MA and CV calculated using grain size analysis methods for normal artificial data.

Methods	MA ( $\mu\text{m}$ )	CV (%)
Powers	1184.7	20.9
RRBS	1188.8	20.1
Rens	1182.3	20.6
Butlers	1182.9	20.4

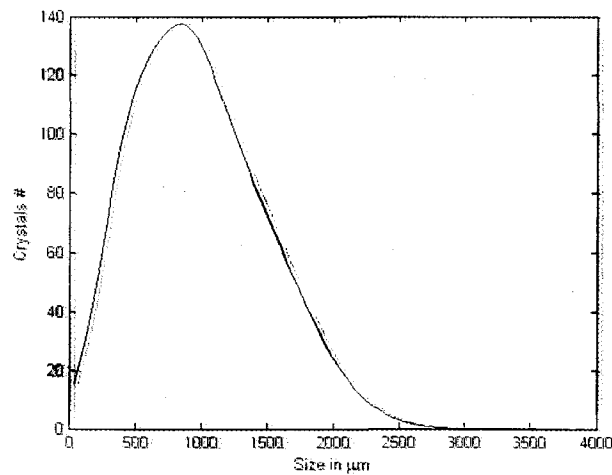


Figure 2.2. The frequency distribution for artificial data used to test methods of grain size analysis. It is a non-normal distribution with  $\mu = 1000\mu\text{m}$ ,  $\sigma = 262\mu\text{m}$  and skewness = 1.2

### 2.3 Calculating MA and CV from Crystal Images

The question is how is it possible to estimate MA and CV using classical image processing algorithms? The volume distribution is related to the projected area and the number of crystals i.e.  $V \propto NA^{3/2}$  (Dalziel et al., 1999). Using this relation one can estimate the cumulative percentage by mass retained in each bin. As pointed in Section 2.2.5, either of those four crystal sizing methods can be used to calculate MA and CV. As discussed in Section 2.2.1, the Powers method assumes that the distribution is normal. This assumption is not always true. RRSB and Rens methods were developed to suit both normal and non-normal distributions (ICUMSA, 1994). Comparative study in Section 2.2.5, using normal and non-normal artificial data, on crystal sizing methods indicated that MA and CV calculated by using Rens and RRSB agreed within the tolerance set by SMRI. After assessing the techniques currently used in South Africa, Peacock (2000) recommended RRSB as a standard.

Table 2.2. Summary of MA and CV calculated using grain size analysis methods for skewed artificial data.

Methods	MA ( $\mu\text{m}$ )	CV (%)
Powers	1686.9	33.1
RRBS	1691.0	31.7
Rens	1675.6	31.8
Butlers	1762.1	33.8

After a comparative study of the crystal size parameters estimated using Rens and RRBS methods, Schoonees (2002) confirmed that the average differences between the two calculations falls within the tolerance set by SMRI, which is  $\pm 0.03\text{mm}$  for MA and  $\pm 2\%$  for CV and recommended the use of the Ren's method. In this work, Rens method was employed for 2 reasons. The sieve analysis was done, at SMRI, using the Rens distribution and the same analysis could be followed to calculate crystal size parameters from crystal images. The second reason was that Rens and RRBS crystal sizing methods calculated MA and CV, for two artificial data, confirmed that their differences lie within tolerance set by SMRI.

### 2.3.1 Summary of Size Distribution

Powers (Powers, 1948) defined MA and CV as the median-size-by-mass and the corresponding standard deviation as the percentage of median-size-by-mass respectively. It was, however, pointed out by Peacock (2000) that there was confusion about the actual definition of MA and CV. This confusion arose when mean-size-by-mass was used for non-normal distributions whose mean and median were not the same. He, therefore, recommended that MA and CV should be calculated as mean-size-by-mass and its standard deviation as the percentage of mean-size-by-mass respectively. He further recommended that mean-size-by-number and its standard deviation as the percentage of mean-size-by-number should also be reported in addition to MA and CV. His recommendations are based on two major requirements of the sugar industry with regard to grain size analysis:

- The results of the analysis should be directly comparable with historical data, so that the previous knowledge gained by the industry is not lost.

- The result should be useful for further engineering calculation.

Peacock (2000) explained that historically, grain size analysis had been calculated using MA and CV, as originally defined by Powers (Powers, 1948). It is thus important that any future grain size analysis method should yield equivalent parameters. He further pointed out that MA and CV are not ideal for future engineering calculation as modeling of crystallization makes use of the mean-size-by-number and associated standard distribution to describe grain size distribution. Therefore he recommended that all four parameters (MA, CV, mean-size-by-number and standard deviation) should be reported for grain size distributions.

## 2.4 Grain Size Analysis Using Sieve

The sieve method for determining the size properties of raw and refined sugars is well established internationally for quality assessment (Miller and Beath, 2000). As described by a SASTA<sup>2</sup> document Anon (2005), the apparatus for the raw sugar sieving method comprises a sample divider or riffle, a top pan balance (which can measure mass with an accuracy of  $\pm 0.01$  g), woven wire cloth sieves (1700, 1180, 1000, 850, 600, 500, and 350  $\mu\text{m}$ ) and a mechanical shaker. The procedure involves sub-sampling until a sub-sample of about 100 g is obtained. The sieving procedure involves first weighting each sieve and the base pan and assembling the sieves in descending order of aperture size. The measured sub-sample is then transferred to the top sieve and shaken for 15 minutes. The values of the retained masses are converted to mean aperture (MA) and coefficient of variation (CV) using a calculation that assumes a model size distribution mentioned in Section 2.3. Significantly, although 7 sieve sizes are recommended in a SASTA document, in other production environments (e.g. in refineries) a smaller number of sieves (e.g. 3) are used. This can be acceptable, provided the size distribution has a consistent shape. This method has several advantages and disadvantages. It is a relatively straightforward technique that can be implemented in a production environment and requires only low technology equipment to give acceptable reproducibility and accuracy. It does, however, require a large sample and a relatively long preparation and measurement time. The major disadvantage of the sieving method is that the size distribution is

---

<sup>2</sup>South African Sugar Technologist Association

characterised by a relatively small number of parameters, since typically from 1 to 8 sieves are used. This prevents the detailed determination of the size distribution. It is, therefore, difficult to accurately characterise a crystal population, using a small number of sieves, if the sugar contains, for example, a large percentage of conglomerates or agglomerates, or has a high 'fines' component due to crystal breakage.

## 2.5 Alternative Crystal Size Control Techniques

Generally, non-sieving crystal sizing techniques can be categorised into two major categories, i.e. image and non-image based. Imaging refers to those techniques which involve acquiring and analysing images of the crystals.

### 2.5.1 Image Based Techniques

In South Africa, the idea of using an image based system for crystal sizing, dates back to early 1990's. Schumann and Thakur (1993) reported the possibility of using a video camera attached to a personal computer (PC) fitted with a frame grabber card in the sugar industry. The intention was primarily to replace expensive use of polaroid film to record sugar crystal images. The possibility of using imaging techniques to automate the measurements of size distribution was also mentioned. Their imaging system used a black and white CCD camera with an image size of 6.4mm  $\times$  4.8mm and a standard 25mm lens length whose magnification could be altered using an extension tube. Crystal images were analyzed using Image Pro Plus (IPP) package. Although it was not explained how, it was said that the IPP could be used to preprocess and threshold images and also to calculate area, perimeter and count the number of crystals in the image. One of the disadvantages in using the IPP software was that, it couldn't separate a touching and overlapping crystals. These touching and overlapping crystals were therefore treated as a single crystal without being separated. The paper proposed the use of feature such as roundness to identify and reject overlapping crystals. It also proposed a mechanical solution which involved dropping crystals in a sticky medium to separate crystals before imaging them. The results were not analysed in terms of MA and CV and size distributions were not given.

Palenzuela and Cruz (1996) have classified sugar crystal images based on spectral

analysis using neural networks. The spectral shape parameters (spectrum maximum, high energy bandwidth, total spectral energy) were used as inputs to a neural network to classify the images in terms of the crystal homogeneity, size distribution, etc. The results of the classification were purely qualitative, indicating the presence or absence of the above-mentioned situations. There was, thus, no numerical value given to quantify the size of the crystals in the image.

Dalziel et al. (1999) introduced a classical image analysis based system for crystal sizing. An image based algorithm first sorted the objects according to their grey scale values. Depending on their roundness, unwanted objects, including clusters of crystals, side-on crystals and bubbles were ignored. The problem of touching and overlapping crystals was addressed semi-automatically using a splitting function. However, not all overlapping and touching crystals could be separated using the same function and, in these cases, their boundaries were traced manually. Various properties of the region including area, perimeter, maximum linear dimension, aspect ratio, and roundness were estimated. Other parameters such as the volume equivalent size and projected area were calculated and used to compute the crystal size distribution. MA and CV were calculated using the imaging system and sieve technique for three dry sugar samples taken from sugar mills. There was, however, no ground truth to confirm the accuracy of those values. An interesting result shown in the paper was that the ratio of  $L$  (the diameter of a sphere that has the same volume as the crystal) to  $\sqrt{A}$  (square root of projected area) for Australian sugar was constant, i.e.  $\frac{L_v}{\sqrt{A}} = 0.97 \pm 0.01$ . This ratio was used to convert a two-dimensional projected area size into its three-dimensional volume equivalent size.

Crystal sizing, using masscuite image, at pan stage was reported by Ingram and Steindl (2001). It was the continuation of the work done by Dalziel et al. (1999). Their system comprised a digital camera, personal computer, an image processing software package (Image Pro Plus 4.1) and microscope slides. The crystal image was first converted into a grayscale image and this was followed by background subtraction to remove the effect of uneven lighting of the sample. Morphological opening was used to clean up specks and small protrusions on the crystal edges. After a series of pre processing operations, the image was thresholded to separate the foreground from the background. To split lightly touching crystals, 'limited watershed splitting' operation was applied. 'Limited watershed splitting' was described as a

specified number of morphological erosion operations to separate a touching crystals and the same number of dilation operations to enlarge the objects back to their original size but without allowing any of the objects that were split by erosion to be rejoined. Touching crystals and conglomerates were also identified and rejected using a criteria defined by  $\text{area}/(\text{length} \times \text{width}) < 0.7$ . The separated crystals were analyzed and their size, in terms of their volume equivalent ( $L_v$ ), projected area ( $A$ ) and their equivalent sieve size ( $L_s$ ) were calculated.  $L_v$  and  $L_s$  were calculated for each crystal from  $A^{\frac{1}{2}}$  using an empirical formula. Finally, mean size-by-number and mean size-by-mass, CV and density functions were calculated for both  $L_v$  and  $L_s$  size distributions. These calculated values were not compared to any standard methods to confirm their accuracy.

Peacock (1998) suggested the possible application of neural networks in the sugar industry for process control and subsequently, Mhlongo and Alport (2002) developed a crystal sizing technique using an artificial neural network after first performing a wavelet analysis of crystal images. The wavelet coefficients were used as inputs to a Multi-Layer Perceptron (MLP). An analysis of the percentage error in crystal size indicated that Daubechies wavelet coefficient performed better than the Haar, Symlet and Coiflet wavelets. Test results on 144 pan images showed a fairly good correlation between predicted mean size and actual mean size, with a mean percentage error of 9%. Predicted mean size and actual mean size for crystal images obtained from a laboratory crystaloscope immersed in a glycerin solution showed a mean percentage error of 12.9%.

## 2.5.2 Non-Image Based Techniques

There are a number of non-imaging methods for controlling crystal growth using laser diffraction, conductivity measure, viscosity measurement. The first control devices were based on boiling point elevation, refractometric index and conductivity (Theisen and Diringer, 2000). The conductivity method measured the concentration and the motion of the ions in the solution and therefore was greatly affected by changes in the purity and the temperature of the mother liquor during the crystallization. The boiling point elevation control methods on the other hand needed pressure to be constant in the pan. Small changes in pressure in the pan can affect the boiling point of the liquor. Furthermore boiling elevation cannot be used for the whole boil-



ing. Therefore, most sugar factories defined the end of the boiling indirectly by the current consumption of the stirrer. An increase in the viscosity of the massecuite is caused by high solid content of the boiling (sugar in this case) which in turn increased the power consumption of the stirrer. This increase in power consumption was used as an indicator to terminate the boiling process.

The refractometer was the only optical instrument which measured the concentration of the solution by the angle of refraction of the light. However, refractometers also have certain disadvantages. The concentration measurement only took place on the prism of the instrument which was extremely small compared with the volume of the pan. Therefore the refractometer measurement might not be representative of the total volume to be controlled (Theisen and Diringer, 2000).

A crystal growth monitoring system using laser diffraction was developed by Brown et al. (1991). The system used a laser source (1mW or 5mW He/Ne laser), Fourier transform lenses and a photo-sensitive detector. A parallel beam of Helium-Neon laser light was diffracted by crystals in the sample and then collected by a silicon detector. The detector was in the form of 32 semi-circular rings which were arranged at different distances from the center of the detector. The smallest crystals diffracted light the most and their light intensity and energy contribution was collected by the outer rings. The largest crystals contribute a diffracted light signal which was collected on the inner rings, near the center of the detector. A computer program used to calculate the mixture of particle sizes and concentrations which corresponds to the measured light intensities. The system calculated the crystal size distribution and the mean size. The system was not compared to any standard sugar size measuring method to confirm its accuracy. Furthermore the system had a limitation in terms of sample size which needed the volume of crystal suspension to be 1% of the total volume otherwise it obscured the laser light beam passing through the crystal suspension. The system was designed to calculate sugar crystal size assuming that the crystals were spherical. Due to the fact that the crystals can be any shape, this assumption for shape of crystals will introduce an error.

Theisen and Diringer (2000) reported a pan control system based on a microwave transmission measurement. The system operated by transmitting microwaves through

the media to be analyzed. The effective microwave field was generated in between the two transmitting and receiving antennas which were integrated with sensors. As a result of interactions, the microwaves were absorbed, reflected and scattered by the media to be measured. The overall absorption, reflection and scattering caused a reduction of the microwave energy and therefore an attenuation of the microwave field in between the sensors. Additionally, the phase velocity of the spreading microwave was changed according to the dielectric field which was built up by the media. The change in the wave phase velocity of microwaves was practically a shift of the phase of the wave. Both effects were based on the special dielectric properties of water. In the liquid phase, water has extremely high dipole strengths. During the transmission, these poles were polarized and set into vibration by the microwave field. The vibrations caused an intermolecular friction correlating with the energy reduction in the microwave field. Due to the fact that water has high dipole strength comparing with other solids in the solution, the energy reduction in the microwave correlated with the water content. This correlation was the basis for the indirect determination of dry substance content of the mixture of solids and water. This reduction in the field strength was described by the real and complex dielectric constant of the media. By determining values which were linked to the dielectric constant, the attenuation and phase shift were calculated. This in turn indicated the water content of the media. This system was used to measure the concentration of the massecuite that helped to determine the seeding point. However, it could not quantify the crystal sizes and was indirect measurement technique.

Miller and Beath (2000) presented a comparison of crystal sizes measured using laser diffraction and the traditional sieve technique. This measurement used crystals dispersed in a suitable suspending fluid such as methanol, or suspended in a parent growth solution and pumped through a flow cell from either a pilot scale apparatus or a factory pan. Sieves of sizes 420, 600, 850, 1000 and 1200  $\mu$ m were used. The results showed a linear relationship between MA using the sieving technique, and the volume median diameter (assuming that the crystals were spherical) using laser diffraction. Other crystals properties such as the specific surface area and surface area mean diameter were calculated for samples from four sugar mills and compared with the sieve technique. It was, however, observed that linear regression analysis for these parameters showed poor correlations and large standard errors.

Schultz and Edye (2000) introduced an online device for the measurement of crystal content of massecuite. The system was developed using low resolution nuclear magnetic resonance (NMR) instrumentation and was based on measuring the contribution of the solid and liquid parts of the massecuite to the decay of the NMR signal. It was designed to provide the time history of the crystal content in the pans. A knowledge of the crystal content for a given crystallisation pan helped the controller to take corrective action to optimise the pan capacity. The system, however, provided no direct measured value for the size of crystal, but only a graph of the percentage of crystal content as a function of time. Moreover, no comparison was made to verify the accuracy of the actual crystal content percentage.

Sugar crystallization process control over the whole range of boiling beginning from charging to end of the process, based on viscosity, was developed by Tzschatzsch et al. (2003). The system was an in-line torsional oscillating viscometer which used an oscillating sphere. The system used an oscillating sphere, magnetic coils, amplifier of variable gain, rectifier and an amplitude monitoring circuit. The sensing element was a stainless steel sphere immersed in the sample medium. Viscosity was determined by measuring the power required to maintain torsional vibrations of the sphere at constant amplitude. The functional dependence between the power required to maintain the oscillation of the sphere (sensor) at constant amplitude and dynamic viscoelastic was used to calculate viscosity of the boiling at different stages. The viscosity profile indicated the time history of the process from which the seeding point and the end of the process could be determined. The other important parameter in sugar process control is crystal content. Crystal content can be calculated indirectly from viscosity using an empirical formula and compared with the one calculated using radiometry and shown good correlation. It was recommended the combination of supersaturation (represented by viscosity) and dry solid content (represented as crystal content) could be a reliable tool to monitor the boiling in sugar industry. This system was, as far as the knowledge of the author concerned, the only one that could measure both supersaturation and crystal content. It, however, didn't calculate crystal size parameters. Moreover crystal content was calculated indirectly from supersaturation (viscosity) measurement.

An acoustic system for monitoring dry solid content (sucrose crystal) in cooling crystallization pans was developed by Bubnik et al. (2003). This ultrasonic measuring device could measure the concentration or the density of liquids as well as phase alteration or reactions. The system used the fact that the velocity of sound through a medium depends on the concentration and hence the density. The system comprised ultrasonic probes, the controller and LCD display and could indicate whether the boil (massecuite) reached the required brix (density) or not. The knowledge of concentration helped the controller to monitor the process and define the seeding and end points of the process. The system was not compared to either any standard system for accuracy or crystal size.

Other non imaging methods based on conductivity and fuzzy logic systems were used (Doss, 1983) and (Sharma et al., 2003) respectively. Conductivity of sugar, in the solid phase, as a measure of quality was presented by Prasad and Singh (1999). Due to the fact that the conductivity depends on the associated impurity contents of sugar, it was used to measure the quality of dry sugar. Seven sugar samples of different impurity level were used and their statistical T-test indicated that their corresponding conductivity measures were significantly different from each other. Each samples had a unique conductivity value that was used to measure the quality. This method could not provide information about the size of the sugar.

## 2.6 MA and CV as Process Control

In the sugar industry, a number of non-imaging process control techniques, based on boiling point elevation, conductivity, viscosity of the boil is use to optimise the crystallisation process. Crystal imaging and sieving technique can also be used to measure crystal size parameters. Most of the recent non-imaging pan monitoring techniques used supersaturation and crystal contents of the boil. Controlling the supersaturation of the mother liquor is crucial at the beginning of the boil to determine the seeding point. If the supersaturation of the boil is not monitored properly, then it is possible to get conglomeration and fine crystal formation which are undesirable. An uncontrolled rise in supersaturation of the massecuite toward the end of the product inhibits the circulation of crystals in the pan and hence leads to conglomeration.

So most of the methods on process control, in sugar industry, therefore, used supersaturation to monitor the pan. Merle (2004) recommended the combination of supersaturation and crystal content to optimize the whole process in sugar industry.

One question that may be asked where our work on process controls in terms of MA and CV can be used. Process control in terms of yields' MA and CV are not yet available (Merle, 2004) although researchers are still working on it (Ingram and Steindl, 2001) and (Dalziel et al., 1999). To the knowledge of the author no article has been encountered about process control using MA and CV. However, MA and CV have been used for dry sugar as a measure of quality. The answer to the question can be accurate measurement of crystal size parameters (MA and CV) using the cheapest and user friendly methods and combining this technique with the current indirect monitoring methods may provide more reliable control on the process. The use of digital imaging can therefore be taken as a low cost option for crystal size measurement. In the next Chapters (4 and 5), crystal sizing algorithms using crystal images are presented. In Chapter 3 the tools used to develop the algorithms are reviewed.

# Chapter 3

## Mathematical Morphology

### 3.1 Introduction

Mathematical morphology is a methodology for the quantitative analysis of special structures which was pioneered by G. Matheron and J. Serra at the Paris School of Mines, France, in 1960s (Serra, 1982). Its mathematical origin stems from set theory, topology, lattice algebra, random functions, and stochastic geometry. It is based on the algebra of non-linear operators operating on object shape. In many ways the method of processing resembles the linear algebraic system of convolution.

Mathematical morphology has variety of applications including image enhancement, image restoration, image segmentation, edge detection, curve filling, skeletonization and shape analysis. It can also be applied to texture analysis, feature detection, image compression, noise reduction, etc. Many problems in the fields of geosciences, material sciences, biomedical imaging, industrial applications, identification and security control and document processing have been tackled using mathematical morphology. In geosciences, it was used for the extraction of linear structures in satellite images of the earth surfaces (Destival, 1986), length and diameter estimation of man-made mineral fibers have been studied in the field of material sciences (Talbot, 1996) and (Talbot et al., 1996). Size measurements, in material sciences, required the development of an efficient methodology for separating connected fibers or crossing fibers in scanned electron microscope images (SEM). One of its applications in the field of biomedical imaging is the automatic recognition of cancerous cells using morphological openings by reconstruction and ultimate eroded sets (Thiran and Macq, 1996).

The processing of 2D electrophoresis gels using top-hat operation for normalizing the background and the union openings for removing the vertical and horizontal streaks is described in (Skolnick, 1986). Morphology operations have also been used to suppress uneven background illumination and detect defects such as spills, scratches, and cracks to inspect metal strip in industrial applications (Laitinen et al., 1990). Its application has been used in document processing to extract morphological features of print characters (Liang et al., 1994) and to extract morphological features for face recognition (Gordon and Vincent, 1992).

Due to the fact that mathematical morphology has also been applied in this work to characterize sugar crystal size distribution and to automatically measure MA and CV, it is necessary to discuss some of morphological operations. This chapter introduces definitions, implementations and examples of morphological operations. Although all definitions of mathematical morphology are applicable to gray level images, the focus of this chapter is on binary morphological operators as they are preferentially used in this work.

## 3.2 Neighbouring Pixels

An image can be considered to consist of a 2-dimensional array of square pixels arranged in a square grid. Figure 3.1 shows a black pixel, P, surrounded by a number of neighborhood pixels. P has 8 neighbors which can be classified into two groups i.e. those that have an edge in common with P and those that only have a point in common. The former group which are shaded grey in Figure 3.1 are called the 4-neighbors of P whereas the totality of neighbors is called the 8-neighborhood of P. Thus, all 4-neighbor pixels are also 8-neighbor pixels but some 8-neighbor pixels are not 4-neighbor.

### 3.2.1 Connectivity of Connected Components

One of the most important concepts in image processing is the notion of connectivity. For a square grid, let Q be a set of pixels (connected component). Q is called 4-connected (or a 4-connected component) if for every pair of pixels  $p_i, p_j$  in Q, there exists a sequence of pixels  $p_i, \dots, p_j$  such that 1) the sequence of pixels is contained

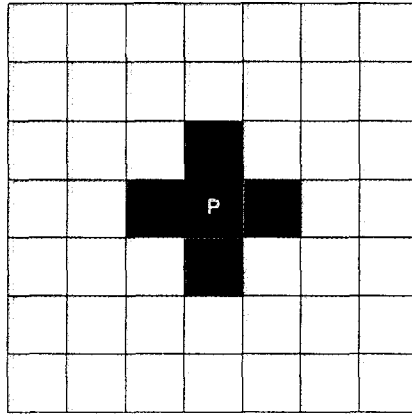


Figure 3.1. A pixel P in the square grid and its 4-neighborhood.

in Q and 2) every pair of pixels adjacent in the sequence are 4-neighbors of each other. Similarly, Q is 8-connected (or an 8-connected component) if for every pair of pixels  $p_i, p_j$  in Q there exists a sequence of pixels  $p_i, \dots, p_j$  such that 1) the sequence of pixels is contained in Q and 2) every pair of pixels adjacent in the sequence are 8-neighbors of each other.

### 3.2.2 Structural Element (SE)

A structural element (also called kernel) is a small set of pixels used to probe the image under study. It is typically translated to each pixel position in the image based on the origin. An origin must be defined for each SE so as to allow its positioning at a given pixel. The center pixel of the structuring element identifies the pixel of interest or the pixel being processed. In practice, the sizes and shapes of SE's are adopted to the image patterns being processed. There are varieties of SE's that differ in terms of their shape and size. In this work due to the fact that the 2D image of well formed crystals look rectangular in shape, a rectangular shaped structural element was used for the development of the crystal sizing algorithms. Typical examples of structuring elements are shown in the Figure 3.2.



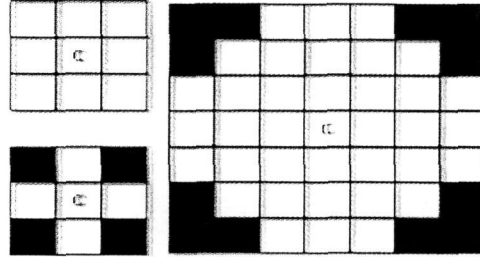


Figure 3.2. Typical examples of structural elements centered at 'c'.

### 3.3 Basic Morphological Operators

#### 3.3.1 Erosion

Erosion and dilation are the two fundamental morphological operators because all other operators are based on the combinations of these two processes. Although the notion is the same, different literature defines these operators differently. According to (Serra, 1982), who is one of the pioneers in the field, the eroded set of  $F$  is defined as the locus of centers of  $SE(K)$  included in the set  $F$ . This transformation looks like Minkowski subtraction. An image  $F$  eroded by a SE  $K$  is defined as:

$$E(F, K) = F \ominus K = \bigcup_{b \in K} (\{a - b \mid a \in F\}) \quad (3.1)$$

Erosion transformation can be regarded as shrinking operation. A typical example of the erosion operation for a binary image is illustrated in Figure 3.3. As the result of this transformation some pixels of the foreground in the original image become the part of the background. Only the set foreground pixels, that fit the center of the structural element and all other pixels of structural element contained in the foreground remain i.e. not eroded. As shown in the example when the size of structural element and the foreground in the original image are equal, only center of the foreground pixels remain (not eroded).

#### 3.3.2 Dilation

Dilation is the dual operator of erosion. The dilation of a set  $F$ , by a structuring element  $K$ , is defined as the locus of points  $x$  such that  $K$  hits  $F$  when its origin coincides with  $x$ . It is also called Minkowski addition. An image  $F$  dilated by a SE

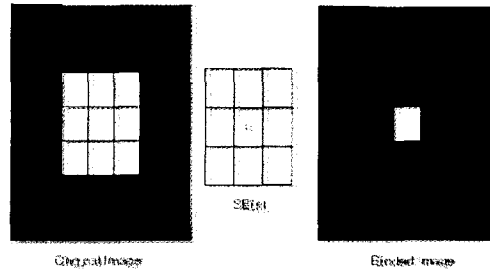


Figure 3.3. Example of erosion transformation using  $3 \times 3$  structural element center at 'c'.

$K$  is given as:

$$D(F, K) = F \oplus K = \bigcup_{b \in K} (\{a + b \mid a \in F\}) \quad (3.2)$$

The dilation operation can be regarded as an expansion operation. It is the reverse transformation to erosion operation. In the Figure 3.4, as result of this operation, some background pixels are transformed to foreground pixels. During transformation if one of the SE hits the foreground pixels, the pixel that coincide with the the center of SE will be counted as the foreground pixel. In this manner, depending on the size and the shape of the SE, the background pixels that surround the foreground can be transformed to the foreground pixels.

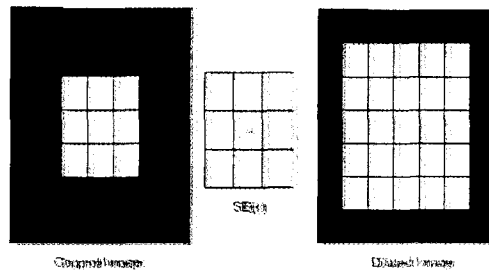


Figure 3.4. Effect of dilation transformation using  $3 \times 3$  structural element center at 'c'.

### 3.3.3 Properties of Erosion and Dilation

Erosion and dilation are complementary transformations. This means that after the erosion of an image, the original image can be recovered by applying dilation with the same structuring element. For an image  $F$  and structural element  $K$  defined in universal set  $U$  with  $F \subseteq U$  and  $K \subseteq U$ ,  $F \oplus K = (F^c \ominus K)^c$  where  $F^c = U \setminus F$ . Erosions and dilations are invariant to translations i.e.  $((F_x \oplus K) = (F \oplus K)_x$  or

$(F_x \ominus K) = (F \ominus K)_x$ . They also preserve the order relationships between images, that is, they are increasing transformations (i.e. if  $A \subseteq B$ , then  $(A \ominus K) \subseteq (B \ominus K)$  or  $(A \oplus K) \subseteq (B \oplus K)$ ).

## 3.4 Morphological Opening and Closing

### 3.4.1 Opening

The erosion of an image removes all structures that cannot contain the SE and also shrinks all the other ones. The search for an operator recovering most structures lost by the erosion leads to the definition of morphological opening operator. The principle is based on dilating the image previously eroded using the same structuring element. In general not all structures are recovered. For example, objects completely destroyed by the erosion are not recovered at all. Once an image has been eroded, there exists in general no inverse transformation to get the original back. The idea behind the morphological opening is to dilate the eroded image to recover as much of the original image as possible. An image  $F$ , opened by an SE  $K$ , is defined as the erosion by SE followed by the dilation with the transpose SE  $\hat{K}$  i.e.

$$O(F, K) = F \circ K = ((F \ominus K) \oplus \hat{K}) \quad (3.3)$$

Morphological opening removes all connected components whose sizes are smaller than the size of the structural element. In the Figure 3.5 there are two connected components whose sizes are smaller than the size of SE. The operation of morphological opening removes those two connected components. The central  $3 \times 3$  pixel connected component which has a size equal or bigger than the SE remains unchanged.

### 3.4.2 Morphological Closing

The idea behind the morphological closing is to build an operator tending to recover the initial shape of the image structures that have been dilated. This is achieved by eroding the dilated image. An image  $F$  closed by an SE  $K$  is defined as the dilation with a SE  $K$  followed by the erosion with the transposed structuring element  $\hat{K}$  i.e.

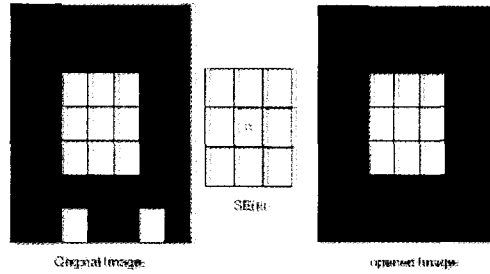


Figure 3.5. Example of opening transformation using  $3 \times 3$  structural element center at 'c'.

$$C(F, K) = F \bullet K = ((F \oplus K) \ominus \hat{K}) \quad (3.4)$$

The effect of closing operation fills the small holes which are smaller than the structuring element. The background pixels that cannot be covered by SE transformed to the object pixels as shown in the Figure 3.6.

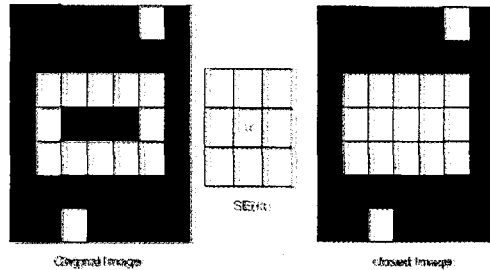


Figure 3.6. Effect of closing transformation using  $3 \times 3$  structural element center at 'c'.

### 3.4.3 Properties of Opening and Closing

An opening operation removes the object pixels that cannot be covered by the SE translations that fit the image objects. The closing has the opposite behavior because it adds the background pixels to foreground that cannot be covered by the SE translations that fit the background of the image. In other words, opening and closing are dual transformations i.e.  $((F \bullet K) = (F^c \circ K)^c)$ . The second property is that opening is anti extensive transformation as some of the pixels are removed and closing is extensive transformation (some pixels are added to foreground). Both opening and closing are increasing transformations. This means they preserve order relationships between images i.e. if  $A \subseteq B$ , then  $(A \bullet K) \subseteq (B \bullet K)$ . Moreover,

successive applications of openings and closings do not further modify the image i.e  $((F \bullet K) = (F \bullet K) \bullet K)$ . This property referred as the idempotent transformation. The idempotence property is often regarded as an important property for a filter because it ensures that the image will not be further modified by iterating the transformation.

### 3.5 Recursive Erosion

The recursive erosion transformation of a binary image is based on the successive morphological erosion of the image. In some literature it is also called the generalized distance transform (Chen and Haralick, 1996). Given a binary image  $F$ , the erosion transform of  $F$  with respect to a structuring element  $K$  produces a gray scale image where the gray level of each pixel  $x \in F$  is the generalized distance of  $x$  to the image background, i.e. the largest positive integer  $i$  such that  $x \in F \ominus^i K$ . The generalized distance at a pixel  $x$  indicates the maximum number of consecutive erosions of  $F$  by  $K$  such that  $x$  is still contained in the eroded image foreground. Mathematically it is represented as:

$$F \ominus^i K = \begin{cases} F & \text{if } i = 0 \\ (F \ominus^{i-1} K) \ominus K & \text{if } i \geq 1 \end{cases} \quad (3.5)$$

When performing recursive erosions of an object, components are progressively shrunk until they completely disappear. Figure 3.7 shows an example of successive erosion. With transformation, the object pixels were eroded until all the connected components have disappeared. It is useful for distance transform and segmentation.

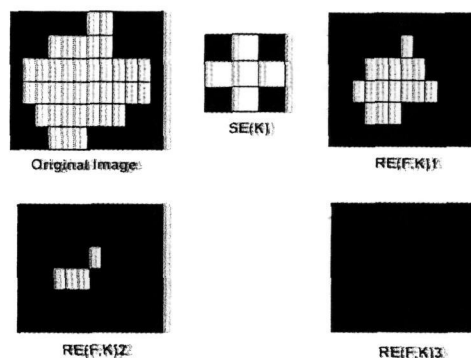


Figure 3.7. Recursive erosion transformation

## 3.6 Ultimate Erosion

The ultimate erosion of a binary image is defined as a set of connected components corresponds to the union of the regional maxima of the transformed image using recursive erosion. The regional maxima of the transformed binary image (which is gray scale image) is a connected set of pixels with an associated value of distance from the background pixel such that every neighboring pixel has a smaller greyscale value. In short the ultimate erosion of the object results in a region having an innermost connected components.

## 3.7 Distance Transformation

The distance transformation (DT) is used to convert a digital binary image that consists of an object (foreground) and non-object (background) pixel into another image in which each object pixel has a value corresponding to the minimum distance from the background (Frank and Yi-Ta, 2004). Three distance function metrics are often used in digital image processing. If there exist two points  $p = (x, y)$  and  $q = (u, v)$  in digital image, the distance function is defined as follows:

- City-block distance:  $d(p, q) = |x - u| + |y - v|$
- Chessboard distance:  $d(p, q) = \max(|x - u|, |y - v|)$
- Euclidean distance:  $d(p, q) = \sqrt{(x - u)^2 + (y - v)^2}$

The distance transformation is only applied to binary images. The result of the transform is a gray level image showing the distance to the closest boundary from each point. It is achieved using recursive erosions with a suitable SE until all foreground regions of the image have been eroded away. Each object pixel is labeled with the number of erosions that had been performed before it disappeared which indicates its distance from the background. Figure 3.8 shows a simple image and its distance transform using different distance metrics.

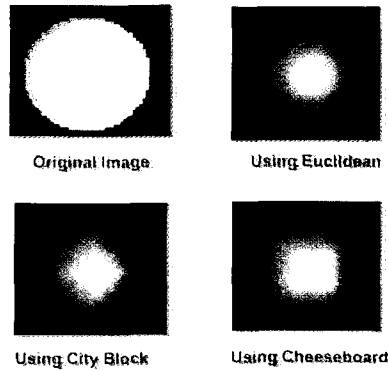


Figure 3.8. Distance transformation using the three distance metrics

### 3.8 Watershed Segmentation

The concept of a ‘watershed line’ was best explained by Vincent and Soille (1991) by referencing the ‘great divide’ in the USA which separates the catchment basins of Atlantic and Pacific oceans. Because of the divide, a drop of water falling one side of this line flows down until it reaches the Atlantic ocean, whereas a drop falling on the other side flows down to the Pacific ocean. The dividing line is called the watershed line. The two regions it separates are known as the catchment basins while the two oceans are the minima.

In the field of image processing, assuming that grey tone image as a topographic relief, the intensity of the pixel corresponds to the elevation at that point. This analogy helps to represent grey scale image with its minima, catchment basins and watershed lined. Several algorithms have been proposed to extract the watershed line that separates two or more minima. Details of their descriptions can be found in (Vincent and Soille, 1991). Comparative study of these algorithms indicates that the one based on immersion is accurate, fast and needs relatively low memory size. Since this immersion model will be used to segment the sugar crystals in the images, its algorithmic definition, adopted from (Vincent and Soille, 1991), is presented below.

Let  $F$  be a grey value image with  $F(p)$  represents pixel value at  $p$  and  $h_{min}$  and  $h_{max}$  being the minimum and maximum greyscale value of  $F$ . Define a recursion with a grey level  $h$  increasing from  $h_{min}$  to  $h_{max}$ , in which the basins associated with the minima of  $F$  are successively expanded. Let  $X_h$  denote the union of the set of

basins computed at level  $h$ . A connected component of the threshold set  $T_{h+1}$  at level  $h + 1$  can be either a new minimum, or an extension of a basin in  $X_h$ . If it is the extension of basins in  $X_h$ , the influence zone for each basin is calculated. The influence zone is called a catchment of basin and is defined as the set of pixels, at level  $h + 1$ , closer to one of the minima than to any other at the same level, with in the set  $X_{h+1}$ . The result gives  $X_{h+1}$ . Mathematically:

$$\begin{aligned} X_{h_{min}} &= p \mid F(p) = h_{min} = T_{h_{min}} \\ X_{h+1} &= Min_{h+1} \cup IZ_{T_{(h+1)}}(X_h), \quad h \in [h_{min}, h_{max}] \end{aligned} \quad (3.6)$$

where  $Min_{h+1}$  is a minimum at level  $h + 1$  and  $IZ_{T_{(h+1)}}$  is the influence zone of  $X_h$  at level  $h + 1$ . The watershed  $W(F)$  of  $F$  is the complement of  $X_{h_{max}}$  :

$$W(F) = F \setminus X_{h_{max}} \quad (3.7)$$

An example of watershed transformation with immersion using a simple  $3 \times 3$  image is shown in Figure 3.9. The letters A and B represent the minima and W is used to denote the watershed pixels.

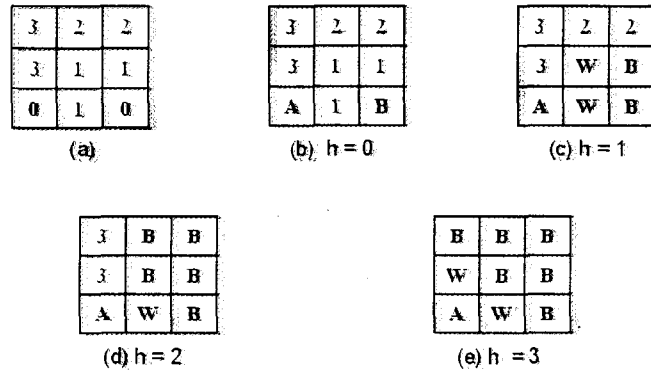


Figure 3.9. Watershed transformation

According to the immersion algorithm, it is the case that at level  $h + 1$  all non-basin pixels (i.e. all pixels in  $T_{h+1}$  except those in  $X_h$ ) are potential candidates to get assigned to a catchment basin in step  $h + 1$ . Therefore, pixels with a grey value less than or equal to  $h$  which are not yet part of a basin after processing level  $h$ , are merged with some basin at the higher level  $h + 1$ . Pixels, which in a given iteration



are equidistant with at least two nearest basins, may be provisionally labeled as 'watershed pixels' by assigning them the label  $W$ . However, in the next iteration this label may change again. A definitive labeling as a watershed pixel can only happen after all levels have been processed. In the figure there are two minima (zeros), so there will be two basins whose pixels are labeled A and B in Figure 3.9 (b - e). This shows what will happen as the immersion algorithm is applied to the grey scale image to extract the watershed lines.

### **3.9 Summary**

Crystal size measurements require an accurate segmentation of the border of the crystals. Marker controlled watershed segmentation are used to trace the boundaries. As it will be described in Chapter 4, distance transforms, ultimate erosion, local maxima, and their combination are used to mark crystals before the application of the watershed segmentation.

# Chapter 4

## Algorithms for Crystal Size Measurements

### 4.1 Introduction

In sugar production the optimal control of sugar crystal growth during the crystallisation stages is essential for producing sugar crystals having the required size specification. As discussed in Chapter 2, the process is usually monitored using a variety of indirect measurement techniques such as conductivity, boiling point elevation, stirrer torque and radio frequency measurements in addition to visual inspection. The results from such indirect measurements are judged and the necessary decisions are made by the operators, who then make adjustment to the pressure, temperature, pH etc. This optimisation is often compromised by operator fatigue and error. An automated system would not be subjected to these problems and would also allow for on-line feedback control. This might be achieved by developing software routines for the automated measurement of crystal size using classical image analysis techniques. In this Chapter, 5 algorithms have been evaluated to automatically determine the size distribution from images of crystal samples captured by a digital camera attached to a microscope. The algorithms measure crystal size parameters (MA and CV) in addition to the size distributions. The accuracy mainly depends on how well the crystals are segmented from the background in the crystal images. All 5 algorithms required watershed segmentation which was used to segment individual crystals, touching and overlapping crystals. The segmentation accuracy of the algorithm was found to depend on the pre watershed transformation operations used to

mark the crystals. The algorithms are compared with each other and with manual clicking techniques which is used as a ground truth.

The chapter is organized as follows. First all algorithms will be described and compared with the clicking method to evaluate their accuracy. The algorithm which combines ultimate erosion with distance transform (UE+DT) has shown better accuracy and is further discussed and evaluated. The chapter ends with a discussion and a conclusion.

## 4.2 Imaging Hardware and Acquisition

The imaging system comprises a high resolution CCD camera attached to microscope. The  $8\times$  magnified microscope images were captured and digitized to give a  $576 \times 768$  pixel color image at a resolution of 24 bits. The pixel separation, for 8 magnification, corresponded to  $8.85\mu\text{m}$  in the horizontal and  $16.49\mu\text{m}$  in the vertical directions. For the purpose of this work, 25 dry sugar samples obtained from the Hulleys refinery, in Durban South Africa, were used. Crystals were randomly spread on a microscope slide and images (each containing about 100 crystals) were captured. These images contained crystals having a variety of spatial configurations such as clustering, overlapping or just touching. The crystals were purposely not separated to ensure that the images represented typical configurations that could be encountered if the images were taken from the crystallization pan in a production environment. The analysis was performed using MATLAB which is a high-level technical computing language and uses interactive environment for algorithm development, data visualization, data analysis, and numeric computation (MATLAB, 6.5). It can be used in a wide range of applications, including signal and image processing, communications, control design, test and measurement, financial modeling and analysis, and computational biology. It can also be integrated with other languages and applications.

## 4.3 Applying Watershed Segmentation

As described in Chapter 3, watershed segmentation is a morphological algorithm which permits the detection of crest lines in images (Beucher, 1992). Considering the grey-tone image as a topographic surface, with greyscale of each pixel being

associated with the height, water falling on it will flow down the walls of the catchments basin corresponding to each minimum value of the greyscale. The points where the water can flow down either one of the two sides form the crest lines which are to be detected. An efficient implementation based on immersion simulation has been presented by Vincent and Soille (1991). This approach may be described as follows. If a hole is drilled in each minimum and filled, progressively with water, the watersheds would correspond to the line of the points where water coming from two different basins would meet. The concept of immersion can be implemented by making use of a hierarchical queue, with priorities defined by the grey level of image points. Points are recursively inserted and extracted from the queue, in an order defined by their grey levels. In this way, the lowest grey levels are processed before the highest ones. Watershed transformation was efficiently applied to segment electrophoresis gel (Beucher and Lantuèjoul, 1979), binary image of coffee beans (Vincent and Beucher, 1989) and in biological studies of clustered nuclei (Norberto et al., 1997). In order to be able to apply this algorithm to detect lines dividing clustered objects, two prerequisites are required:

1. The original image has to be transformed into a different image, where following the topographical 'crest lines' correspond to the original image object boundaries and their inner and outer parts to 'valleys', and
2. Singular markers are defined on every valley of the transformed image as starting points of the flooding process.

An incorrect choice of the image transformation usually leads to incorrect segmentation, and failure in assigning a single marker to each valley of the transformed image leads to over segmentation. A number of different marking techniques were evaluated with the objective of identifying individual single crystals uniquely. In the next sections we present various marking techniques that have been used to transform the image before the application of watershed segmentation.

## 4.4 Image Processing Algorithms

The flow diagram in Figure 4.1 depicts the steps used to segment the crystal images. The acquired RGB color image was converted to a grey level image by averaging the

intensity levels in each of the R, G, B channels. This was followed by histogram equalization to spread the pixel values to all possible grey levels (i.e. 0 - 225). An automatic

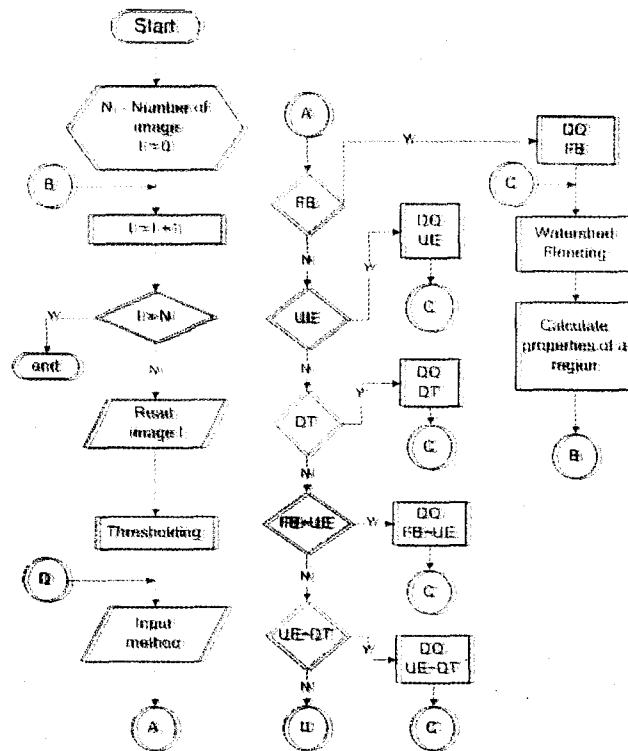


Figure 4.1. Flow diagram showing the steps used to segment the crystal images. The acquired image is binarized using Otsu's thresholding method and then marked using UE, DT, FB or a combination of those techniques. Finally watershed flooding is applied to determine the crest lines which separate the objects from each other and from the background.

thresholding function was applied to binarize the greyscale images. The threshold value was computed using a method described by Otsu (1979) which is based on calculating and comparing the between class variances and finally by choosing the one which gives the maximum between class variance. This segments the foreground from the background except for some foreground pixels which are misclassified as background. Misclassified foreground pixels cause holes on the object. Filling the holes using morphological operators binarize the image with the objects that have a pixel intensity of 1 and a background value of 0. All the above steps are common for all five algorithms developed. They differ from each other with the type of markers used to mark the crystals. The three markers (i.e distance transformation, ultimate

erosion and regional maxima) and their combinations were evaluated to uniquely identify individual crystal.

#### **4.4.1 Foreground and Background Marker**

A local maxima is used to mark the foreground. This is achieved by combining gray scale morphological erosion and dilation with gray scale reconstruction to maintain the original size of the crystals. By performing morphological erosion followed by dilation (morphological opening) all the connected components which do not contain the size of the structural element are filtered out whilst at the same time preserving the other components. The morphological dilation, which is the first operation of morphological opening, in the greyscale assigns the pixel under question with the biggest intensity value of its neighborhood. The pixel intensity in the resulting image have the value greater than or equal to its value in the original image. The morphological erosion in the greyscale assigns the pixel under study with the smallest intensity value of the neighboring pixels. The overall effect of morphological opening in gray level image removes 'dark' spots which results in a brighter image. The local maxima of the resulting bright image used to mark the crystals. In some images the background as well as the crystals were marked. This is undesirable because the application of the watershed algorithm on those images introduces a region which does not correspond to a crystal. Figure 4.2 shows example for a part of background segmented as an object. Therefore, marking only the crystals is crucial for accurate segmentation.

#### **4.4.2 Ultimate Erosion as a Marker**

The ultimate erosion (UE) algorithm uses the last connected components to mark the crystals (Serra, 1982). The last connected component is obtained by repeatedly eroding the binary image using a structural element but stopping one step before the whole object disappears. In some cases, however, more than one marker per crystal can be produced. Direct application of watershed transformation will cause the problem of oversegmentation. Figure 4.3 shown a crystal marked by several markers and the resulting oversegmented crystal when watershed segmentation was applied. This problem was partially addressed by dilating the markers to join them.

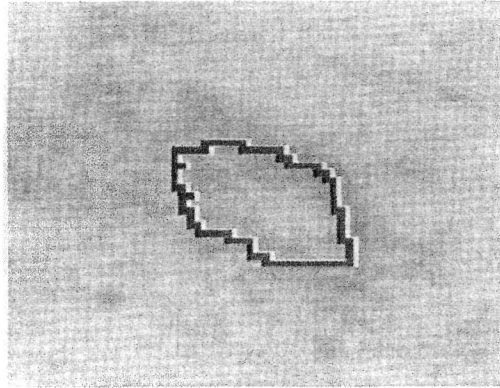


Figure 4.2. Example of background segmented as a foreground. This is the result of mismarking background as a foreground.

For some crystals, however, as the result of ultimate erosion their last connected components were so far apart from each other that a single morphological dilation could not join them and hence these crystals were oversegmented when watershed segmentation was applied. This is undesirable and this effect was minimized by combining this technique with DT and FB as described in Section 4.4.4.

#### 4.4.3 Distance Transform as a Marker

The distance transform (DT) method has been used in biological studies to mark clustered nuclei (Norberto et al., 1997). Distance function of binary image assigns every pixel with its distance to the background, i.e. to the closest pixel with value 0 assuming the foreground is 1. It can segment round shaped objects efficiently because the center of the object is the only point, equidistance from the background, marked as the maxima. Non convex objects are marked by more than one maxima which results in oversegmentation. This can introduce erroneous data when estimating some properties of a region such as its area. Combining this transformation with other (UE for example) improves the segmentation.

#### 4.4.4 Combining Markers

In some crystals, using the above techniques individually can produce crystals with more than one marker. As shown in Figure 4.3, this leads to an oversegmentation of the crystals when the watershed algorithm is applied. To minimize such occurrences,

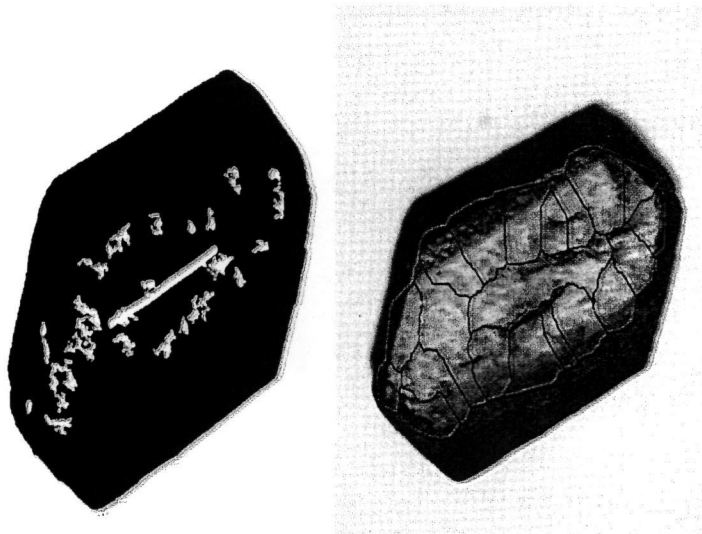


Figure 4.3. Example of a crystal image marked by several markers and the resulting image when watershed segmentation was applied

it is necessary to mark each object with only one marker. The above techniques were combined to attempt to ensure that there was only one marker for each crystal and to avoid mis-marking the background. It was found that the best combination was when ultimate erosion algorithm was combined with both the distance transform and background and foreground marker i.e. FB+UE and UE+DT.

Finally watershed function was applied to determine the crest lines which separate the objects from each other and from the background. Figure 4.4 indicates how well these algorithms segment a sample crystal. When the ultimate erosion was combined with distance transform (UE+DT), this gave the best segmentation, since the contour most closely coincides with the visible border. Foreground and background (FB), ultimate erosion (UE) and their combination(FB+UE), however, underestimated the sample crystal. Although distance transform (DT) gave good segmentation for this particular crystal, there was a problem of oversegmentation for some crystals which were marked more than a single marker. Evaluation of these algorithms, as described in Section 4.6, UE+DT showed better performance because it was better in marking crystal with a single marker.



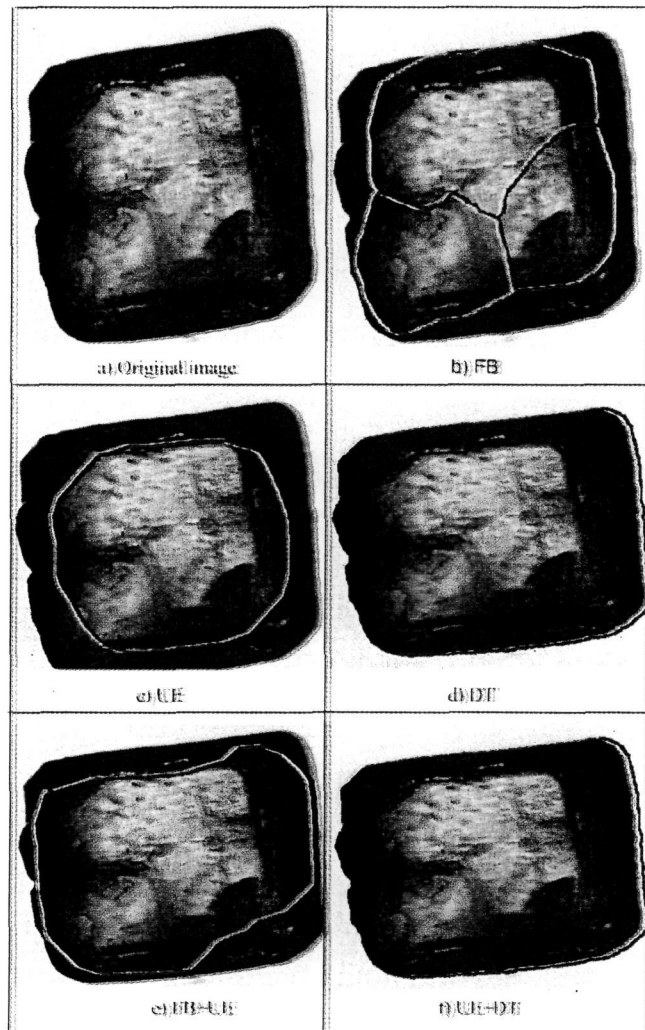


Figure 4.4. These are examples to illustrate how well the algorithms segment a sample crystal (a) from the background. The distance transform gives the best result when combined with ultimate erosion. The individual algorithms FB (b), UE(c) and DT (d) in addition (FB+UE) underestimates the area of the crystal.

## 4.5 Manual Clicking

One possible method to score the accuracy of a segmentation process is to manually determine the boundaries of all the crystals and compare these results with those obtained by the automatic algorithms. A clicker software program was written to allow the individual boundary of crystals to be manually traced using the mouse cursor. A complete contour was found by clicking on the corner pixels of the crystals. By so doing the individual crystals, touching and overlapping crystals were segmented from the background and from each other. The manually segmented crystals were further analyzed to calculate the area, length, and width of each crystal. Although the use of this program was tedious it was considered to offer the best ground truth against which the automatic algorithms could be benchmarked.

## 4.6 Accuracy of the Segmentation Algorithm

The MA and CV of 25 sugar samples, calculated from crystals image, were compared with the manually clicked technique to evaluate the accuracy of the segmentation algorithm for each of the 25 crystal images. Three algorithms for segmenting the crystal images have been evaluated. These include the foreground and background marker (FB), ultimate erosion (UE) and the distance transform (DT) methods. In addition, efforts were made to evaluate various combinations of these algorithms to enhance the accuracy. A measure of the accuracy can be defined as the average percentage error,  $\varepsilon$

$$\varepsilon(\%) = \left[ \frac{\sum_{i=1}^N \frac{|P_i - C_i|}{C_i}}{N} \right] \times 100\% \quad (4.1)$$

where  $P_i$  is the predicted MA or CV of the  $i$ -th image using one or a combination of the three algorithms,  $C_i$  is the MA or CV of the  $i$ -th image determined by manually clicking and  $N$  is the number of images. Equation 4.1 can be used to quantify the % error in measuring either MA or CV and the corresponding errors will be designated  $\varepsilon_{MA}$  and  $\varepsilon_{CV}$  respectively. Table 1 shows the values of  $\varepsilon_{MA}$  for the different algorithms. The error achieved by applying UE+DT is  $\varepsilon_{MA} = 5.45\%$  and is significantly better than that achieved by the other options. Because the combination of ultimate erosion and the distance transform (UE+DT) produced the smallest mean error, it was used for the rest of the analysis. Figure 4.5 indicates the number of crystals

Table 4.1. Average percentage error in mean aperture MA, calculated after applying the segmentation algorithms BF, UE and DT and the two combinations BF+UE and UE+DT.

	FB	UE	DT	FB+UE	UE+DT
$\epsilon_{MA}(\%)$	48.5	33.4	17.2	16.5	5.5

segmented using manual clicking and the UE+DT algorithm and Figure 4.6 shows the percentage error. In most of the images, the number of crystals segmented by UE+DT is fewer than manual. One reason for this was that fragmented small crystals were removed by the morphological operators. Also in some images the crystals touching the edge of the image were excluded by the segmentation algorithms, whilst some of them were included when the crystals were manually clicked. However, it could be argued that if some crystals are randomly removed from the images by the automatic algorithm, then the distribution would not be affected very much, and so it is still meaningful to compare the MA and CV obtained by the segmentation algorithms and the clicker program.

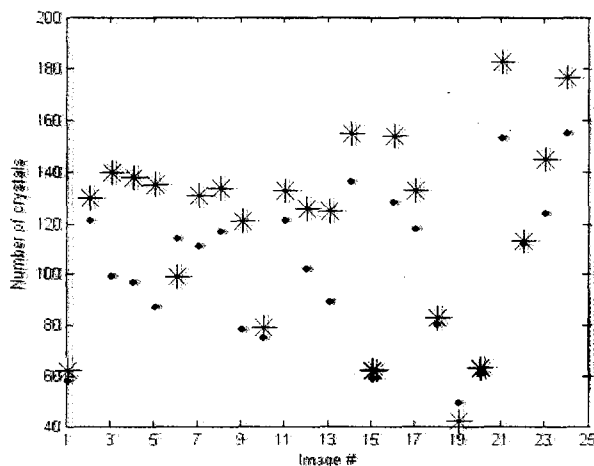


Figure 4.5. The number of crystals segmented using UE+DT (dot) and manually (star) for each of the crystal images. In most images the number of crystals identified by the algorithm is less than the manual method since the algorithm rejected small fragmented crystals.

An image (image #23) was randomly chosen from 25 crystal images and analyzed to evaluate the accuracy of the UE+DT in terms of the area of the crystals. Figure 4.7 shows crystal contours segmented by UE+DT overplotted on the original image. Crystals touching the edge of the image were rejected by the segmentation algorithm. Although this reduce the number of crystals segmented, it was desirable to clean all the crystals touching the border of the image. If the crystals touching the border of

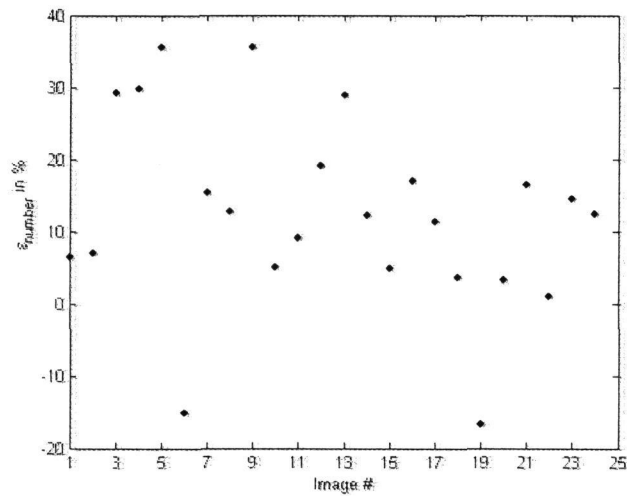


Figure 4.6. Percentage error in the number of crystals segmented using UE+DT and manually. In most images the number of crystals segmented by UE+DT is lower than manual.

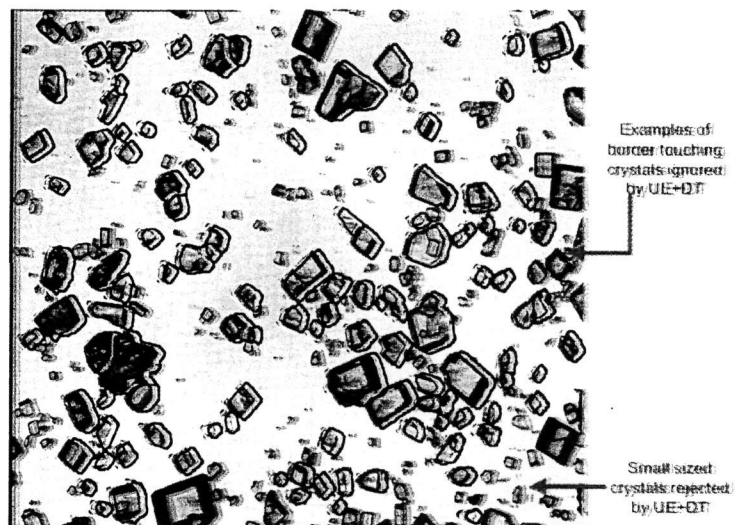


Figure 4.7. Crystal contours overplotted on the original image (image #23) after segmented using UE+DT. Crystals touching the edge of the image and small sized crystals were rejected (shown by the arrows).

the image were included in the analysis, they would introduce erroneous data. The reason for this is that the area of the crystals touching the border of the crystals can not be calculated accurately. To alleviate this problem, these crystals will either be removed or ignored during the analysis. Figure 4.7 shows example of such border crystals. Figure 4.7 also shows other ignored examples where crystals which were fully within the image but joined with other crystals which were themselves touching the border. Furthermore crystals whose size was smaller than the size of the structural elements used in the algorithm were also not considered. By ignoring these categories of crystals, discrepancy between the number of crystals segmented by the automatic and clicking methods was removed. One can capture a number of images from the same sample to get as many number (say 1000 crystals) of crystals required to calculate crystal size parameters. In this particular image 90 crystals were segmented.

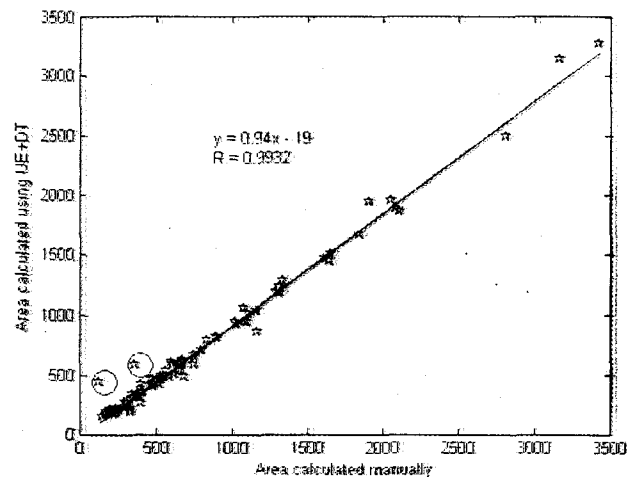


Figure 4.8. Scatter plot for the area of crystals analyzed in an image. The abscissa is area calculated manually and the ordinate represents the area calculated using UE+DT. The line is the least square fitted curve with the coefficient of 0.94 and -19. Generally the segmenting algorithm slightly underestimates the area of the crystals. Few outliers are circled.

To evaluate the performance of the UE+DT algorithm, the area of each crystal calculated using UE+DT compared with the area calculated manually. Figure 4.8 shows a scatter plot for the area computed manually and segmentation algorithm after removing the crystals that are not considered by UE+DT. The least square fitted curve with the regression coefficients of 0.94 and -19 approximate the data. A strong correlation, with a correlation coefficient  $R = 0.9932$ , was observed. The fact that there are not many outliers observed in the plot is evidence that the area of the crystals is being accurately estimated using the segmentation algorithm. The percentage difference in the area computed using UE+DT and manually is depicted

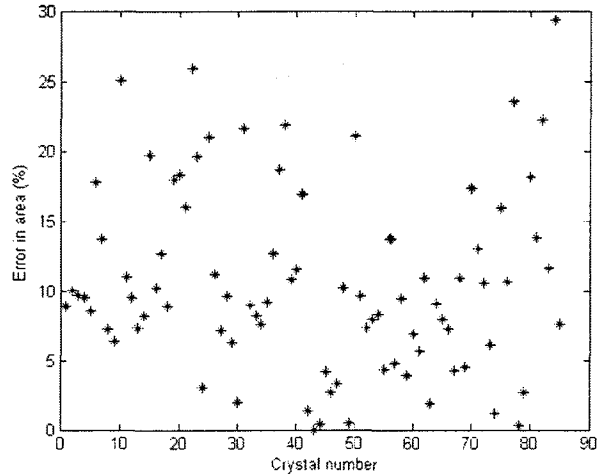


Figure 4.9. Scatter plot of the percentage error in the area computed using UE+DT and manually for each of the crystals in in image # 23. For most crystals UE+DT underestimates their area with an average percentage of error approximately 10.

in Figure 4.9. In most incidences the segmentation algorithm underestimates the area with  $\varepsilon_{Area} \approx 10$ . Figure 4.10 and Figure 4.11 are frequency of distribution for the crystals whose area were calculated using UE+DT and manually respectively.

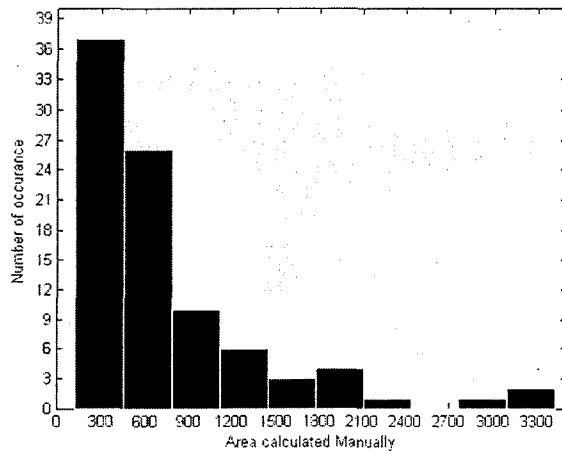


Figure 4.10. Frequency distribution for the crystals (in image #23) whose area calculated manually after excluding the crystals that were not segmented by UE+DT.

The distribution has roughly the same values of skewness with 2.00 for manually clicking and 2.14 for the UE+DT. Figure 4.12 shows a scatter plot for the mean size defined as the mean of the square root ( $\sqrt{A}$ ) of the area for 25 images calculated manually and using UE+DT. The best fitted straight line have a linear regression co-

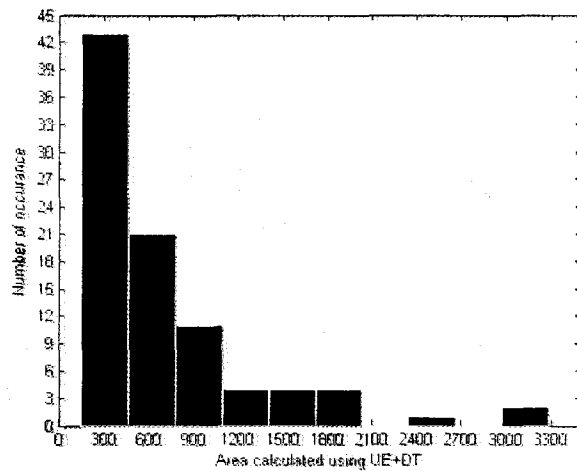


Figure 4.11. Frequency distribution for the crystals (in image #23) whose area calculated using UE+DT.

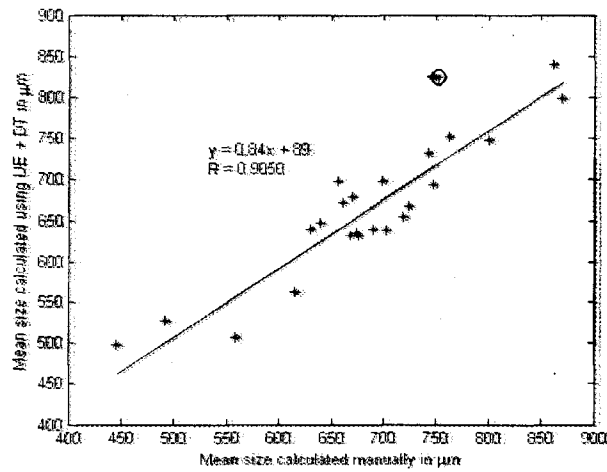


Figure 4.12. Scatter plot of the mean size defined as the mean of the square root of the area ( $\sqrt{A}$ ) of the crystals calculated for each of the 25 images.

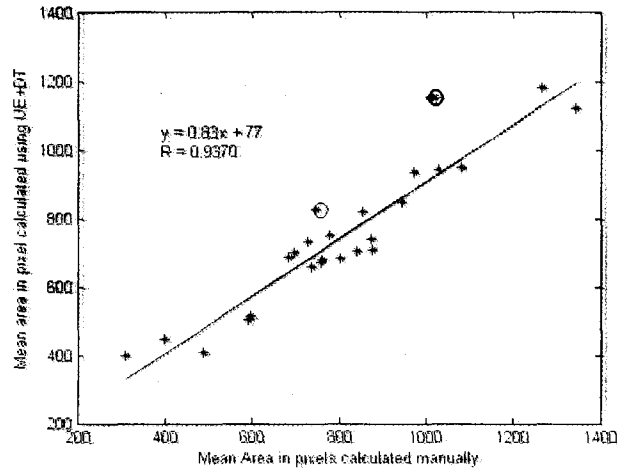


Figure 4.13. Scatter plot for the mean area calculated for all the crystals in each of 25 images. On the vertical axis is the mean area predicted using UE+DT and on the horizontal axis is the mean area calculated manually by clicking the individual crystal in each image.

efficients of 0.84 and 89 with fairly good correlation of value  $R = 0.9050$ . Figure 4.13 shows the predicted mean area versus the mean area calculated using manually clicking from crystal images. The scatter plot is shown together with the best fit straight line and the corresponding linear regression coefficients. The best fit straight line has a slope of 0.83 and has an offset of 77. There are few outliers which are circled. Upon closer investigation of those images it was found that they either contained a number of overlapping or fragmented crystals which were included in the manual clicking but rejected by the algorithm. The mean  $\varepsilon_{Area}$  was 9.63%. This is lower than the result of 12.9% reported by Mhlongo and Alport (2002). However a more meaningful comparison of these two algorithms would require them to be tested on the same sets of images. MA for the crystal size distribution, shown in Figure 4.14, was estimated using the Rens method. To find MA from the images, the crystals area was computed using UE+DT and this was converted to a mass distribution (assuming all crystals have the same density) and the cumulative percentage by mass was calculated. The mass distribution was computed for 30 equally spaced bin sizes. Fairly good correlation ( $R = 0.9286$ ) was observed with regression coefficients of 0.92 and 61.



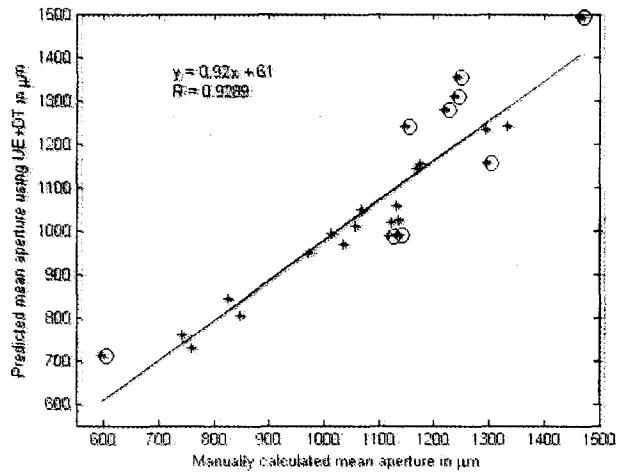


Figure 4.14. Scatter plot of MA for each of the 25 crystal images. The values on the vertical axis were calculated using UE+DT and the horizontal values were calculated by manually clicking the individual crystals. The best-fit straight line has coefficients of 0.92 and 61.

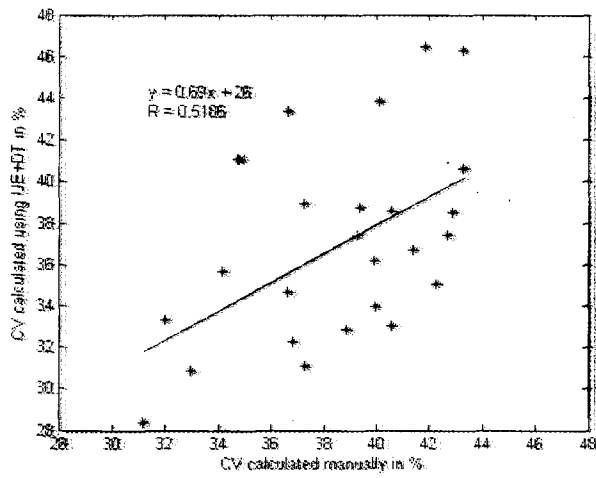


Figure 4.15. Scatter plot for CV. The vertical axis shows the predicted value and the horizontal axis is calculated manually from the crystal images.

However, as shown in Figure 4.15, CV is poorly estimated and there is a much larger scatter of the points. Thus, it appears that the crystals that are being removed by the DT+UE algorithm is affecting the shape of the distribution function. To verify this, the crystal size distributions for the randomly chosen image (image #23) calculated by UE+DT and manual techniques were compared for their shape. Comparing Figure 4.16 and 4.17, it is evident that the shape of the distributions is not the same. It can also be seen that the distribution calculated manually skewed to the right, indicating that more small sized crystals were considered that were not by UE+DT.

Both size distribution are non-normal. As described in Chapter 2, Rens distribution works better for such distribution. Applying Rens method CV was calculated to be 41% for the UE+DT and 37% manually. The percentage error in CV for all 25 images is shown in Figure 4.18. The mean absolute error in CV  $\varepsilon_{CV} \approx 12\%$ .

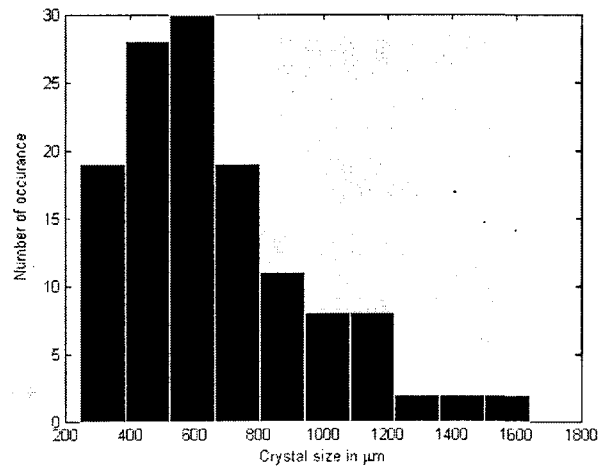


Figure 4.16. Frequency of occurrence for crystal size, defined as  $\sqrt{A}$ , distribution calculated manually.

## 4.7 Discussion and Conclusion

The results of an automated classical image processing technique has been developed to estimate the crystal size parameters MA and CV as a possible alternative to the usual sieving technique that is used in the production environment. Although a number of segmentation algorithms were evaluated, it was found that a combination of ultimate erosion and the distance transform, (UE+DT), was the most accurate in finding the crystal boundaries.

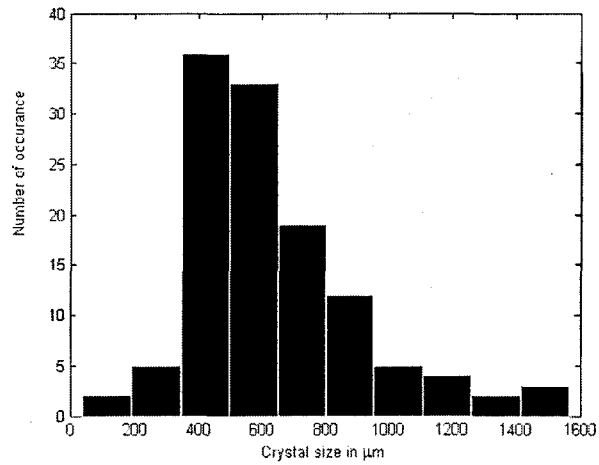


Figure 4.17. Frequency of occurrence for crystal size, defined as  $\sqrt{A}$ , distribution calculated using UE+DT.

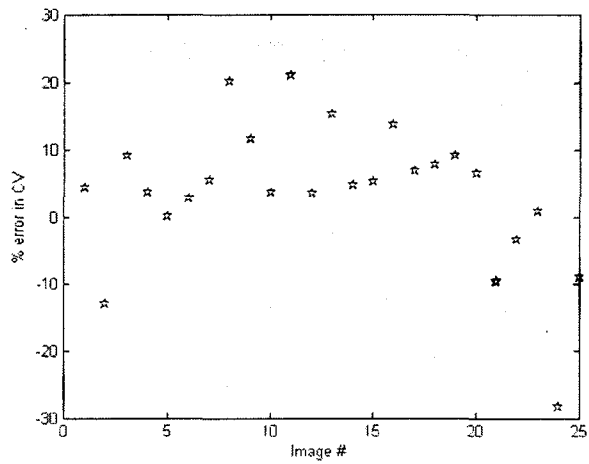


Figure 4.18. Percentage error in CV calculated using UE+DT and manual. The average absolute error of 12 %.

Watershed segmentation was employed to segment clustered, just touching and overlapping crystals. Using dry crystal samples obtained from a refinery, the MA and CV were calculated for each of 25 sample images using the Rens method. These results were compared with those obtained by manually clicking on the crystal boundaries. Figure 4.8 shows a scatter plot for the area of crystals calculated for image #23. Although the area of the crystals calculated using UE+DT and manual clicking method exhibited a strong correlation ( $R = 0.9932$ ), the slope of the graph was not 1:1. In most cases the automatic algorithm underestimated the area of the crystals. The problem of oversegmentation which resulted from marking crystals with more than one marker can account for the differences between the areas calculated by the algorithm and manual methods. Such discrepancies in the area, however, were also observed for crystals that were marked using a single marker. This is attributed to the lack of an efficient algorithm to trace the exact boundary of the objects (foreground) in an image with low contrast. In the UE+DT algorithm, the images were contrast stretched to ensure that all the greyscale levels were used. The results shown in Figure 4.8 were found using images with low contrast and hence exhibited very little greyscale differences between the foreground and background. This problem was caused by the image capture technique which involved using transmitted light. The images could also be captured using reflected light by spreading the crystals on a dark background. This would have the effect of increasing the contrast and hence enable the crystal boundaries to be traced more accurately. The discrepancies in Figure 4.12 and 4.13 are also attributed to the problems the algorithm experienced in tracing the boundaries of low contrast images. This problem also limited the accuracy of crystals size parameter calculated in the subsequent analysis. Despite this MA showed fairly good correlation with an average percentage error of  $\varepsilon_{MA} \approx 6\%$ . This result is slightly better than the earlier one reported by Mhlongo and Alport (2002) using wavelets and neural networks. However there was more scatter in the CV results possibly indicating that the crystals that were eliminated by the UE+DT algorithm this because they were either at the edge of the image, or too fragmented some overlapping crystals were oversegmented was having an effect on the crystal size distribution.

By taking multiples of crystal images of each sample can increase the total number of crystals analyzed in each sample. Overlapping crystals can be identified using a

curvature measure and optimizing the morphological operators can retain fragmented crystals.

Chapter 5 will present a technique which identifies and rejects overlapping crystals based on their convexity measures. This method could preserve fragmented crystals that would be otherwise eroded when the watershed algorithm was applied.

# Chapter 5

## Use of Convexity to Remove Overlapping Crystals

### 5.1 Introduction

In Chapter 4, 5 algorithms were evaluated for crystal sizing. Sugar crystals were segmented and separated first by marking and then using the watershed transformation. It was demonstrated that the combination of ultimate erosion and distance transformation (UE+DT) performed better than the other methods. In this chapter, another algorithm is developed and evaluated. Due to the fact that there is a difference in shape between overlapping and non overlapping crystals, this technique used two convexity measures.

Shape is a crucial feature in many areas of image analysis, including for example, the particle shape analysis of coarse aggregate (Kwan et al., 1999) and in the pharmaceutical industry for the automatic inspection of tablets (Derganc et al., 2003). It has also been used to detect elliptical objects in remote sensing (Zhu and Wang, 2004). In addition to the basic descriptors of shape including compactness, circularity, and rectangularity (Sonka et al., 1998), the convexity of polygons is also considered as one of basic descriptors of shape as described by Zunic and Rosin (2004). Convexity measure has been used for a variety of applications, including for instance shape decomposition (Latecki and Lakamper, 1999). The concept of shape decomposition based on convexity measure was used to improve the measurement of the crystal size distribution. In this study, the convexity measure was used to identify and exclude

occluded sugar crystals in the captured image. This technique reduces erroneous data that could be introduced if overlapping crystals were included in the subsequent size measurements and determination of the crystal size distribution.

After short introduction about contour tracing, convex hull algorithm used in this work will be described. The two common measures of convexity based on perimeter and area are used to classify the sugar crystals as overlapping or non overlapping. The classification accuracy was also evaluated using the Receiver Operating Characteristics curve (ROC). MA and CV were then calculated using this improved technique and were compared with the same parameters calculated using the manual method.

## 5.2 Contour Tracing

One method of finding and analyzing the contour of a connected component in an image is to scan it until a border pixel of a component is found and subsequently to trace the boundary until the entire boundary is obtained. Such a procedure is referred to as contour tracing. There is no standard formal definition given to the boundary of a connected component. Generally the boundary of the object is that which seems reasonable to humans and algorithms are judged according to how well they agree with human perception. However a border finding algorithm can be precisely implemented by defining ‘border’ points which are intimately related to the boundary. A connected component of a black pixel  $P$ , in Figure 3.1, is a 4-border point if at least one of its 4-neighbors is white. It is an 8-border point if at least one of its 8-neighbors is white. The boundary tracing algorithm implemented in this work is adopted from Sonka et al. (1998). The algorithm scans the image until it finds the first object pixel, depending on the kind of neighborhood required, then searches for the boundary pixel of the object in the counter clockwise direction.

### The Boundary Tracing Algorithm

The boundary tracing algorithm can be defined by the following steps:

1. Search the image from top left until a pixel of a new region is found. This pixel  $P_0$  has the minimum column value of all pixels of that region having the minimum row value. Pixel  $P_0$  is a starting pixel of that region’s border. Define

a variable  $dir$  which stores the direction of the previous move along the border from the previous border element to the current boarder element. Assign

- (a)  $dir = 3$  if the detected border has 4 - connectivity (Figure 5.1a).
  - (b)  $dir = 7$  if the detected border has 8 - connectivity (Figure 5.1b).
2. Search the  $3 \times 3$  neighborhood of the current pixel in an anti-clockwise direction. Begin the neighborhood search in the pixel positioned in the direction:
- (a)  $(dir + 3) \bmod 4$  (Figure 5.1c).
  - (b)  $(dir + 7) \bmod 8$  if  $dir$  is even (Figure 5.1d).
  - $(dir + 6) \bmod 8$  if  $dir$  is odd (Figure 5.1e).
- The first pixel found with the same value as the current pixel is a new boundary element  $P_n$ . Update the  $dir$  value.
3. If the current boundary element  $P_n$  is equal to the second border element  $P_1$ , and if the previous border element  $P_{n-1}$  is equal to  $P_0$ , stop. Otherwise repeat step 2.

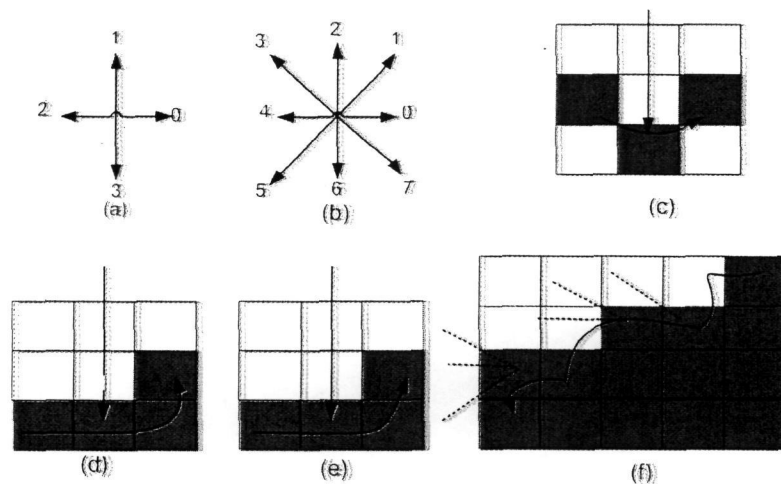


Figure 5.1. Boundary tracing: (a) direction notation for 4-connectivity; (b) direction notation for 8-connectivity; (c) pixel neighborhood search sequence in 4-connectivity; (d),(e) search sequence in 8-connectivity; (f) boundary tracing in 8-connectivity (dashed lines show pixels tested during the border tracing)



### 5.3 Convex Hull

A convex hull is a concept used to describe the topological properties of an object. The convex hull is the smallest region which contains the object such that any two points of the region can be connected by a straight line, all points of which belong to the region. For example consider an object whose shape resembles the one shown in Figure 5.2. Imagine a thin rubber band pulled around the object, then the shape of the rubber band provides the convex hull of the object (Sonka et al., 1998).

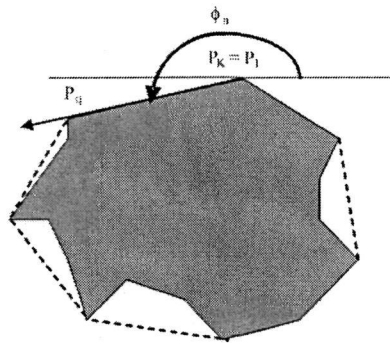


Figure 5.2. An example region (shaded grey) together with its convex hull (region bounded by dashed line) which is formed by a rubber band if it were to be placed around the region. Beginning at a point  $P_1$  on the boundary, and moving in an anti-clockwise direction the next point on the convex hull,  $P_q$  is found when the angle formed by the vector  $\overline{P_1 P_q}$  is a minimum. This process is then repeated.

#### Algorithm to construct the convex hull of a region

1. Find all pixels of a region with minimum row coordinate, among them, find the pixel  $P_1$ , with the minimum column coordinate. Assign  $P_k = P_1$ .
2. Search the region boundary in an anti-clockwise direction and compute the orientation angle  $\phi_n$  for every boundary point  $P_n$  which lies after the point  $P_k$  (in the direction of boundary search) as in Figure 5.2.  $\phi_n$  is the angle the vector (formed by joining pixel  $P_k$  to pixel  $P_n$ ) makes with the x axis. The point  $P_q$  satisfying the condition  $\phi_q = \min(\phi_n)$  is an element (vertex) of the region convex hull.
3. Assign  $P_k = P_q$
4. Repeat steps 2 and 3 until  $P_k = P_1$ .

## 5.4 Convexity Measure

Two common parameters that have been used to characterise the convexity of a shape are based on the area and perimeter of the object. Area based convexity,  $C_A$ , is defined for a given shape  $S$  as the ratio of the area of the region to the area of the corresponding convex hull, i.e

$$C_A(S) = \frac{A(S)}{A(CH(S))} \quad (5.1)$$

where  $A(S)$  and  $A(CH(S))$  are the area of the shape and its convex hull respectively. The second measure  $C_P$ , depends on the perimeter of the shape and its convex hull, and is defined as

$$C_P(S) = \frac{P(CH(S))}{P(S)} \quad (5.2)$$

where  $P(S)$  and  $P(CH(S))$  are the perimeter of the shape and its convex hull respectively. Both convexity measures have a number of desirable properties. They are:

1. in the range 0 to 1.
2. equal 1 if and only if the shape is convex.
3. invariant under similarity transformations.
4. There are shapes whose convexity measure is arbitrarily close to 0.

We will now describe how these two convexity measures have been used to exclude occluded crystals in captured images of sugar samples. The performance of two class classification of crystals has been evaluated using the Receiver Operating Characteristics (ROC) curve generated by varying the threshold values of the convexity measures. The value of the area under the curve (AUC) is then used to categorize a classifier as either random or nonrandom (Fawcett, 2006).

## 5.5 Evaluation of the Two Class Classifiers Using the ROC Curve

The ROC curve has long been used in signal detection theory. Originally it was conceived during World War II to assess the capabilities of radar systems in distinguishing random interference (noise) from actual targets (Swets et al., 2000). ROC has been employed in medical decision making, diagnosis and in particular imaging. Bradley (1997) showed how ROC curves and particularly AUC could be used for evaluating the quality of dichotomizers. There does not appear to be any other literature describing the use of ROC to evaluate techniques to measure the crystal size distribution in the sugar industry. One can use ROC curves as an effective way to evaluate performance of a classifier to separate overlapping and non overlapping crystals based on their convexity measure.

### 5.5.1 AUC as a Performance Measure

The test of a classification scheme requires the knowledge of the correct and incorrect classifications from each class. This information is then normally displayed in a confusion matrix, also called contingency table. A confusion matrix is a table showing the difference between the actual and predicted classes using a particular discriminating function as shown in the Table 5.1. In Table 5.1,  $T_p$  and  $T_n$  are the

Table 5.1. Confusion Matrix

Actual	Predicted		
	Non overlapping	Overlapping	
Non overlapping	$T_n$	$F_p$	$C_n$
Overlapping	$F_n$	$T_p$	$C_p$
	$R_n$	$R_p$	

number (or %) of actual non overlapping and overlapping crystals respectively,  $F_p$  and  $F_n$  are the numbers (or %) of misclassified overlapping and non overlapping respectively. The row totals,  $C_n$  and  $C_p$  are the number of actual non overlapping and overlapping crystals, and the column totals,  $R_n$  and  $R_p$ , are the number of predicted non overlapping and overlapping crystals. If  $N$  is the total number of crystals then

$N = C_n + C_p = R_n + R_p$ . The actual non overlapping rate (also called hit rate and recall) of a classifier is estimated as

$$TPR = \frac{T_p}{C_p} \quad (5.3)$$

The misclassified overlapping rate (also called false alarm rate) of the classifier is

$$FPR = \frac{F_p}{C_n} \quad (5.4)$$

Additional terms associated with ROC curves are the

$$\text{sensitivity} = TPR \quad (5.5)$$

and

$$\text{specificity} = \frac{T_p}{C_n} = 1 - FPR \quad (5.6)$$

All of these measures of performance are valid only for one particular operating point, which is normally chosen so as to minimize the error probability. Often, however, the area under the operating characteristics curve is used to measure the performance of the two class classifier. The ROC curves are the plots of  $TPR$  versus  $FPR$  as the decision threshold is varied (Bradley, 1997). The  $AUC$  can be computed by applying trapezoidal rule using the following equation:

$$AUC = \sum_i (FPR_i - FPR_{(i-1)}) \times TPR_{(i-1)} + \frac{1}{2} (TPR_i - TPR_{(i-1)}) \times (FPR_i - FPR_{(i-1)}) \quad (5.7)$$

The perfect classifier, which traverses the point  $TPR = TNR = 1$ , has  $AUC = 1$ , while a classifier with ROC curve along the line of the 'uselessness', refers to the diagonal of ROC curve, has  $AUC = 0.5$ . The latter result is referred to as a random classifier (Fawcett, 2006).

## 5.6 Segmentation and Calculating Convexity

### 5.6.1 Segmentation of Crystals

All 25 crystal images, used in Chapter 4, were analysed to test the performance of the convexity technique. The imaging system contained a CCD camera attached to the microscope as explained in chapter 4. The crystals in the image were deliberately made to have different spacial configuration such as touching, overlapping and non overlapping to mimic what could have been if the image was taken in the production environment. The images were processed to segment the crystals from the background using the technique explained in Chapter 4 Section 4.4. This involved converting the images to their grey level equivalent and then thresholding. Once the images had been segmented the discriminated crystals were measured and analyzed. The parameters that were measured included their length, width, area, perimeter in addition to the convexity measure  $C_A$  and  $C_P$ .  $C_A$  and  $C_P$  were then used to identify and reject overlapping crystals. Figure 5.3 shows a flow diagram of the algorithm.

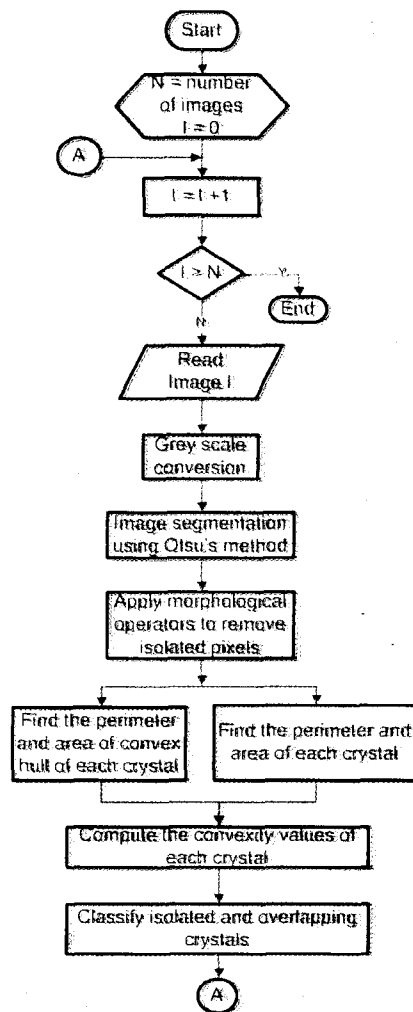


Figure 5.3. Flow diagram showing the steps used to segment the crystal images using the convexity measures. The acquired image was binarized using Otsu's thresholding method and morphological operators and then the areas and perimeters of the connected component and convex hull were calculated. Finally the convexity measures, based on the areas and perimeters, were calculated and threshold values were applied to identify and reject overlapping crystals.

### 5.6.2 Calculation of Convexity Measures

The contour tracing algorithm described in Section 5.2 was used and Figure 5.4 shows an example of the boundary pixels overplotted on a segmented images. However some problems arose when trying to find boundary pixels for connected crystal shapes. For two just touching connected components, where there were a few pixels joining them, the algorithm traced only one of them and rejected the other if 4 connectivity was used. There was no such problem for 8 connectivity. This was expected because for two just touching crystals if they are not connected in 4 neighborhood, they must be connected in 8 neighborhood as 4 connectivity is a subset of 8 connectivity. Ignoring this limitation for the moment, the contours were then used to calculate

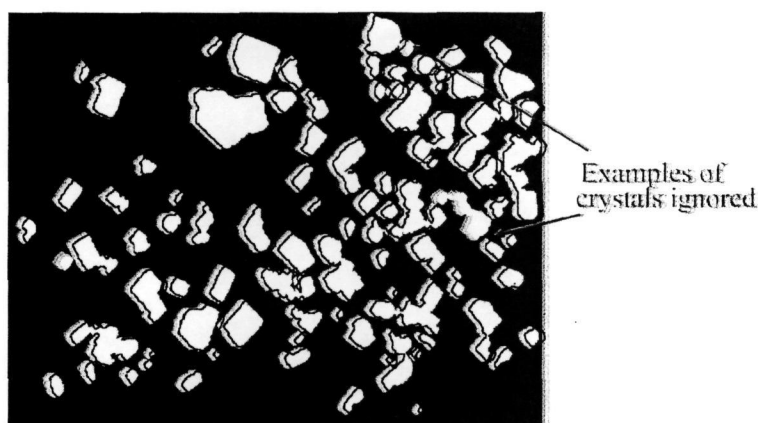


Figure 5.4. An example crystal image showing the individual crystals, together with their individual contours. This example also shows that some crystals could be ignored by the algorithm when they were joined by a few pixels.

the convex hulls of the region for each of the shapes as shown in Figure 5.5 using the convex hull algorithm described in Section 5.3. However, it was also observed that two independent neighboring connected components could have convex hulls that overlapped. Figure 5.6 illustrates a number of such examples. This is undesirable when one tries to calculate areas and perimeters. To alleviate these two problems, the area and perimeter of each crystal were calculated immediately after its convex hull had been found. The other problem that was observed was that a small convex hull can be completely contained within a larger one. This was also undesirable as some of the connected components disappeared when all the convex hulls of the objects were joined. Such problems were again addressed by calculating their area and perimeter immediately after finding the convex hull.

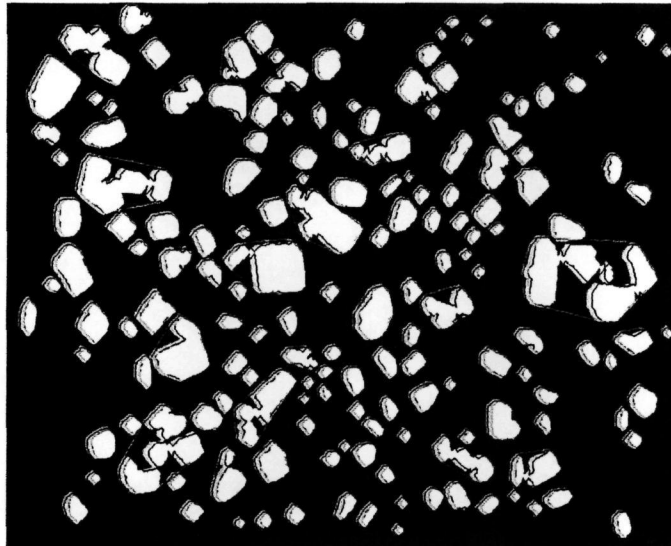


Figure 5.5. Convex hull of a connected component in blue color over plotted segmented image and traced contour in red.

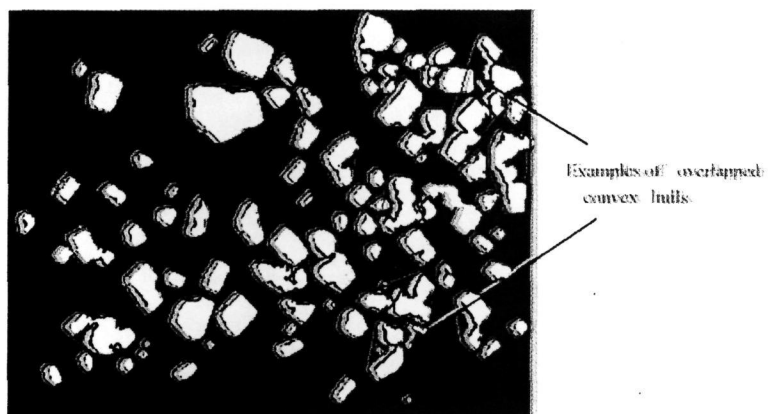


Figure 5.6. Examples of two independent neighboring connected components whose convex hulls overlapped. Red marks the boundaries and blue their convex hulls.



Once the perimeter and the area of the regions and their corresponding convex hull were calculated, the convexity measures,  $C_A$  and  $C_P$ , could be obtained.

### 5.6.3 Classification and Choice of Thresholds

If a common threshold value was chosen for  $C_A$  and  $C_P$ , then this produced a decrease (increase) in the number of non overlapping (overlapping) crystals as the threshold value increased as shown in Figure 5.7. This data was obtained from a randomly chosen image which contained 80 crystals (15 overlapping and 65 non overlapping) counted manually. For this particular image it was found that for the convexity values between 0 and 0.55 all the crystals were classified as non overlapping even though there were some overlapping crystals. The problem lies how to find the optimal threshold value which will most accurately separate the crystals into the two (overlapping and non overlapping) classes.

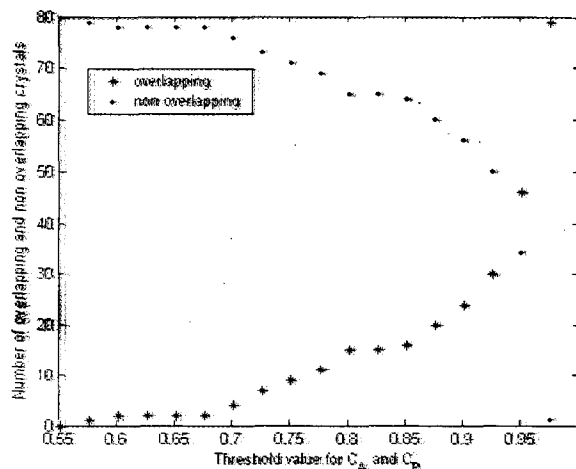


Figure 5.7. The graph shows the number of crystals classified as overlapping and non overlapping crystals. The convexity values ( $C_A$  and  $C_P$ ) vary from 0.55 to 1 in steps of 0.025. An image contained 80 crystals with 15 overlapping and 65 non overlapping which was counted manually.

Generally, it would be necessary to find some function of  $C_A$  and  $C_P$  which would optimally discriminate between these two classes (overlapping and non overlapping) of crystals, however, in this application it was found that a single common threshold value was sufficient. From Figure 5.8 it would be seen that a threshold value of  $C_A \sim 0.85$  or  $C_P \sim 0.85$  will correctly separate most of the crystals into the two classes. In

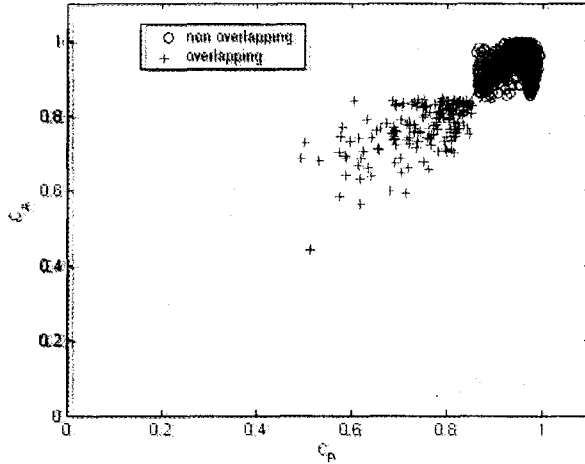


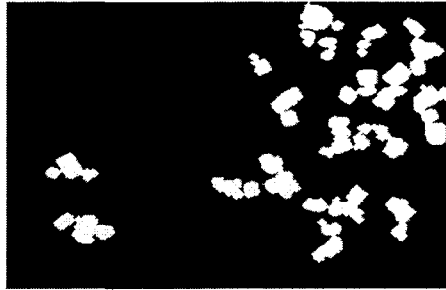
Figure 5.8. Scatter plot for convexity measures  $C_A$  and  $C_P$ . Overlapping crystals are marked as '+' and non overlapping crystals are marked 'o'.

Chapter 6, a more objective technique for optimising the choice of threshold value, using Artificial Neural Network (ANN) and Support Vector Machines (SVM), is presented. It was, however, found that the choice of a common threshold value of  $C_A = C_P = 0.85$  gave an acceptable confusion matrix results. Table 5.2 shows the confusion matrix using convexity threshold values of  $C_A = C_P = 0.85$  for all the 2175 (1866 non overlapping and 309 overlapping crystals counted manually) crystals in the 25 images. Only a relatively few 21% or (67 out of 309) overlapping crystals were misclassified as non overlapping crystal. Figure 5.9(a and b) show the resulting

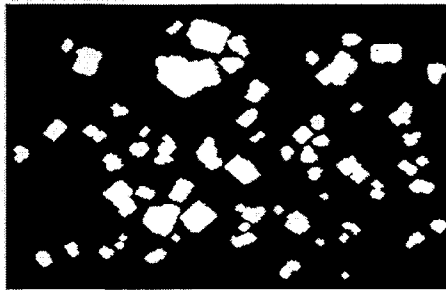
Table 5.2. Confusion matrix using convexity threshold values of  $C_A = C_P = 0.85$  for all the 2175 crystals in the 25 images.

Actual	Predicted	
	Non overlapping	Overlapping
Non overlapping (%)	100	0
Overlapping (%)	21	79

15 overlapping and 65 non overlapping crystals respectively when this convexity threshold applied to an image #11. For this example only 1 crystal was misclassified as being non overlapping.



a



b

Figure 5.9. The above images show an example of the result of a classifier of applying a convexity threshold value of  $C_A, C_P = 0.85$  to typical crystal image resulting in 15 overlapping crystals in (a) and 65 non overlapping crystals in (b).

#### 5.6.4 Classifier Accuracy using AUC

As mentioned in Section 5.5, the ROC curve is defined as a plot of  $TPR$  against  $FPR$  and was generated by varying the threshold value for the convexity measures. For each threshold value, varying between 0 and 1 in steps of 0.025, the corresponding  $TPR$  and  $FPR$  were calculated and the ROC curve was plotted. Figure 5.10 shows the ROC curve generated for the 25 crystal images used in this work. To draw the curve, first the number of overlapping and non overlapping crystals in the image were counted. This was taken to be the total actual non overlapping and overlapping which was used to evaluate the two classes. For each threshold the confusion matrix and hence the corresponding performance metrics were computed.  $AUC$  was computed using Equation 5.7 and found to be 0.99 which indicated that the classification was successfully discriminating between the two classes. This result suggested that the classifier could be confidently applied to identify and reject overlapping crystals in the crystal image.

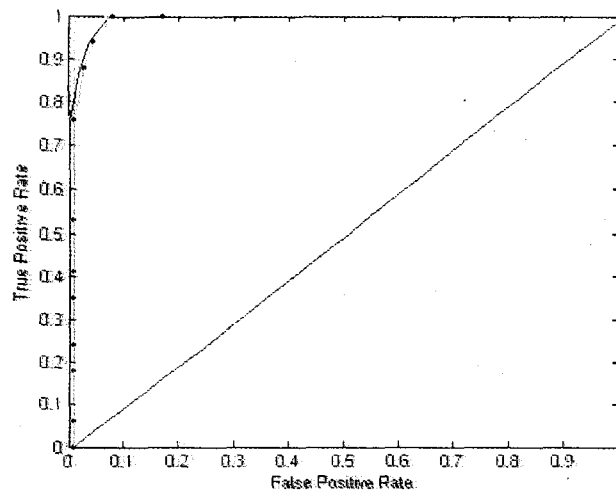


Figure 5.10. The ROC curve for a classification of the crystals into overlapping and non overlapping classes using different threshold values of the convexity measures  $C_A$  and  $C_P$  according to their convexity measure. The dotted plot represents the values computed for each confusion matrix with a line joins the points. The solid straight line represents the line of 'uselessness' which would result for no separation into classes.

### 5.6.5 Calculation of MA and CV

After removing the overlapping crystals, MA and CV were computed and compared with same parameters calculated by manually tracing the crystal borders using the mouse cursor. The Rens method was used to calculate crystal size parameter from the cumulative percentage by mass. Figure 5.11 shows the predicted mean size (af-

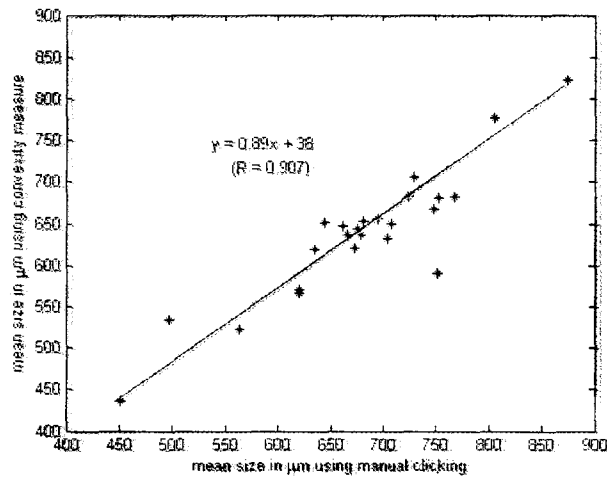


Figure 5.11. Scatter plot of mean size  $\sqrt{A}$  calculated for the 25 images. On the vertical axis is the mean size predicted after using convexity measure to automatically exclude overlapping crystals and the horizontal axis shows the mean size calculated by manually clicking around the individual crystals.

ter applying convexity based algorithm) versus the mean size obtained by manual tracing the boundaries. The scatter plot is shown together with the best line and the corresponding linear regression coefficients. The best fit straight line has a slope of 0.89, a small offset of 38 and a high correlation coefficient of 0.91. However there are few outliers. Upon closer investigation of those images it was found that they contained a number of overlapping crystals which were included in the manual clicking but rejected by the algorithm. This reduces the number of crystals remained in the image for further analysis. However, the problem can be alleviated by analyzing multiples of images from the same sugar sample.

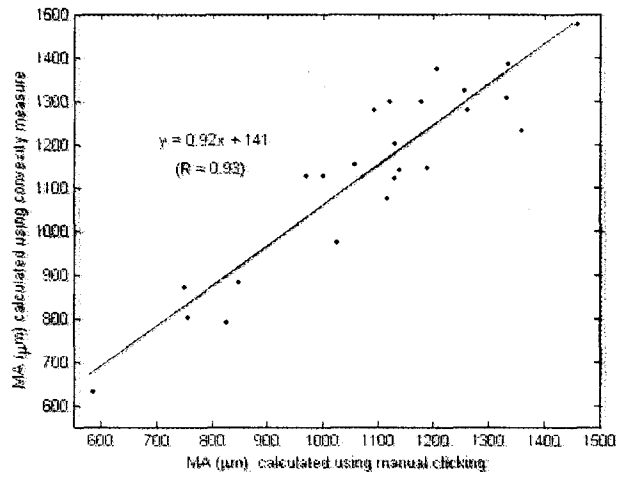


Figure 5.12. Scatter plot of MA for the 25 crystal images. The values on the vertical axis were calculated after removing overlapping crystals based on the convexity threshold and the horizontal values were calculated by manually clicking the individual crystals. The best-fit straight line has coefficients of 0.92 and 141.

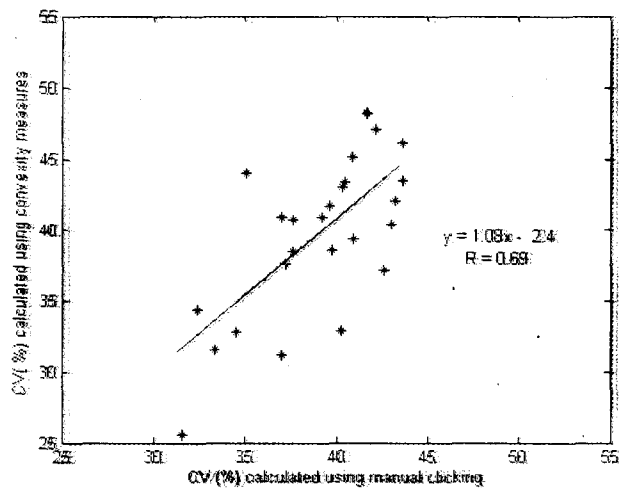


Figure 5.13. Scatter plot of CV for the 25 images. The values on the vertical axis were calculated after removing overlapping crystals based on the convexity threshold and the horizontal values were calculated by manually clicking the individual crystals.

To find MA, as described in Section 5.6.5, from the images, after applying convexity threshold, the crystal areas were computed and this was converted to a mass distribution and then to the percentage of crystals retained (cumulative). MA was then computed by applying Rens method for each crystal image. Referring to Figure 5.12 fairly good correlation, with  $R = 0.93$ , was observed. The best-fit straight line has coefficients of 0.92 and 141. The  $\varepsilon_{MA}$  was 7.75%. The scatter plot for CV, shown in the Figure 5.13, has a relatively low correlation coefficient,  $R = 0.69$ , nevertheless was larger than the previous value of  $R = 0.4$  found using ultimate erosion and distance transformation (UE+DT) (Argaw et al., 2006). The mean error in CV,  $\varepsilon_{CV} \approx 9.73\%$ , calculated using convexity based algorithm is lower than  $\varepsilon_{CV}$  calculated using UE+DT ( $\varepsilon_{CV} \approx 12\%$ ).

## 5.7 Discussion and Conclusion

An improved technique to determine MA and CV of sugar crystal size distributions using area and perimeter convexity measures to identify and reject overlapping crystals has been developed. The remaining non overlapping crystals were analyzed and the MA and CV were calculated. These parameters were measured for all 25 crystal images and compared with same parameters calculated using manual clicking on a captured image. Fairly good correlation, ( $R = 0.93$ ), has been obtained for MA and with a mean error of  $\varepsilon_{MA} = 7.75\%$ . A summary of the mean errors and correlation

Table 5.3. Summary of % errors and correlation coefficients for MA and CV after applying convexity based algorithm

	$\varepsilon(\%)$	R
MA	7.75	0.93
CV	9.73	0.69

coefficients for the convexity technique is shown in Table 5.3. Both MA and CV are calculated with an error of  $< 10\%$ . MA has a high correlation coefficient of 0.93 while CV has lower value. This low correlation coefficient of  $R = 0.69$  for CV needs to be more thoroughly investigated in order to validate the model that is being used. As shown in the confusion matrix (Table 5.2) 21% of the overlapping crystals were

misclassified as non overlapping. Although this only represented 67 out of 309 overlapping crystals, this could contribute to the errors. In chapter 6 classification results of crystals as overlapping and non overlapping using objective techniques viz ANN and SVM are presented.



# Chapter 6

## Application of ANNs and SVMs to Classify Crystals as Overlapping and Non-overlapping

### 6.1 Introduction

Overlapping and touching crystals compromise the accuracy of techniques to determine the size of sugar crystals using image processing. To improve the accuracy of crystals size measurement using crystals image processing, it is necessary that overlapping and touching crystals are identified and either excluded or separated. In Chapter 4, 5 algorithms, based on marker controlled watershed segmentation to separate crystals, were evaluated. However, these algorithms could not produce 100% separation of individual crystals resulting in some overlapping and touching crystals. It was also pointed out that convexity measures could be used to exclude overlapping and touching crystals. It was shown that a manual choice of the threshold value of convexity based on their area and perimeter was reasonably successful in classifying overlapping or non overlapping crystals. However, in order to explore whether more sophisticated techniques could improve the classification accuracy, two classification algorithms viz. Artificial Neural Networks (ANNs) and Support Vectors Machine (SVM) were evaluated. Both classifiers are characterized as non-parametric where a prior knowledge of the distribution of the data set is not required. Two convexity features, based on the individual crystal area and perimeter were used as input to the classifiers. The desired values of -1 for overlapping and 1 for non-overlapping, were assigned to the outputs. During training, in both cases, the RMS error for

weights and biases was set to 0.01. 60% of the data set was used for training and the remaining unseen 40% was used to test the network. The test data set contained 1941 non-overlapping and 311 overlapping crystals. In the next section the results obtained using these two classifiers (ANN and SVM) will be presented.

## 6.2 Artificial Neural Networks

Artificial Neural Networks have been successfully employed to solve a variety of computer vision problems. There are a number of different ANNs that use different configurations of their processing elements and training or learning rules. These rules specify an initial set of weights and indicate how weight should be modified during the learning process to improve network performance. The theory and representation of the various network types are motivated by the functionality and representation of biological neural networks. In this sense, processing units are usually referred to as neurons, while interconnections are called synaptic connections. Although different neural modes are known, all have the following basic components in common (Ritter and Wilson, 1996):

1. A finite set of neurons  $a_1, a_2, \dots, a_n$  with each neuron having a specific neural value at time  $t$ , which will be denoted by  $a_i(t)$ .
2. A finite set of neural connections  $W = W_{ij}$ , where  $W_{ij}$  denotes the strength of the connection of neuron  $a_i$  with neuron  $a_j$ .
3. A propagation rule  $\tau_i(t) = \sum_{j=1}^n a_j(t)W_{ij}$ .
4. An activation function  $f$ , which takes  $\tau$  as an input and produces the next state of the neuron  $a_i(t+1) = f(\tau_i(t) - \theta)$  where  $\theta$  is a threshold.  $f$  can be a hard limiter, threshold logic, or sigmoidal function, which introduces nonlinearity into the network.

## 6.3 Multilayer Perceptrons (MLPs)

Multilayer Perceptrons (MLPs) are one of the most successful types of ANNs. Typically the network consists of a set of processing units that constitute the input layer,

one or more hidden layers, and an output layer. The input signal propagates through the network in a forward direction, on a layer-by-layer basis. Figure 6.1 illustrates the configuration of the MLP. A node in a hidden layer is connected to every node in the layer above and below it. In Figure 6.1 weight  $W_{ij}$  connects input node  $x_i$  to hidden node  $h_j$  and weight  $\nu_{jk}$  connects  $h_j$  to output node  $o_k$ .

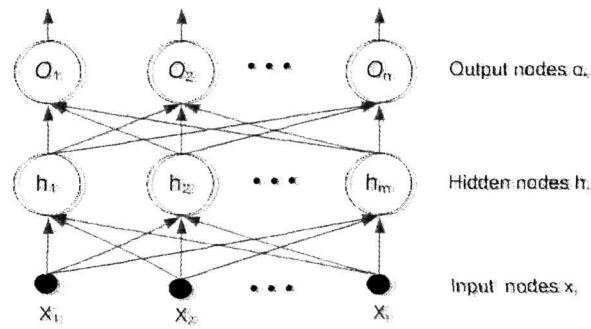


Figure 6.1. Two layers perceptron

Classification begins by presenting a pattern to the input nodes  $x_i$ ,  $1 \leq i \leq l$ . The data flow in one direction through the perceptron until the output nodes  $o_k$ ,  $1 \leq k \leq n$ , are reached. Output nodes will have a value of either -1 or 1. Thus, the perceptron is capable of partitioning its pattern space into  $2^n$  classes. The steps that govern the data flow through the perceptron during classification are (Ritter and Wilson, 1996):

1. Present the pattern  $p = [p_1, p_2 \dots p_l] \in R^l$  to the perceptron, that is, set  $x_i = p_i$  for  $x_i$ ,  $1 \leq i \leq l$ .
2. Compute the values of the hidden-layer nodes as it is illustrated in Figure 6.2,

$$h_j = \tanh(W_{oj} + \sum_{i=1}^l W_{ij}x_i) \quad 1 \leq j \leq m \quad (6.1)$$

3. Calculate the values of the output nodes according to

$$o_k = \text{threshold}(\nu_{ok} + \sum_{j=1}^m \nu_{jk}h_j) \quad 1 \leq k \leq n \quad (6.2)$$

4. The class  $c = [c_1, c_2 \dots c_n]$  that the perceptron assigns to the pattern  $p$  must be a binary vector. So  $o_k$  must be the threshold at some level  $\tau$  and depends on the application.
5. Repeat steps 1, 2, 3 and 4 for each pattern that is to be classified.

Multilayer perceptrons are highly nonlinear interconnected structures and are, therefore, ideal candidates for both nonlinear function approximation and nonlinear classification task. It has been applied to a variety of problems in image processing, including optical character recognition (Sackinger et al., 1992) and medical diagnosis ((Dhawan et al., 1996)and (Dhawan and Leroyer, 1988)).

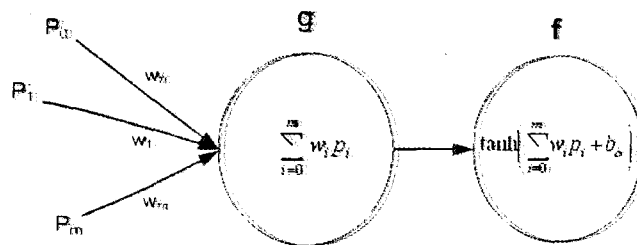


Figure 6.2. Propagation rule and activation function for the MLP network

## 6.4 Supervised Classification Results using Neural Network

A commercial Neurosolution V3.0 (Neurosolution, V 3.0), equipped with a computational component that can be used as pattern classifier using extracted features, was used. ANNs of the feedforward type, or MLPs, have been applied because they have been found to be excellent functional mappers for problems that can be formulated as requiring an input-output map. A MLP, with one hidden layer, was employed. The detailed of the architecture may be represented by Figure 6.1. In our case, the convexity measures based on area and perimeter were used as the two inputs. The hidden layer contains 4 processing elements and they return  $h_j = \tanh(W_{j0} + \sum_{i=1}^2 C_{ij} W_{ji})$ . Where  $W_{ji}$  and  $W_{j0}$  are weights and biases of the hidden layer which were modified automatically during training. Finally the output of processing element returns

either 1 or -1 determined by  $o_k = \text{threshold}(\nu_{ko} + \sum_{j=1}^4 \nu_{kj}h_{jk})$ , where  $\nu_{kj}$  and  $\nu_{ko}$  are the weight and bias of the output processing element respectively. The following values for the weights and the biases were found after training using 3378 (441 overlapping and 2937 non-overlapping) crystals representing 60% of the data set:

$$W_{ji} = \begin{pmatrix} -1.4412 & -0.6594 \\ -0.8301 & -4.7285 \\ -2.0455 & -0.5245 \\ 0.9384 & 1.2539 \end{pmatrix}, \quad W_{jo} = \begin{pmatrix} 0.3472 \\ 4.3145 \\ 1.2725 \\ 0.9737 \end{pmatrix}$$

$$\nu_{kj} = (0.7660 \quad -1.8131 \quad -1.0736 \quad 0.6137), \quad \nu_{ko} = (0.1942)$$

The two inputs are:

$$C = \begin{pmatrix} C_A \\ C_P \end{pmatrix}$$

Thus,

$$\begin{pmatrix} h_1 \\ h_2 \\ h_1 \\ h_2 \end{pmatrix} = \tanh \begin{pmatrix} -1.4412 \times C_A - 0.6594 \times C_P + 0.3472 \\ -0.8301 \times C_A - 4.7285 \times C_P + 4.3145 \\ -2.0455 \times C_A - 0.5245 \times C_P + 1.2725 \\ 0.9384 \times C_A + 1.2539 \times C_P + 0.9737 \end{pmatrix}$$

The ANN output is calculated in a number of steps. First, the output from the previous (hidden) layer is multiplied by the matrix  $\nu_{kj}$  and  $\nu_{ko}$  is added. This is then thresholded  $o_k = \text{threshold}(\nu_{ko} + \sum_{j=1}^4 \nu_{kj}h_{jk})$ , which will have values of -1 or 1. The confusion matrix for the test dataset is shown in Table 6.1. The percentages are shown in brackets

Table 6.1. Confusion matrix calculated using ANN

Predicted	Actual	
	Non overlapping	Overlapping
Non overlapping	1830(94.28%)	14(4.5%)
Overlapping	111(5.72%)	297(95.5%)
Total	1941(100%)	311 (100%)

It is seen that most (94.28%) of the non-overlapping and (95.5%) overlapping crystals were correctly classified.

## 6.5 Support Vector Machine

Support vector machines (SVM) have originated from statistical learning theory in the middle of the 1990's (Mangasarian, 2000). The construction of SVMs has been described in Cristianini and Shawe-Taylor (2000). In this section, a brief introduction on how to construct an SVM is presented. Consider a binary classification problem, where the given data set is partitioned into two classes with a linear hyperplane separating them. Assume that the training dataset consists of  $k$  training samples represented by  $(x_1, y_1), \dots, (x_k, y_k)$ , where  $x_i \in R^N$  is an  $N$ -dimensional data vector with each sample belonging to either of the two classes labeled as  $y_i \in -1, +1$ . The goal of SVMs is to find a linear decision function defined by  $f(x) = w \cdot x + b$ , where  $w \in R^N$  determines the orientation of a discriminating hyperplane, and  $b \in R$  is a bias. The hyperplanes for the two classes are, therefore, represented by  $y_i(w \cdot x + b) \geq 1$ . Due to noise or mixture of classes during the selection of training data, variables  $\xi_i > 0$ , called slack variables, are introduced to cater for the effects of misclassification. The hyperplanes for the two classes become  $y_i(w \cdot x + b) \geq 1 - \xi_i$ . The optimal hyperplane (i.e.,  $f(x) = 0$ ) is located where the margin between two classes of interest is maximized and the error is minimized. It can be obtained by solving the following constrained optimization problem (Cristianini and Shawe-Taylor, 2000),

$$\begin{aligned} \text{Minimize: } & \frac{1}{2} \|W\|^2 + \nu \sum_{i=1}^k \xi_i \\ \text{Subject to: } & y_i(W \cdot x + b) \geq 1 - \xi_i \text{ for } i = 1, 2, \dots, k \end{aligned} \quad (6.3)$$

The constant  $\nu > 0$  is called the penalty value or a regularization parameter. It defines the trade-off between the number of misclassifications in the training data and the maximization of the margin. In practice,  $\nu$  is selected by trial and error. The constrained optimization problem, in the equation above, is solved by the method of Lagrange multipliers. The equivalent (or the dual) optimization problem becomes,

$$\begin{aligned}
& \text{Maximize: } \sum_{i=1}^k \alpha_i - \frac{1}{2} \sum_{i=1}^k \sum_{j=1}^k \alpha_i \alpha_j y_i y_j (x_i \cdot x_j) \\
& \text{Subject to: } \sum_{i=1}^k \alpha_i y_i = 0 \text{ and } 0 \leq \alpha_i \leq \nu, \text{ for } i = 1, 2, \dots, k
\end{aligned} \tag{6.4}$$

where  $\alpha_i > 0$  are the Lagrange multipliers. The solution of the optimization problem in the equation above is obtained in terms of the Lagrange multipliers,  $\alpha_i$ . According to the Karush-Kuhn-Tucker optimality condition, some of the multipliers will be zero. The multipliers that have nonzero values are called the support vectors. The results from an optimizer, called an optimal solution, are a set  $\alpha = (\alpha_1, \dots, \alpha_k)$ . The value of  $W$  and  $b$  are calculated from  $w = \sum_{i=1}^k y_i \alpha_i x_i$  and  $b = \frac{1}{2}[W \cdot x_{+1} + W \cdot x_{-1}]$ , where  $x_{+1}$  and  $x_{-1}$  are the support vectors of class labels +1 and -1 respectively. The decision rule is then applied to classify the dataset into two classes i.e +1 and -1.

$$f(x) = \text{sign}(w \cdot x + b) \tag{6.5}$$

## 6.6 Supervised Classification Results using Support Vector Machines

SVMs classify points by assigning them to one of two disjoint half spaces. The Lagrangian Support Vector Machines (LSVM) used in this classification work have been described by Mangasarian and Musicant (2000). The following values for the weight and bias were found after training:

$$W = (4.370 \quad 10.851) \text{ and } b = (13.331)$$

The equation of the discriminating line ( $f(x) = \text{sign}(w \cdot x + b)$ ) for the SVM in terms of the features,  $C_A$  and  $C_P$ , may be written as:

$$4.370 \times C_A + 10.851 \times C_P + 13.331 = 0 \tag{6.6}$$

Table 6.2 shows the confusion matrix of the classification result using SVMs. For the purpose of comparison, the same data set used for ANN was also used for the SVM analysis.

Table 6.2. Confusion matrix calculated using SVM

Predicted	Actual	
	Non overlapping	Overlapping
Non overlapping	1917(98.76%)	46(14.79%)
Overlapping	24 (1.24%)	265 (85.21%)
Total	1941 (100%)	311 (100%)

It is seen that most (98.76%) of the non-overlapping and (85.21%) overlapping crystals were correctly identified.

## 6.7 Conclusions

ANN and SVM were used to classify crystals as overlapping and non overlapping using crystals convexity measures. The confusion matrix calculated for MLP showed that many overlapping crystals (4.5% of overlapping crystals) were misclassified as non-overlapping crystals while relatively higher (5.72% non-overlapping crystals) were misclassified as overlapping crystals. The classification results using SVM show that 46 out of 311 (14.8%) were misclassified overlapping crystals. Relatively few 1.2% non-overlapping crystals were misclassified as overlapping crystals. The percentage of misclassified overlapping crystals by SVM was higher than the percentage of misclassified overlapping crystals by MLP. In both cases, fairly acceptable percentage of misclassification of non-overlapping crystals as overlapping was obtained. The confusion matrix showed that SVM gave relatively lower percentage of misclassified non overlapping crystals.



# Chapter 7

## Comparison of Crystal Sizing Algorithms and Sieving Technique

### 7.1 Introduction

Traditionally, crystal size measurements are carried out by inspection or by using mechanical sieves. Apart from being time consuming, these techniques can only provide limited quantitative information. To address these problems, a digital image processing (DIP) technique, which involves automatically analyzing a captured image of a representative sample of  $\approx 100$  crystals has been developed. Two crystal sizing algorithms, that were described in Chapter 4 and Chapter 5, have been compared with the sieving method. The first applies ultimate erosion followed by a distance transformation (UE+DT), which performed better than the other algorithms discussed in Chapter 4, and the second uses convexity measures to remove overlapping crystals. Using two samples obtained from a sugar refinery, the parameters of interest, including mean aperture (MA) and coefficient of variance (CV), were calculated and compared with those obtained from the sieving method. The imaging technique is faster, more reliable than sieving and can be used to measure the full crystal size distributions of both massequite and dry product.

## 7.2 Crystal Size Distribution Analysis using Mechanical Sieve

Generally, mechanical sieving is the most commonly used method to determine sugar crystal size parameters in a production environment. Basically, the sieving operation attempts to divide a fixed mass of sugar into fractions, each of which has crystals that lie within specified size limits. This size separation is accomplished using a number of sieves that are pan shaped and have stainless steel mesh bottoms with decreasing aperture sizes. As detailed in Chapter 2, before the sieving starts, the sieves are first stacked with the smallest mesh size at the bottom and the largest one at the top. A pan is placed underneath to collect the sugar crystals which pass through all sieves.



Figure 7.1. Example of sieves used for crystal sizing. They are four sieves and a pan at the bottom.

Figure 7.1 shows an example of such a set of sieves used for crystal size measurement in the sugar industry. To perform sieving, the sugar sample is placed in the top sieve which has the largest mesh size, covered, and then shaken for 15 minutes in a mechanical shaker. During shaking, the crystals pass through sieves of successively smaller size until they are retained on a sieve that is too small for them to pass through. After sieving, the quantity of each fraction of crystals remaining in the

individual sieve pans is measured by weighing. The size of the crystals that pass through a particular mesh is not always smaller than the size of the sieve. Due to the elongated shape of the crystals, it is possible that crystals, which are much longer than the aperture size, can pass through the mesh as shown in Figure 7.2. The crystals passing through a sieve can actually have one dimension larger than the size of the sieve aperture. In this case the sieve size is a measure of the smaller dimensions of the crystals.

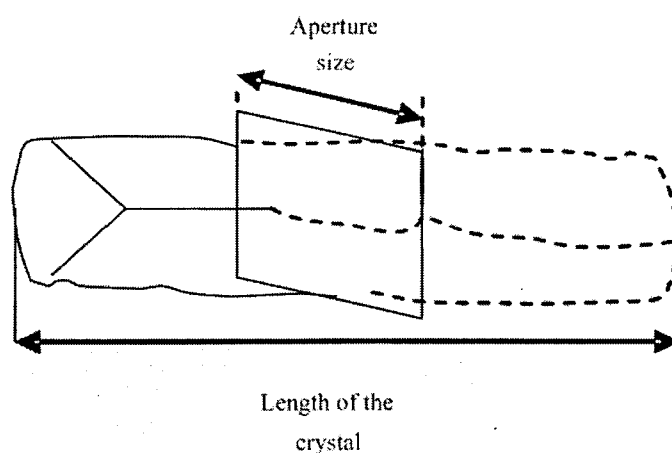


Figure 7.2. Example of elongated crystal passing a square sieve whose size is smaller than the length of the crystal. In this case crystal size is the measure of the other sides of the crystals.

The other possibility is that, some crystals can be oriented diagonally when they pass through the sieve aperture as shown in Figure 7.3. In this case the length of a particle passing through a sieve can be greater than the sieve size, although it has to be smaller than the diagonal length of the sieve aperture.

The result of the sieve analysis can be used to estimate the crystal size parameters (MA and CV) using either a look-up-table based on the mass fraction retained or using empirical equations (such as the Rens method) based on the cumulative percentage by mass.

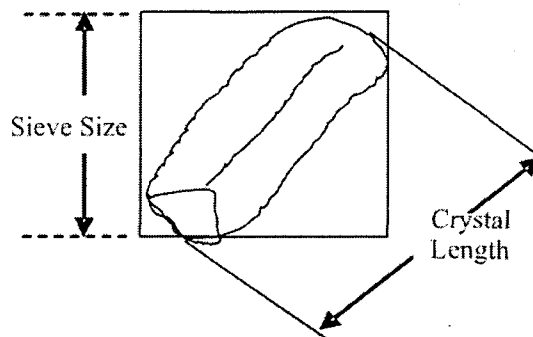


Figure 7.3. Example to show a crystal whose length is bigger than a sieve size can pass through the square sieve aperture.

### 7.3 Using Digital Image Processing

The image analysis technique for crystal sizing requires a high quality crystal picture which is well focused, uniformly illuminated and has large number of pixels. The imaging system used to take the pictures of the sugar samples consisted of a CCD camera attached to a microscope. The microscope had a magnification of  $8\times$  and the field of view was measured using a calibrating micrometer stage. Having acquired images of the samples, two independent automatic segmenting algorithms (i.e. UE+DT (Argaw et al., 2006) and the algorithm based on convexity measures) were applied. From the extracted crystals, the following morphological parameters were measured: area, perimeter, length, width and convexity. The area was defined as the projected area of the crystal in its stable position. This involves counting the number of the pixels inside the closed boundary of the crystal image and converting the pixel count to an area using the scale factor determined by the size calibration. The length and width were determined from the dimensions of the smallest bounding box as shown in Figure 7.3. The results were then saved as a text file for statistical analysis.

### 7.4 DIP and Mechanical Sieving Methods

Two different sugar samples (Sample #1 and #2) were obtained from the Hulleys Refinery in Durban, South Africa. These were analyzed using the sieving technique at SMRI and Hulleys and compared with the analysis using DIP methods. Since the

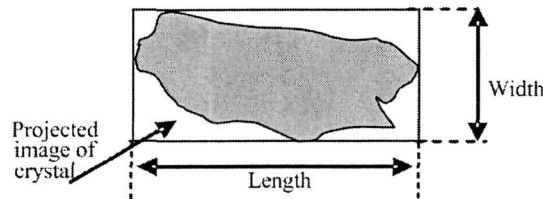


Figure 7.4. One possible operational definition of the length and width of a crystal can be based on the dimensions of a bounding box.

results from these two techniques will be compared, it is constructive to consider the differences between these two techniques.

1. In mechanical sieving, the sugar retained on each sieve and the pan is measured by weighing the mass and these are then used to plot the cumulative percentage by mass curve. In DIP, however, the volume or mass of the sugar is not measured. Because the acquired image is only a two dimensional projection of the crystal, the depth of the crystal is not measured. Thus, using DIP, only the area of each of the crystals is directly obtained and this is presented in terms of the cumulative percentage by mass.
2. In mechanical sieving, due to the relatively small number of sieve sizes used, the size distribution of the crystal sample is determined by a fairly small number of data points. Thus, subtleties of the shape of the distribution function are not well described. However, since the size of the individual crystals are measured directly using DIP, the crystal sizes can be sorted into any number of bins (provided that enough crystals are measured) and hence the cumulative distribution function can in principle be described by a much larger number of data points.

The DIP results can be compared to the sieving results by converting the area, obtained from DIP, to mass using a couple of techniques. Dalziel et al. (1999) calculated volume from the area as  $A^{\frac{3}{2}}$ . An alternative technique used by Mora et al. (1998) for cement particles makes the assumption that the particles are taken from the same sample and hence have more or less the same shape characteristics. The crystal depth is then assumed to be related its width by:

$$\text{depth} = \beta \times \text{width} \quad (7.1)$$

for some constant,  $\beta$ . The Volume of the crystal may then be calculated as:

$$\begin{aligned}\text{Volume} &= \text{area} \times \text{depth} \\ &= \beta \times \text{area} \times \text{width}\end{aligned}\tag{7.2}$$

This relationship between volume and area was also used to characterise the size and shape of coarse aggregate for concrete (Kwan et al., 1999) and (Mora and Kwan, 2000). The cumulative percentage by mass then turns out to be independent of  $\beta$  and the crystal density  $\rho$  and may be incrementally calculated for each of the bins as:

$$\frac{\rho \times \beta \times \sum_{i=1}^p \text{area} \times \text{breadth}}{\rho \times \beta \times \sum_{i=1}^n \text{area} \times \text{breadth}} = \frac{\sum_{i=1}^p \text{area} \times \text{breadth}}{\sum_{i=1}^n \text{area} \times \text{breadth}}\tag{7.3}$$

where the summation in the denominator is for all crystals while the summation in the numerator is for the crystals whose size is smaller than that particular value. Having the area converted to mass, the results obtained by DIP can then be compared to those obtained using sieving. The results from two automatic image based algorithms were compared with the result from mechanical sieving analysis.

#### 7.4.1 Comparing with UE+DT Algorithm

The cumulative percentage by mass curves for sieving and UE+DT were compared with a direct determination of individual crystal size by clicking on the crystal boundaries as shown in Figure 7.5. Although there is a fair discrepancy between these curves, it is instructive to calculate the corresponding values of MA and CV using the Rens method and compare them with those obtained by directly clicking on the crystals. These results are shown in Table 7.1. Since there does not appear to be any reason why the clicking technique does not accurately describe the sugar crystal size distribution, we must treat this curve as ground truth. Comparing sieving with clicking method, large percentage differences in MA and CV were obtained. The percentage difference calculated for CV, using UE+DT, was reasonably low although MA was calculated with bigger percentage. It is clear that the three cumulative

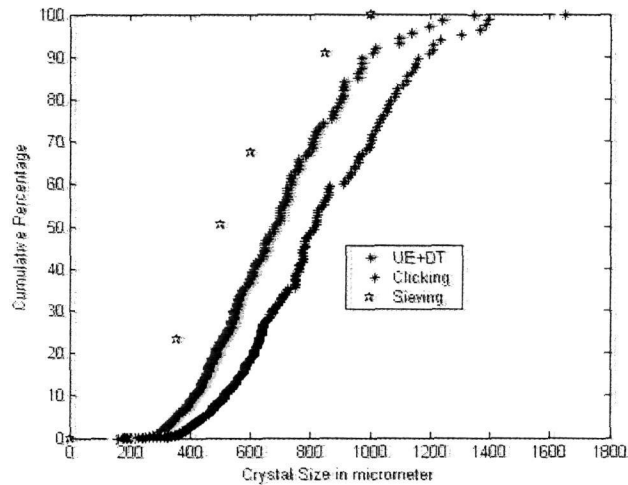


Figure 7.5. cumulative percentage by mass curves for SMRI sieving results (black), UE+DT (blue) and clicking (red).

percentage by mass curves shown in Figure 7.5 do not agree with each other. Firstly, as illustrated in Figure 7.2 and 7.3, it is possible for the sieving method to give a distribution, which has smaller crystal sizes than the directly measured clicking method. This is consistent with the effect that, on average, it is possible for crystals which have dimensions larger than the mesh aperture size to pass through the sieve. Secondly, the cumulative percentage by mass curve in Figure 7.5 found using UE+DT also indicates a size distribution that is smaller than that obtained by the clicking method. Careful examination of the segmentation results achieved by UE+DT indicated that some of overlapping crystals were being over segmented by the algorithm. This resulted from marking the crystal with multiples marker. In order to eliminate this effect, another algorithm based on the convexity of each crystal was used to first identify and reject overlapping crystals. This algorithm used convexity measures of the crystal based on perimeter and area to identify and remove overlapping crystals. The resulting cumulative frequency curves then coincided very closely with the clicking curves as discussed in Section 7.4.2.

The implications of this discrepancy between the sieving and clicking results are not yet fully understood. Since sieving is routinely and consistently used in the sugar industry, it is possible that the sieving results can nevertheless be useful in

Table 7.1. Summary of MA and CV and their % error calculated using sieving and UE+DT for two samples labeled n = 1, 2. The % errors for MA and CV are calculated with respect to the values obtained by the direct clicking method.

Methods	n	MA( $\mu m$ )	Error (%)	CV (%)	Error (%)
SMRI Sieve	1	504	38	41	20
	2	505	42	45	36
Hullets Sieve	1	553	32	50	47
	2	602	31	35	2.9
UE+DT	1	678	16	34	0
	2	726	16	35	6
Clicking	1	815	-	34	-
	2	871	-	33	-

optimizing growth in the crystallisation pans and in maintaining a uniform exit product. It would certainly be an advantage to use the automatic UE+DT algorithm in the production environment. Since the sieving method is well established and is widely used in the sugar industry, we could choose to multiply the crystal masses by a shift factor, S, that will shift the UE+DT cumulative percentage by mass curve to coincide with the sieve. The value of the shifting factor was calculated by searching for a value of S that gave best correlation between the cumulative percentage by mass curves calculated by sieving and UE+DT algorithm. Figure 7.6 shows plot of correlation coefficient calculated after shifting the UE+DT curve by different shifting factors ranging from  $S = 0.4$  to 1 for a sample image. Since the shift factor, S, determined in this way for the two samples were so close to each other (0.60 and 0.625), an average value of  $S = 0.61$  was chosen and this then gave a good agreement between the sieving and UE+DT curves as shown in Figure 7.7. A summary of the MA and CV values calculated, after shifting the cumulative percentage by mass curve by a shift factor of  $S = 0.61$ , is shown in Table 7.3.



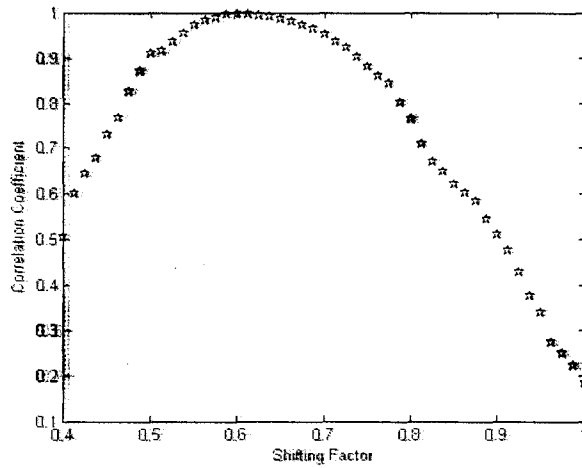


Figure 7.6. An example of graph for correlation coefficient between SMRI sieving and UE+DT cumulative curves, calculated by shifting a UE+DT curve, versus the shifting factor.

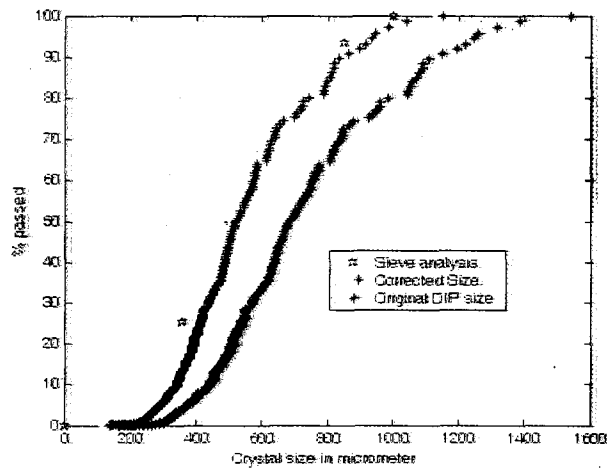


Figure 7.7. cumulative percentage by mass curves obtained by using UE+DT (before and after shifting using  $S = 0.61$ ) and sieving. Good agreement between the sieving and shifted UE+DT is observed.

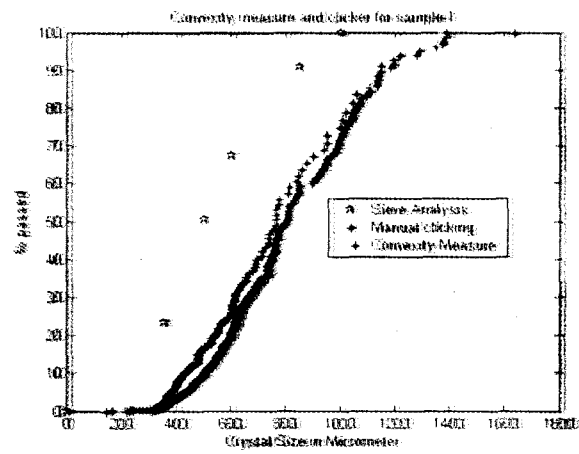
## 7.4.2 Comparing with Convexity Based Algorithm

The same technique could then also be applied to the convexity algorithm that works by excluding the overlapping crystals based on their convexity values. Figure 7.8 shows the cumulative percentage by mass curves calculated using convexity measure, sieve analysis and manual clicking for the two samples. Comparing the convexity based algorithm curve with manual method, they are close to each other indicating that the convexity algorithm can calculate crystal size better than UE+DT. These curves, however, are consistently smaller than the curve generated using the sieve analysis. MA and CV calculated using Rens method is shown in Table 7.2.

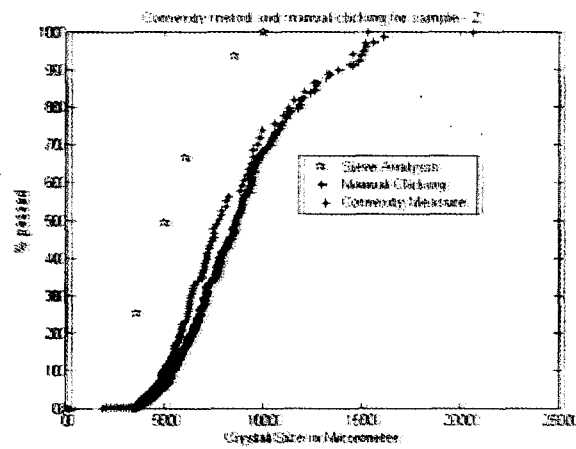
Table 7.2. Summary of MA and CV and their % error calculated using sieving and convexity method for two samples labeled n = 1, 2. The % errors for MA and CV are calculated with respect to the values obtained by direct clicking method.

Methods	n	MA( $\mu m$ )	Error (%)	CV (%)	Error (%)
Convexity	1	760	7	37	9
	2	793	9	37	12
Clicking	1	815	-	34	-
	2	871	-	33	-

After shifting the curves, although in this case a value of  $S = 0.55$  was required, the values of MA and CV could then be calculated by applying the Rens method. Figure 7.9 shows the curves obtained using convexity measure and sieving before and after size correction for two sugar samples. As expected the S factor was smaller than the factor used to correct the curves generated by UE+DT. Comparing with convexity method, UE+DT underestimates the crystal size. The effect of over segmentation of some overlapping crystals by UE+DT may account for this. Finally crystal size parameters were calculated using both algorithms after the shifting and compared with the same parameters calculated using sieving. Table 7.3 indicates the values of MA and CV and their percentage error, as compared with SMRI sieving results, found after shifting the cumulative percentage by mass curves with their respective shifting factors.

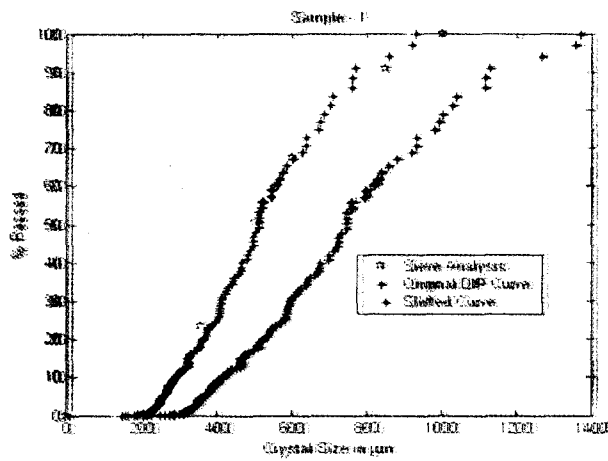


a.

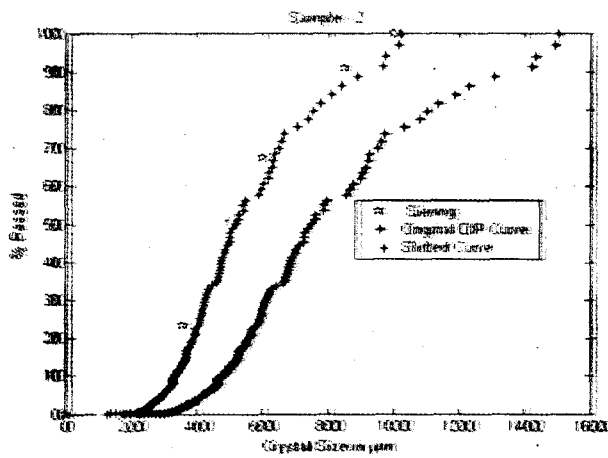


b.

Figure 7.8. The graph of cumulative percentage by mass versus crystal size calculated using convexity measure, sieve analysis and manual clicking for two samples (a and b). The red star is for convexity method, blue for the clicking and black star for the sieve. Only few data points can be obtained for the sieving method, which is one of its limitations.



a



b

Figure 7.9. The graph of cumulative percentage by mass versus crystal size calculated using convexity measure, sieve analysis (a and b). The red star is for shifted convexity method, blue for the original convexity and black star for the sieve.

Table 7.3. Summary of MA and CV calculated using sieving and automatic algorithms for two samples. A shifting factor  $S = 0.61$  was used for UE+DT while  $S = 0.55$  was used for convexity algorithm.

Methods	n	MA( $\mu m$ )	Error(%)	CV (%)	Error(%)
SMRI Sieve	1	504	-	41	-
	2	505	-	45	-
Hullets Sieve	1	553	9.7	50	21.9
	2	602	19.2	35	22.2
UE+DT	1	515	2.2	35	14.6
	2	516	2.2	37	17.7
Convexity	1	524	3.9	34	17.0
	2	513	1.6	36	20

Comparing with sieving method, both automatic algorithms calculated MA with an accuracy of 1-4 %. There was a bigger percentage error in CV.

## 7.5 Discussion

The possibility to measure sugar crystal size parameters (MA and CV) using digital image processing was introduced. Two crystal sizing algorithms (UE+DT and Convexity based algorithm) were developed and compared with sieving technique that is being currently used in sugar industry. They were also compared with clicking method which could be used as a benchmark. In sieving technique MA and CV were computed using the cumulative percentage of the mass of the crystals retained on the respective sieve size. Due to the fact that the volume of the crystals could not be determined from the projected crystals image, the area of the crystals was converted into a volume (mass) to compute cumulative percentage by mass. This conversion of area to mass helped to compare the image based methods with the sieve analysis.

The curves generated in this way were not exactly match to each other (Figure 7.5 and Figure 7.8) and caused the resulting MA and CV to be large on average by 28% and 26% respectively for UE+DT and 35% and 16% respectively for the convexity algorithm. There could be many reasons for this to happen. As illustrated in Figure 7.2 and 7.3 the size of the crystals that passed through a sieve could be bigger than the size of a sieve appertue. The cumulative percentage by mass curve

found using the clicking method was also shown bigger shift from UE+DT (Figure 7.5) although it was so close to the curve generated using convexity based algorithm (Figure 7.8). The effect of oversegmentation of some overlapping crystals by UE+DT could be a reason for such big shift. Better matching curves were generated using convexity algorithm.

Once the cumulative percentage by mass curves generated, the size parameters could be calculated. If the problem of such differences in cumulative percentage by mass curves generated using sieve analysis and imaging methods were not corrected, MA and CV calculated using sieve analysis and imaging methods would have big percentage error. So there was a need to shift the curves using the shifting factor(S). Shifting factor (S) was calculated for fine sugar samples whose value lied between 0.60 to 0.625 for UE+DT and 0.54 to 0.56 for the convexity algorithm. Shifting the curves by S has shown good agreement with the curves generated using sieving (Figure 7.7 and 7.9). Estimation of size parameters, after shifting the cumulative percentage by mass curves, can result in the value which is reasonably comparable with the same parameters measured using sieving techniques.

In fact MA and CV measured for the samples, using sieving technique, at Hullet and SMRI have shown big differences, as shown in Table 7.1 and 7.2. The question is which can be taken as the standard? For imaging techniques clicking could be used as the benchmark as it manually measure the size parameters from crystal images. Comparing with clicking, the percentage differences in MA and CV, calculated using the automatic algorithms are smaller than sieving techniques as shown in Table 7.1 and 7.2. These figures are higher for CV than MA. In the case of sieving few number of data points (less than or equal to 4) are used to calculate MA and CV using Rens method. In some samples the number of data points can be reduced to 2 if some of the data points fall outside the upper and the lower limits set in Rens method i.e. 90% and 10%. This in turn affects the values of MA and CV. This is one of the limitations of sieving method. The automatic algorithms, however, generate continuous curve which is not susceptible to such conditions of Rens method.

The other advantage of DIP methods is that because it can calculate the length

of the crystals, the elongation of the sugar sample can also be determined (as the mean ratio of length to width). Unlike sieving method, DIP can give detailed size information as it can directly measure the size of the individual crystals. Nevertheless DIP has disadvantage in limiting the number of overlapping crystals. It is even more difficult when one tries to measure very fine sugar crystal.

## 7.6 Conclusions

Two automatic digital image processing algorithms (UE+DT and the convexity algorithm) have been developed to obtain the crystal size parameters MA and CV from captured images of crystal samples. These results have been compared with those obtained by sieving which is the standard technique used in the sugar industry and by a direct determination that involved manually tracing the crystal borders. Interestingly, the MA and CV obtained from sieving are found to be smaller than the direct method. To some extent, this has been explained by noting that large crystals that have a dimension that is larger than the sieve aperture can pass through a smaller sieve. The oversegmenting problem associated with the UE+DT technique has been resolved by instead using an algorithm based on convexity. Finally, it has been demonstrated that if the DIP cumulative percentage by mass curves are multiplied by an average shift factor ( $S = 0.61$  for UE+DT and  $S = 0.55$  for Convexity method), MA values very close to those calculated by the sieve technique can be obtained.

098159

# Chapter 8

## Summary and Conclusions

### 8.1 Summary

In the sugar industry process control is used to insure that the final exit product which meets the required quality control standards. The various processes are usually monitored using a variety of indirect measurement techniques (as described in Chapter 2) such as conductivity, boiling point elevation, stirrer torque and radio frequency measurements in addition to visual inspection. The results from such indirect measurements are judged and the necessary decisions are made by the operators, who they make adjustment to the pressure, temperature, pH etc. This optimization is often compromised by operator fatigue and error. An automated system would not be subjected to these problems and would also allow for online feedback control.

In this study a computerized method has been developed to measure sugar crystal size parameters (MA and CV) directly from images of the dry sugar exit product. A number of algorithms have been evaluated to improve the accuracy of the results. Overlapping and touching crystals were found to compromise the accuracy of the techniques. The first approach attempted to develop an algorithm which could segment and separate overlapping and touching crystals. As described in Chapter 4, five algorithms, using marker controlled watershed segmentation, were investigated. These algorithms were compared with each other and with a manual method which involved clicking the boundaries of individual crystals using the computer mouse. This manual clicking method was used as a benchmark to evaluate the accuracy of the algorithms. Although a number of segmenting algorithms were examined, it was



found that a combination of ultimate erosion and the distance transform (UE+DT) was the most accurate in finding the correct crystal boundaries (as described in Chapter 4). Using dry crystal samples obtained from the Hullels Refinery South Africa, Durban, the MA and CV were calculated for each of 25 sample images using the Rens method after applying the UE+DT algorithm. MA and CV were calculated for the whole 25 crystal images used in this study with a mean percentage error 6% and 12% respectively.

The second approach, involved using a measure of convexity to identify and remove touching and overlapping crystals. As described in Chapter 5, two convexity measures based on the area and perimeter of the object were used. The algorithm first segmented the crystals from the background and then classified the object into two classes. The class with no overlapping or few overlapping crystals was then further processed to calculate the mean aperture (MA) and coefficient of variance (CV) using the Rens method. MA and CV were compared with the manual clicking which was assumed to be ground truth. This comparison gave relative errors of 7.75% and 9.73% for MA and CV respectively. Compared with UE+DT, the convexity technique gave MA with the higher percentage errors, but CV was predicted with lower percentage errors.

As described in Chapter 6, two different classification algorithms, SVM and ANN, were used to classify crystals as non-overlapping and overlapping. The convexity of the crystals based on their area and perimeter were used as input features. The classification accuracy of 94.3% and 98.8%, for non overlapping crystals, were achieved by ANN and SVM respectively.

In Chapter 7, the two best performing algorithms (UE+DT and convexity based algorithm) were compared with the commonly used mechanical sieving method. Using samples obtained from Hullels Refinery, the parameters of interest, including mean aperture (MA) and coefficient of variance (CV), were calculated and compared with those obtained using the sieving method. The results demonstrated that imaging technique was faster, more reliable than sieving and could be used to measure the full crystal size distributions.

## 8.2 Limitations and Recommendations

One of the problems in this study was crystals image which contains many overlapping and touching crystals and few number of separated (individual) crystals. The use of convexity to remove overlapping crystals resulted in a small number of individual crystals remaining in the image for analysis. Thus it would be necessary to increase the number of analysed images to ensure that a representative population was obtained. This problem could also be addressed by limiting the number of overlapping crystals in the images using a vibration or other technique to spread out the crystals.

In the algorithms that employed marker controlled watershed segmentation, a fixed size and shape of structural element was used. Due to the fact that the sugar crystal can have different size and shape, using a fixed big size structural elements erodes all the small crystals. It is possible that the remaining crystals in the image might not then constitute a representative sample. This in turn will affect the accuracy of the measurement of the crystal size parameters. This problem could be alleviated using an adaptive structural element which would modify its size and shape according to the size and shape of the crystals in the sample.

## 8.3 Conclusions

Automatic, computerized methods have been developed to measure sugar crystal size parameters directly from images of dry crystals which give objective, quantitative and reproducible values. Overlapping and touching crystals were problematic and negatively affected the accuracy of the algorithms. These problems were addressed using two different approaches. The first approach used marker controlled watershed segmentation (as described in Chapter 4). Depending on the kind of markers used, five algorithms were evaluated. These algorithms were compared with each other and with the manual clicking method (used as ground truth) that directly traced the boundary of the individual crystals using the computer mouse. The accuracy of the segmentation algorithms depended on the technique used to mark the crystal in the image. The parameters of interest included the mean aperture (MA) and coefficient of variance (CV). Comparing MA and CV calculated using the automatic

algorithms with same parameters calculated using manual clicking (used as ground truth), UE+DT (one of the automatic algorithm) exhibited the lowest percentage error (6% and 12% respectively).

The mean aperture (MA) and coefficient of variance (CV) were also calculated using the automatic algorithm based on convexity and compared with same parameters calculated by manual clicking (used as ground truth) and both agreed with mean percentage errors less than 10%.

The two algorithms (UE+DT and convexity based) were compared with the sieving method which is the standard technique used in the sugar industry. Using two sugar samples obtained from the Hullet Refinery, South Africa, the size parameters (MA and CV) were calculated from a captured crystal images. Interestingly, the MA and CV obtained from sieving are found to be smaller than the direct method. To some extent, this has been explained by noting that large crystals that have a dimension that is larger than the sieve aperture can pass through a smaller sieve. Finally, it had been demonstrated (in Chapter 5) that if the DIP cumulative percentage by mass curves were multiplied by a common shift factor, values very similar to those calculated by the sieve technique can be obtained.

Generally, the study demonstrated the feasibility of an alternative method for crystals size measurement directly from crystal images captured using digital camera. Although dry sugar samples were used in the study; in principle the algorithms can also be used to calculate the size of crystals in the massecuite.

## 8.4 Future Work

In this study, automatic algorithms for sugar crystal size measurement direct from crystal images were evaluated. Images were captured by spreading the crystal sample on the microscope slide using transmitted illumination. The images could also be captured using reflected light. Spreading the sugar sample on the dark container could increase the contrast between the object and the background. This in turn would improve the accuracy of the segmentation algorithms.

Testing of these algorithms at the industry stage using sugar crystals image taken direct from the crystallization pan will be our future work.

## References

- Anon (2005), *Raw sugar grain size distribution*, Method 8.11 in: Laboratory Manual for South African Sugar Factories edn, South African Sugar Technologists Association, Mount Edgecombe, South Africa.
- Argaw, G. A., Alport, M. J. and Malinga, S. B. (2006), 'Automatic measurement of crystal size distribution using image processing.', *Proceedings South African Sugar Technologist Association*, **80**, 399–411.
- Bennet, J. (1936), 'Broken coal', *Journal of Inst. Fuel*, **10**, 22.
- Beucher, S. (1992), 'The watershed transformation applied to image segmentation.', *Scanning Microscopy Supplement*, **6**, 299–314.
- Beucher, S. and Lantuèjoul, C. (1979), 'Use of watersheds in contour detection.', *Proc. Int. Workshop on Image Processing, Real-Time Edge and Motion Detection/Estimation*, .
- Bradley, A. P. (1997), 'The use of the area under the ROC curve in the evaluation of machine learning algorithms.', *Pattern Recognition*, **30**(7), 1145–1159.
- Brown, D. J., Alexander, K. and Boysan, F. (1991), 'Crystal growth measurement and modeling of fluid flow in a crystallizer.', *CITS Proceedings*, **19**, 77–94.
- Bubnik, Z., Kadlec, P., Hinkova, A., Pour, V. and Starhova, H. (2003), 'Optimisation of cooling crystallisation by ultrasonic technique.', *CITS Proceedings*, **22**, 181–189.
- Butler, R. (1974), 'Butler method for assesement of MA and CV', *Proceedings 16th Session ICUMSA*, **16**.

- Chen, S. and Haralick, R. M. (1996), 'Recursive erosion, dilation, opening, and closing transforms.', *IEEE Trans. on Image Processing*, **4(3)**, 335–345.
- Cristianini, N. and Shawe-Taylor, J. (2000), *An introduction to support vector machines and other kernel-based learning methods.*, ISBN 0521780195, second edition edn, Press syndicate of the University of Cambridge.
- Dalziel, S. M., Tan, S. Y., White, E. T. and Broadfoot, R. (1999), 'An image analysis system for sugar crystal sizing.', *Proceedings of Australian Society of Sugar Cane Technologist*, **21**, 366–372.
- Derganc, J., Likar, B., Bernard, R., Tomazevic, D. and Pernus, F. (2003), 'Real time automated visual inspection of color tablets in pharmaceutical blisters.', *Real-time imaging*, **9**, 113–124.
- Destival, I. (1986), 'Mathematical morphology applied to remote sensing.', *Acta Astronautica*, **13**, 371–385.
- Dhawan, A., Chitre, Y., Kaiser, C. and Moskowitz, M. (1996), 'Analysis of mammographic microcalcifications using gray-level image structure features.', *IEEE Trans. Medical Imaging*, **15**, 246–259.
- Dhawan, A. P. and Leroyer, E. (1988), 'Mammographic feature enhancement by computerized image processing.', *Computer Methods and Programs in Biomedicine*, pp. 23–25.
- Doss, K. S. G. (1983), 'New control figure for monitoring crystallization of sugar conductometric purity.', *Proceedings Sugar Technologists India*, **47**, MG1–6.
- Fawcett, T. (2006), 'An introduction to ROC analysis.', *Pattern Recognition Letters*, **27(8)**, 861–874.
- Frank, Y. S. and Yi-Ta, W. (2004), 'Fast euclidean distance transformation in two scans using  $3 \times 3$  neighborhood.', *Computer vision, Graphics, and Image Understanding*, **93**, 195–205.
- Gordon, G. and Vincent, L. (1992), *Application of morphology to feature extraction for face recognition. In nonlinear Image Processing III*, Vol. SPIE - 1658.

- ICUMSA (1994), 'The determination of the particle size distribution of white sugar by sieving.', *ICUMSA Methods Book*, **GS2-37**.
- Ingram, G. D. and Steindl, R. J. (2001), 'Rapid crystal sizing on the pan stage by digital image analysis.', *Proceedings of Australian Society of Sugar Cane Technologist*, **22**, 361–368.
- Kwan, A. K. H., Mora, C. F. and Chan, H. C. (1999), 'Particle shape analysis of coarse aggregate using digital image processing.', *Cement and concrete research*, **29**, 1403–1410.
- Laitinen, T., Silven, O. and Pietikäinen, M. (1990), *Morphological image processing for automated metal strip inspection. Image algebra and morphological image processing.*, Vol. SPIE - 1350.
- Latecki, L. J. and Lakamper, R. (1999), 'Convexity rule for shape decomposition based on discrete contour evolution.', *Computer vision and image understanding*, **73**(3), 441–454.
- Liang, S., Ahmadi, M. and Shridhar, M. (1994), 'A morphological approach to text string extraction from regular periodic overlapping text/background images.', *Computer vision, Graphics, and Image Processing: Graphical Models and Image processing*, **65**(5), 402–413.
- Mangasarian, O. L. (2000), 'Generalized support vector machines.', *Advances in Large Margin Classifiers*, Cambridge, MA, MIT Press. pp. 135–146.
- Mangasarian, O. and Musicant, D. (2000), Lagrangian support vector machines, Technical Report Tech. Rep 0006, Data Mining Institute, Computer Science Department, University of Wisconsin, Madison, Wisconsin.
- MATLAB (6.5), '<http://www.mathwork.com>'. MATLAB Technical computing.
- Merle, J. P. (2004), 'Improvements in white sugar crystallization control at ch sugar co.', *Publication of technical papers and Proceedings of the sixty-third Annual meeting of sugar industry technologist (SIT)*, **63**, 15–19.

- Mhlongo, A. Z. and Alport, M. J. (2002), 'Application of artificial neural network techniques for measuring grain sizes during sugar crystallization.', *Proceeding South African Sugar Technologist Association*, **76**, 460–468.
- Miller, K. F. and Beath, A. C. (2000), 'The measurement of raw sugar crystal size by sieving and by laser diffraction.', *Proceedings of Australian Society of Sugar Cane Technologist*, **22**, 393–398.
- Mora, C. F. and Kwan, A. K. H. (2000), 'Sphericity, shape factor, and convexity measurement of coarse aggregate for concrete using digital image processing.', *Cement and concrete research*, **30**, 351–358.
- Mora, C. F., Kwan, A. K. H. and Chan, H. C. (1998), 'Particle size distribution analysis of coarse aggregate using digital image processing.', *Cement and concrete research*, **28**, 921–932.
- Neurosolution (V 3.0), '<http://www.neurosolutions.com/>'. Neurosolution Technical Computing.
- Norberto, M. C. O. D. S., Juan, J. V., Andre, S., Isabel, V., Jose, M. G. S. and Francisco, D. P. (1997), 'Applying watershed algorithms to the segmentation of clustered nuclei', *Cytometry*, **28**, 289–297.
- Otsu, N. (1979), 'A threshold selection method from grey level histograms.', *IEEE Transactions on systems, Man, and Cybernetics*, **SMC-9**(1), 62–66.
- Palenzuela, G. S. E. and Cruz, V. I. P. (1996), 'Techniques for classifying sugar crystallization images based on spectral analysis and the use of neural networks.', *Proceedings IWISPO '96 Third international workshop on Image and Signal Processing - Advances in Computational Intelligence*, **3**, 641 – 645.
- Peacock, S. D. (1998), 'An introduction to neural networks and their application in the sugar industry.', *Proceeding South African Sugar Technologist Association*, **72**, 184 –191.
- Peacock, S. D. (2000), Grain size analysis: A review of current methods, Technical report, Tongaat - Hulett Internal Memorandum.



- Pezzi, G. and Maurandi, V. (1993), 'Numerical methods for calculations of sugar grain size distribution.', *Zuckerind*, **118**, 113–123.
- Powers, H. (1948), 'Determination of the grist of sugars.', *International Sugar Journal*, **50**, 149–150.
- Prasad, M. and Singh, K. (1999), 'Electrical conductivity of sugar crystal as a measurement of its quality.', *Taiwan Sugar*, **V46**, 19–22.
- Rens, G. (1978), 'Rens Method', *Sucr. Belge*, **97**, 169–174.
- Ritter, G. and Wilson, J. (1996), *Handbook of Computer Vision Algorithms in Image Processing Algebra* second edition edn, Boca Raton: CRC Press.
- Rosin, P., Rammler, E. and Sperling, K. (1933), 'RRSB Methods', *Wärme*, **56**, 783.
- Sackinger, E., Boser, B., Bromley, J., Lecun, Y., and Jackel, L. (1992), 'Application of an anna neural network chip to high-speed character recognition.', *IEEE Trans. Neural Networks*, **3**, 498 – 505.
- Schoonees, B. M. (2002), Grain size sieve analysis calculations, Technical Report 13/03, SASTA.
- Schultz, A. C. and Edye, L. A. (2000), 'On - line measurement of crystal content in masseuites using low resolution nuclear magnetic resonance spectroscopy.', *Proceedings of Australian Society of Sugar Cane Technologist*, **22**, 380–384.
- Schumann, G. T. and Thakur, C. S. (1993), 'The use of video camera and PC for crystal image analysis.', *Proceedings of South African Sugar Technologist Association*, **67**, 135–139.
- Serra, J. (1982), *Image analysis and mathematical morphology*, London: Academic press.
- Sharma, K. K., Joshi, H. C., Singh, P. and Shukla, O. S. (2003), 'Fussy logic based control system enter sugar industry.', *Proceedings of the Sugar Technologist Association of India*, **65**, 84–94.

- Skolnick, M. (1986), 'Application of morphological transformations to the analysis of two-dimensional electrophoretic gels of biological materials', *Computer vision, Graphics, and Image Processing*, **35**, 306–332.
- Sonka, M., Halvac, V. and Boyle, R. (1998), *Image processing analysis and machine vision*, ISBN 0-534-95393-X, second edition edn, Brooks/Cole.
- Swets, J. A., Dawes, R. M. and J., M. (2000), 'Better decisions through science.', *Scientific American*, **283**, 82–87.
- Talbot, H. (1996), *A Morphological algorithm for linear segment detection. Mathematical morphology and its applications to image and signal processing.*, Boston Kluwer Academic Publishers.
- Talbot, H., Jeulin, D. and Hanton, D. (1996), 'Image analysis of insulation mineral fibers', *Microsc. Microanal. Microstruct.*, **7**, 361–368.
- Theisen, K. H. and Diringer, T. (2000), 'Microwave concentration measurement for process control in the sugar industry.', *Publication of technical papers and Proceedings Sugar Industry Technologist (SIT)*, **59**, 79–92.
- Thiran, J.-P. and Macq, B. (1996), 'Morphological features extraction for the classification of digital images of cancerous tissues.', *IEEE Trans. Biomedical Engineering*, **43(10)**, 1011–1020.
- Tzschatzsch, O., Schick, R. and Fleisher, L. G. (2003), 'Viscosity as a measurement and control parameter for sugar boiling.', *Proceedings International Commission for Sugar Technology (CITS)*, **22**, 159–172.
- Vincent, L. and Beucher, S. (1989), The morphological approach to segmentation: an introduction, Technical report, CMM, School of Mines, Paris.
- Vincent, L. and Soille, P. (1991), 'Watersheds in digital spaces: An efficient algorithm based on immersion simulation.', *IEEE Transactions on Pattern Analysis and Machine Intelligence*, **13(6)**, 583 – 597.
- Zhu, C. and Wang, R. (2004), 'A fast automatic extraction algorithm of elliptic objects groups from remote sensing images.', *Pattern recognition letters*, **25**, 1471–1478.

Zunic, J. and Rosin, P. L. (2004), 'A new convexity measure for polygons.', *IEEE transactions on pattern analysis and machine intelligence*, **26**(7), 923 – 934.